Aalto University
School of Engineering

Jussi Tamminen

Computational analysis of wireless inductive power transfer for charging light-duty electric vehicles

Thesis submitted as partial fulfilment of the requirements for degree of Master in Science (Technology)

Espoossa 31.1.2020
Supervisor: Professor Kari Tammi
Advisors: Pauli Salminen and Jenni Pippuri-Mäkeläinen

Aalto-yliopisto
Insinööritieteiden korkeakoulu

Aalto-yliopisto, PL 11000, 00076 AALTO
www.aalto.fi

Diplomityön tiivistelmä

Tekijä Jussi Tamminen

Työn nimi Induktiivisen langattoman tehonsiirron laskennallinen analyysi kevyiden sähköautojen lataamista varten

Maisteriohjelma Mechanical engineering **Koodi** ENG25

Työn valvoja Kari Tammi

Työn ohjaajat Pauli Salminen ja Jenni Pippuri-Mäkeläinen

Päivämäärä 30.1.2020 **Sivumäärä** 72 **Kieli** Englanti

Tiivistelmä

Langattomat latauslaitteet voivat osaltaan parantaa sähköautojen käyttömukavuutta, mikä lisäisi sähköautojen houkuttelevuutta kuluttajien silmissä, ja siten lisäisi sähköautojen lukumäärää ja auttaisi vähentämään kasvihuonekaasuja sekä muita päästöjä paikallisesti. Tästä syystä tutkimuksen tavoitteena oli selvittää sekä parantaa langattoman latauslaitteen toimintaa ja suorituskykyä. Tutkimus keskittyi aiemmassa tutkimuksessa kehitettyyn kilparadan muotoiseen, induktiiviseen, langattomaan latauslaitteeseen sähköautoille, joka pystyy 20 kW lataustehoon. Tutkimus hyödynsi numeerista FEM laskentaa latauslaitteen simuloimisessa.

Tutkimuksessa latauslaitteen toimintaa analysoitiin käyttäen COMSOL Multiphysics 5.4 ohjelmistoa ja MATLAB ohjelmaa käytettiin tulosten analysoimiseen sekä esittämiseen. Tutkimuksessa saatiin selville, että ajoneuvon ajonopeus langattoman latauksen aikana ei vaikuta latauslaitteen yhteisinduktanssiin. Myös havaittiin, että aiemmassa tutkimuksessa kehitettyä latauslaitetta on mahdollista parantaa muovaamalla latauslaitteen ferriittiytimet uudelleen. Ferriittiytimen uudelleen muovaaminen tarjosi saman yhteisinduktanssin pienemmällä massalla kuin alkuperäinen rakenne. Lisäksi tutkimuksessa vertailtiin kahta erilaista tapaa laskea latauslaitteen hyötysuhde, sekä arvioitiin riittävän verkotuksen tiheyttä FEM laskentaa varten. Tutkimuksessa otetaan myös kantaa langattoman latauslaitteen materiaalien valintaperusteisiin sekä materiaalivalintoihin.

Tutkimustulosten perusteella pääteltiin, että langattomat latauslaitteet ovat käytännöllisiä ja tehokkaita välineitä sähköautojen lataamista varten. Latauslaitteet kykenevät sekä korkeaan tehoon (20 kW) että korkeaan hyötysuhteeseen (yli 90 %), lisäksi ne mahdollistavat latauksen ajoneuvon liikkeen aikana ilman rikkoutuvia kaapeleita ja kontaktipintoja. Myös voitiin päätellä, että tietokonepohjaiset FEM ohjelmat, kuten COMSOL, voivat parantaa latauslaitteiden suorituskykyä ja tarjota uusia innovatiivisia ratkaisuja.

Avainsanat Langatonlataus, Yhteisinduktanssi, Sähköauto, Numeerinen analyysi, FEM, COMSOL

Aalto University
School of Engineering

Aalto University, P.O. BOX 11000, 00076 AALTO
www.aalto.fi

Abstract of master's thesis

Author Jussi Tamminen

Title of thesis Computational analysis of wireless inductive power transfer for charging light-duty electric vehicles

Master programme Mechanical engineering **Code** ENG25

Thesis supervisor Kari Tammi

Thesis advisors Pauli Salminen and Jenni Pippuri-Mäkeläinen

Date 30.1.2020 **Number of pages** 72 **Language** English

Abstract

Wireless chargers can help make electric vehicles more comfortable, which would make electric cars more attractive to consumers, thereby increasing the number of electric cars and helping to reduce greenhouse gases and other emissions locally. Therefore, this study aimed to investigate and improve the performance and efficiency of the wireless charger. The research focused on a racetrack-shaped, inductive, wireless charger for electric vehicles that is capable of 20 kW charging power. The study utilized numerical FEM computation to simulate the charger.

In the study, the operation of the charger was simulated using COMSOL Multiphysics 5.4 software, and MATLAB software was used to analyze and present the results. The study found that the vehicle's driving speed during wireless charging does not affect the mutual inductance of the charger. It was also found that it is possible to improve the charging device developed in the previous study by reforming the ferrite cores of the charging device. Remodeling of the ferrite core provided the same mutual inductance with a lower mass than the original structure. Also, the study compared two different ways to calculate the efficiency of the charger and evaluated sufficient mesh density for the FEM calculation. The study also addressed the selection criteria and material choices of the wireless charger.

Based on the research results, it was concluded that wireless chargers are a practical and effective means for charging electric cars. Chargers are capable of both high power (20 kW) and high efficiency (over 90%), and enable charging during vehicle movement without breakable cables and contacts. It was also concluded that computer-based FEM programs such as COMSOL could improve the performance of wireless chargers and provide new innovative solutions.

Keywords Wireless charging, Mutual inductance, Electric vehicle, Numerical analysis, FEM, COMSOL

Acknowledgments

This master's thesis was written as a part of an EU funded MICEV project, which aims to develop metrology for wireless charging. Furthermore, I had the privilege to work on this project for a couple of years, and I also had the opportunity to write my bachelor's thesis on the topic. After the bachelor's thesis, it felt like an excellent continuation to stay on the same topic, so I ended up to write my master's thesis on the topic as well. However, it must be said that these years have been very challenging but also really educational. Furthermore, I would like to thank all of the partners and colleagues in the MICEV project, and especially thank Vincenzo Cirimele for all the answered questions. Moreover, I would like to thank Kari Tammi for being my supervisor for all these years, and Pauli Salminen and Jenni Pippuri-Mäkeläinen for being my thesis advisors and colleagues. Lastly, I would like to thank my wife, Veera, for always being supportive.

Espoo 30.1.2020

Jussi Tamminen

Jussi Tamminen

Table of Contents

Symbols

SYMBOL	DESCRIPTION	UNIT
A	Vector potential	Wb/m
B	Magnetic field flux density	T
E	Energy or electric field	J or V/m
H	Magnetic field	A/m
I	Current	A
I_L	Current of the equivalent load	A
I_{re}	Receiver coil current	A
I_{re}	Receiver coil voltage	V
I_{tr}	Transmitter coil current	A
j	Imaginary unit	-
J	Current density	A/m^2
M	Mutual inductance	µH
$n_{Cirimele}$	Cirimele's efficiency	%
n_{Thesis}	Thesis' efficiency	%
P	Charging power (general)	W
P_{static}	Charging power (static)	W
P_V	Specific power loss of core material	kW/m^3
R_1	Resistivity of transmitter coil	Ω
R_2	Resistivity of receiver coil	Ω
R_L	Resistance of the equivalent load	Ω
s	Surface	m^2
T	Time	s

SYMBOL	DESCRIPTION	UNIT
t_0	Initial time	s
T_C	Curie temperature	°C
V	Voltage	V
V_L	Voltage of the equivalent load	V
V_{tr}	Transmitter coil voltage	V
v	Volume	m^3
ε	Absolute permittivity $\varepsilon = \varepsilon_0 \varepsilon_r$	As/Vm
ε_0	Permittivity of vacuum (8.854187817)	As/Vm
ε_r	Relative permittivity	-
μ	Absolute permeability $\mu = \mu_0 \mu_r$	H/m
μ_0	Permeability of vacuum ($4\pi\ 10^{-7}$)	H/m
μ_a	Amplitude permeability	-
μ_i	Initial permeability	-
μ_r	Relative permeability	-
ρ	Resistivity	Ωm
σ	Conductivity	S/m
ω	Angular velocity	1/s

Abbreviations

ABBREVIATION	MEANING
AC	Alternating current
CC	Capacitive coupling
DC	Direct current
DR	Driving direction
EV	Electric vehicle
FDM	Frequency-domain model
FDS	Frequency-domain solver
FEM	Finite element method
FS	Full sweep
GA	Ground assembly
HML	Horizontal measurement line
IBC	Impedance boundary condition
IC	Inductive coupling
ICE	Internal combusting engine
IPT	Inductive power transfer
MA	Measurement area
MICEV	Metrology for Inductive Charging of Electric Vehicles
PK	Peak
Polito	Polytechnic University of Turin
RMS	Root mean square
RU	Receiving unit
SD	Sideway direction
STD	Standard deviation
TDM	Time-domain model

ABBREVIATION	MEANING
TDS	Time-domain solver
TU	Transferring unit
VA	Vehicle assembly
VML	Vertical measurement line
WPT	Wireless power transfer

1 Introduction

1.1 Background

Electric vehicles (EV) provide higher efficiency and lower CO2 emission compared to internal combustion engines (ICE), and therefore they are an environmentally friendlier option of transportation. However, EVs tend to have lower operating ranges than they ICE counterparts do. Moreover, the EVs range is limited by the battery capacity (average capacity is 56.9 kWh), which typically provides a range of 309 km [1]. Currently, cabled charging is used for EV charging but is poses few drawbacks such as inconvenient use – the driver must step out of the vehicle and cables exposed to wear and vandalism because charging equipment is located in the open.

Moreover, the battery is needed to recharge daily and the range of the vehicle depends directly on the battery size. Fortunately, wireless charging could overcome the battery size issues and also provide multiple benefits to EV users, such as more comfortable charging – human operation is not needed, longer-range without increasing the cost and the size of the battery, and more durable charging equipment [2].

Dynamic wireless charging increases the vehicle range without increasing the battery size because the battery is charged during driving [3]. Moreover, batteries can be made lighter which directly increases the efficiency of the EV and provides higher range [4]. The charging could occur on specific lanes or before traffic lights. Utilizing the ready-made infrastructure and charging lanes, a city could provide its citizens with easy access to charging and also exploit the possible rush-hours and traffic jams. The charging equipment is covered with a concrete layer, and thus it is protected from vandalism, wear and weather [5]. Wireless charging could also provide advantages outside streets for example, in large warehouses with autonomous robots [3].

1.2 Research problem and objectives

The research problem is how to use the finite element method (FEM) for obtaining the optimal design for wireless chargers. The goal of this thesis is to show the development and the use of a parametric FEM model and to provide tools for analyzing charger performance using mutual inductance and other factors. The mutual inductance is the most significant coupling parameter affecting the charger performance, and therefore, comprehensive maps form mutual inductance are provided [6]. Besides, different modeling approaches are described. Furthermore, new ferrite assemblies wanted to analyze to see if it is possible to increase the charger performance or reduce the overall weight of the charger.

1.3 Scope

The charger under study was provided by Polytechnic University of Turin (Polito), who was one of the partners in the MICEV project [7]. Polito developed the original model of the racetrack-shaped charger and the scope of this thesis is limited to the analysis and development of that charger. Furthermore, the geometry of this charger offer steady charging when vehicle passes over the charger and also provide low road installation cost because the transmitter coil has no ferrite [8][9]. The thesis concentrates on the performance of the wireless charger, including efficiency, transferred power, power losses and material selection. The main focus is on electromagnetic phenomena such as magnetic fields, mutual inductance,

induced losses and currents; factors that can be solved using FEM software. Other aspects are included if they are needed for solving previously mentioned elements. For example, the electronic structure of the charger is considered for efficiency and transferred power, but only at theory level including compensation topologies. Moreover, the actual electrical component selection is not considered nor is the manufacturing and car assembly.

1.4 Research methods

The following computations and results are based on a model computed with COMSOL Multiphysics 5.4 software [10]. COMSOL was selected for the software because it is user-friendly and versatile. Also, Elmer multi-physics software was tested in [11], but COMSOL was found to be more convenient than Elmer for this task. The charger model is a slightly modified version of the one used previously in this project [5], but the geometry remains the same (Figure 1). Post-processing and visualization of data are partly made with MATLAB. Furthermore, all computing was done using powerful PC with Windows 10 and the reported computing times are based on these specs: CPU: Intel(R) Core(TM) i9-7900X CPU @ 3.30GHz, 3312 Mhz, 10 Cores, 20 Logical Processors, GPU: Nvidia Geforce GTX 1080, and RAM of 128 GB. Two different models were created due to different needs. The first model operates in frequency-domain at 85 kHz, and the second model operates with the same 85 kHz frequency in time-domain. Latter can be utilized for transient simulations and velocity testing. However, during the development, it was found that velocity does not affect mutual inductance, and therefore the parametric frequency-domain model is used for the misalignment error analysis due to lighter computational requirements.

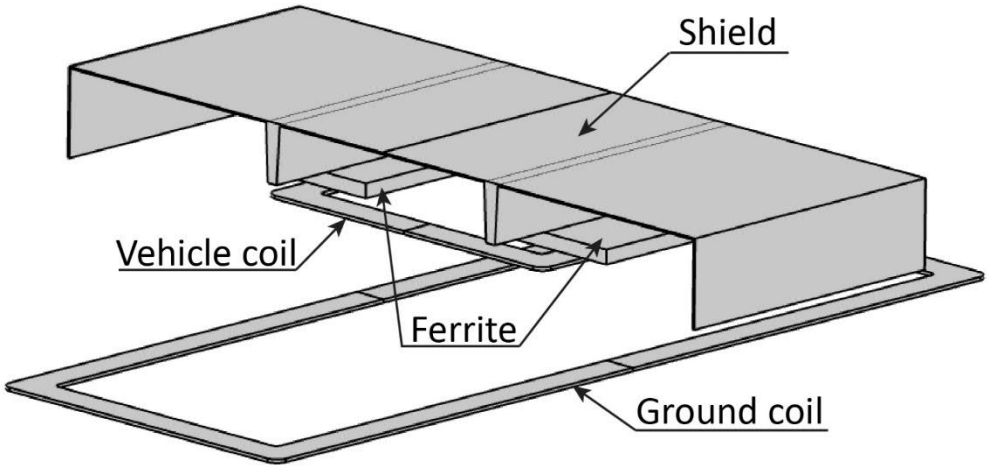

Figure 1. An overview of the "racetrack" model with shield, ferrite blocks, vehicle coil (receiver), and ground coil (transmitter) listed from top to down. The vehicle assembly coil is approximately 62 cm long and 42 cm wide. Ground assembly coil has a width of 62 cm and a length of 162 cm to the direction of travel. Model adapted from [5].

Performance analysis included the evaluation of the mutual inductance for misalignments of ± 1.2 m in driving direction, ± 1 m in sideway direction, and for five air gaps 5 cm, 10 cm, 15 cm, 20 cm and 25 cm. The misalignment analysis had 10 cm steps in driving and sideway directions and simulation containing all of these points for all separation distances are called full sweep (FS). Also, four new ferrite core assemblies were analyzed and two types of calculating efficiency were compared.

2 Materials and methods

2.1 Wireless charging

Wireless charging transfers power over an air gap without cables, for example, with resonating magnetic fields, and therefore it is called wireless power transfer (WPT). Wireless charging can be divided into two categories dynamic wireless charging and static wireless charging [11]. Static wireless charging occurs when the vehicle is stationary during charging like with a personal charger in one's garage. In dynamic wireless charging, the vehicle is on the move during the charging, and therefore, the dynamic charging is a practical way of charging and allows the use of smaller batteries in electric vehicles. Moreover, there are two operating principles of wireless chargers: inductive coupling (IC) and capacitive coupling (CC). IC utilizes magnetic fields, and CC uses electric fields for power transfer, but this thesis considers only the IC that is called inductive power transfer (IPT). The benefits of such charger compared to traditional cabled chargers are; more comfortable use, absence of galvanic contacts, ability to charge during driving, and durability against wear and vandalism. [12]

Wireless power transfer consist of two units; a transferring unit (TU) that is attached to the ground and a receiving unit (RU) that is attached to the vehicle (Figure 2). Other possible names for these units are ground assembly (GA) and vehicle assembly (VA), which is the standard for wireless power transfer for light-duty vehicles [13]. In more detail, the transferring unit has two converters. The first converter is converting the low-frequency AC-current from the power grid to DC-current, and the second converter converts the DC-current into high-frequency AC-current (typically 85 kHz for light-duty electric vehicles [13]). The purpose of these two converters is to control the charging power by adjusting the input voltage and frequency. Likewise, the receiver unit has a rectifier to convert the received AC-current into DC-current suitable for the battery. Moreover, the receiver side has also a boost-converter to maintain a voltage level suitable for battery charging [8]. [5] [12]

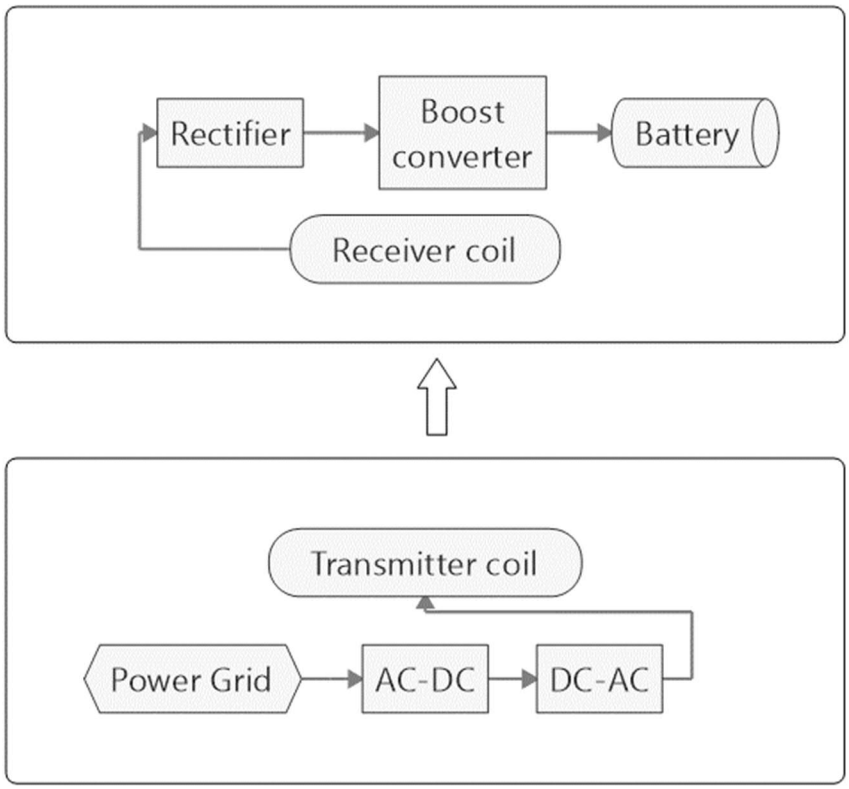

Figure 2. Generalized block diagram of a WPT system. A transmitter side is at the bottom, and the receiver is at the top. Power is flowing from the power grid through the TU and RU to the vehicle battery.

Weak coupling between its sides characterizes WPT since it is used for transferring power over a relatively large air gap. Therefore, to transmit maximum power over the air gap, a reactive part of the power transfer should be compensated. Thus, WPT utilizes resonance between TU and RU to maximize the transferred power. The resonance is acquired using compensation capacitors in TU and RU to eliminate the reactive parts at the operating frequency. Depending on the placement of these capacitors, the compensation is called either parallel or series compensated. Figure 3 shows an example of a series-series compensated system which utilizes series compensation topology in both TU and RU. The compensation offers a couple of advantages such as an increase in power transfer, a decrease in power electronic VA ratings, and an increase in efficiency. Next, the modeling approach is described.[5], [12]

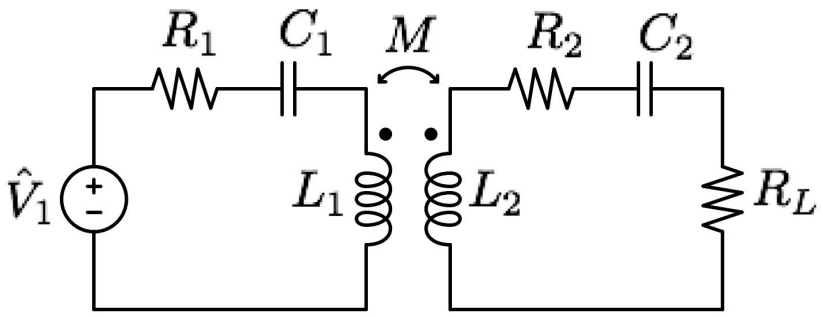

Figure 3. Schematic diagram of series-series compensation topology [5]*. Capacitors C1 and C2 are called compensation capacitors, and they are used to tune the system into resonance.*

2.2 Modeling approach

Wireless charging is possible to simulate with two different types of solvers in COMSOL. These solvers are called time-domain solver (TDS) and frequency-domain solver (FDS). Hence, the models created using these solvers are called time-domain model (TDM) and frequency-domain model (FDM), respectively. Both solvers have their strengths and weaknesses. TDS is more time consuming than FDM, but it consumes less memory and also provides the ability to simulate movements and different current waveforms. Moreover, TDS is capable of simulating any time-varying quantities, while FDS assumes that all quantities are changing sinusoidally relative to time. Figure 4 presents the model development flowchart.

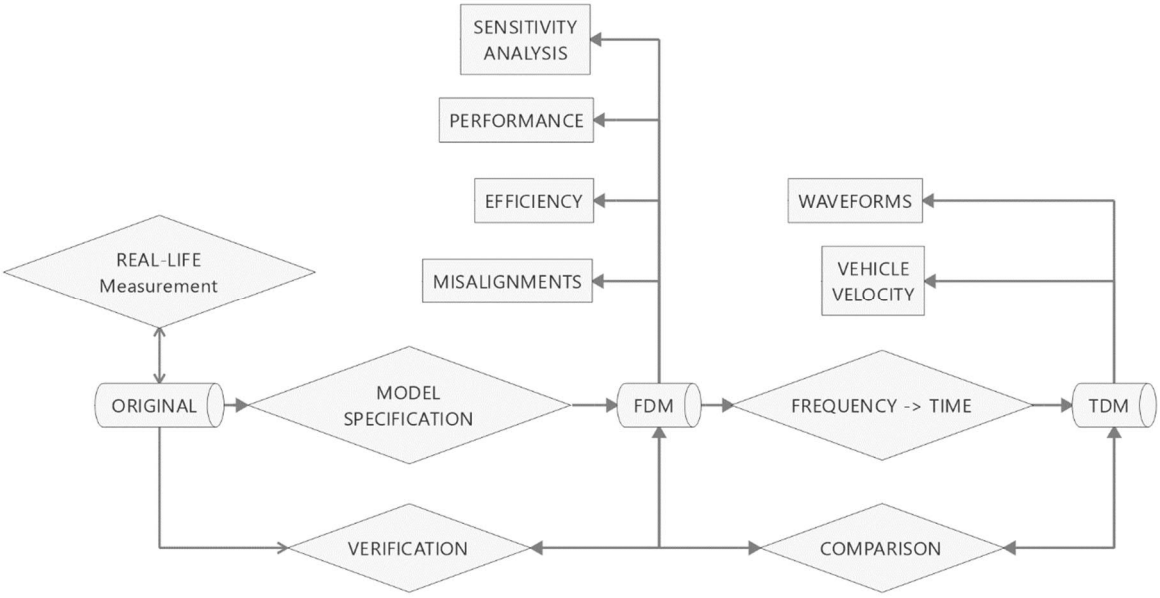

Figure 4. Model development flowchart. The development started with the provided and verified model called original. Next, the original model was specified to meet the requirements of this thesis and to create the FDM, which is used for sensitivity, performance, efficiency and misalignment analysis. Moreover, the FDM was verified by comparing it to the original model. Lastly, the TDM was created by changing the FDS in FDM to TDS, and it verified by comparing it to the FDM.

A chain approach was used for going from the original static model to the TDM with moving coils. The first step was to examine and confirm the original model provided by Polito [5]. Moreover, it was essential to understand the model behavior in order to proceed to a time domain. It was found that an infinite element domain could be used in the FDM to increase the accuracy of the model and reduce the computing time by avoiding unnecessarily large air domain around the model. In addition, some material properties were revised. For example, ferrite properties were changed to match with commercial ferrite material (Ferrocube 3C95) that has low specific power loss at these frequencies and a high relative permeability of 3000. Polito verified the original computational model with real-life measurements [5], and after these slight changes, the new FDM model was verified by comparing it to the original model. After this, a stationary TDM model was done and verified by comparing the results with the new FDM model.

The most significant change in the stationary TDM was a new solver type. A frequency-domain solver has replaced with a time-dependent solver. Moreover, excitation current was defined as a sinusoidal function of time. Then the stationary TDM model was compared to FDM using magnetic fluxdensities at Measurement Lines (ML) (MLs are shown in Figure 6) and mutual inductance between coils. After verification between the FDM and stationary TDM, the vehicle velocity was added to the stationary TDM using moving mesh. Then two speeds of vehicle, 60 km/h, and 600 km/h were simulated.

Already the first simulations showed that the vehicle speed of 60 km/h causes only minor movement during feasible simulation time. That is due to the high excitation frequency of 85 kHz, which needs very tiny time-stepping, and thereby, the coil hardly moved during the (real-time) simulations. Mutual inductance was compared in both cases: stationary and 60 km/h and no significant difference were noticed. This leads to pre-conclusion that the vehicle movement might not have a significant effect on charger performance since the vehicle speed is so low compared to the charging frequency. In any case, the minor movement did not complicate the simulations since the mesh can withstand these minor deformations without re-meshing. In addition to 60 km/h, the higher velocity of 600 km/h was also computed with the model. The results indicated that the higher velocity did not either have any significant effect on mutual inductance in the TDM model. That leads to the conclusion that at least the movements with velocities under 600 km/h have an insignificant effect on the mutual inductance and coupling factor between the coils. Besides, the dynamic TDM is very computationally heavy, and therefore only short real-time simulations could be done (a couple of sinusoidal cycles). These results indicate that correct results can be achieved more comfortably by using parametric sweep in FDM, and therefore, the full solution for different misalignments can be acquired by calculating multiple individual solutions that are combined into one.

2.3 Mutual inductance and performance analysis

Performance analysis includes the evaluation of efficiency, induced losses, and power, and therefore few assumptions are needed. Although most of the power electronics behind the coils are not considered, the charger was assumed to be series-series compensated to justify the used equations (Figure 3). Mutual inductance is an essential property of an inductive charger because it indicates the efficiency of the charger; high mutual inductance enables high efficiency but demands high input voltage also [14]. For series-series and parallel-series compensation, the coil efficiency can be calculated using the following equations

$$\eta_{Cirimele's,SS,PS} = \frac{R_L I_L^2}{R_1 I_{tr}^2 + R_2 I_{re}^2 + R_L I_L^2} = \frac{R_L}{(R_L + R_2)(1 + R_1 \frac{R_L + R_2}{\omega_0^2 M^2})} \quad (1)$$

$$\eta_{Thesis',SS,PS} = \frac{R_L I_L^2}{R_1 I_{tr}^2 + R_2 I_{re}^2 + R_L I_L^2 + induced\ losses} \quad (2)$$

where R_L, R_1, R_2, ω_0 and M denote equivalent load and coils resistances, resonance angular velocity, and mutual inductance, respectively [5]. Furthermore, I_L, I_{tr}, I_{re} are referred to as current of the load, transmitter coil and receiver coil, respectively. Induced losses describes

the losses caused by eddy currents in the ferrite core and the shield. Two equations for efficiency are used to compare the possible differences between them. Equation (1) was introduced in [5] by Cirimele and it is called Cirimele's efficiency in this thesis. The advantage of Cirimele's efficiency is that it is described without currents. The equation (2) is a slightly modified version of Cirimele's efficiency and it is called Thesis' efficiency. Thesis' efficiency uses the power form of Cirimele's efficiency and introduces the induced losses to the equation.
As both of the equations show, also the resonating frequency can be increased for higher efficiency. However, increasing the frequency will also increase losses due to skin and proximity effects [5]. Besides, SAE standard J2954 fixed the operating frequency at 85 kHz with a tuning variance from 79 kHz to 90 kHz [15]. R_1 and R_2 can be minimized to increase the efficiencies, but they are properties of the coils and are determined by the wire diameter in the coils, and are thereby out of the scope of this thesis. R_L, on the other hand, has an optimal value based on R_1 and R_2, but it is also governed by a battery and power electronics on the receiver side. Besides, Cirimele provides a value of 3.65 Ω for R_L in the original model and it was decided to use also for the created FDM and TDM. Furthermore, Since all variables but mutual inductance are somewhat locked, the simplest way to affect the efficiency is to increase mutual inductance. Nevertheless, after the design and manufacturing of the charger, the mutual inductance is the only property that can be affected. Thus, mutual inductance must be evaluated accurately.

Mutual inductance can be evaluated in two ways in COMSOL i) calculating the fraction between receiver voltage and transmitter current

$$M = \frac{V_{re}}{j\omega I_{tr}}, \tag{3}$$

ii) calculating the integral over the volume of the receiver:

$$M = \int \frac{\bar{A}\bar{J}}{I_{tr} I_{re}} dv_2 . \tag{4}$$

where $V_{re}, \bar{J}, \bar{A}$ and j are referred to as receiver voltage, vector potential, current density, and the imaginary unit, respectively. These two methods for obtaining the mutual inductance have only minor differences in the values and that may be a numerical rounding error or equivalent since they are calculated in such different ways. Nevertheless, the error is insignificant.

Performance and efficiency are assessed in two phases. First, the mutual inductance is obtained for all studied misalignments using COMSOL with nominal currents. Table 1 present the nominal currents and other nominal parameters provided by Cirimele. Then, the acquired mutual inductances for different misalignments are used for calculation of proper transmitter currents for different for all misalignments in order to maintain the power under the nominal power. Transmitter current is needed to modify for different misalignments in order to maintain the power at a nominal level, without tuning, the power will rise to unreal values with small air gaps. Cirimele's thesis is used as a reference for nominal power since it introduced the archetype of this charger model [5].

Moreover, the receiver current is also tuned to match the transferred power. The currents are tuned with MATLAB which provides a proper transmitter and receiver currents for all misalignments. So for all misalignments, the transmitter current is kept under nominal transmitter current and also the receiver current is kept under the nominal receiver current. When desired transmitter currents are acquired, all misalignments are simulated again with the tuned currents. Figure 5 presents the tuning process.

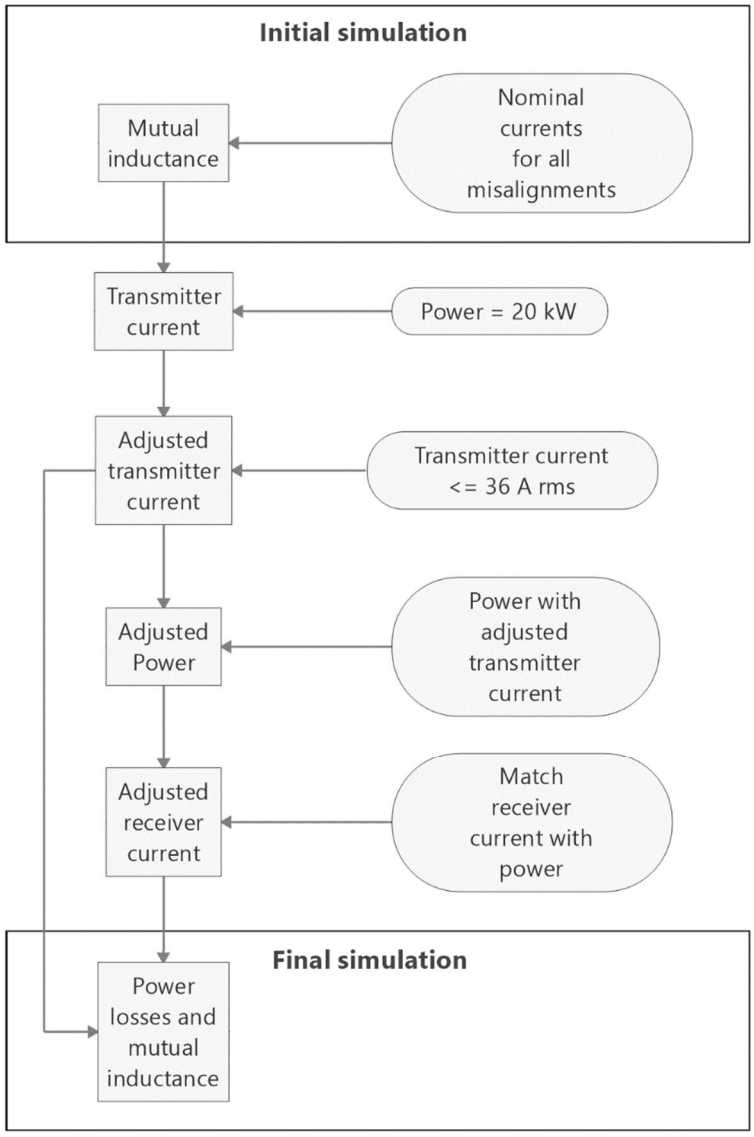

Figure 5. Performance analysis' tuning process. First, mutual inductances for all misalignments were obtained through initial simulation. Then the transmitter currents were modified to get 20 kW power for all misalignments. After that, there were very high currents for misalignments were mutual inductance was low. Then, the transmitter current was limited to 36 A RMS and powers were calculated. At this step, the transmitter currents and powers were set correctly, but receiver currents were unknown. Therefore, the last step was to calculate the correct receiver currents for all misalignments based on the power. Lastly, the whole simulation was rerun providing the correct results for induced losses. Moreover, the mutual inductance remains almost the same during this process which justifies it.

After the model was tuned, it was ready for loss and efficiency analysis. Efficiencies were evaluated as described earlier, and evaluation of induced losses are described in chapters 2.4.2 and 2.4.3.

Transferred power can be evaluated through transferred energy. Transferred energy over time T can be derived using the following equations

$$i_{re}(t) = \frac{V_L(t)}{R_L} = \frac{1}{R_L}\left(M(t)\frac{di_{tr}(t)}{dt} + i_{tr}(t)\frac{dM(t)}{dt}\right), \tag{5}$$

$$P(t) = R_L i_{re}^2(t) = \frac{1}{R_L}\left(M(t)\frac{di_{tr}(t)}{dt} + i_{tr}(t)\frac{dM(t)}{dt}\right)^2, \tag{6}$$

$$E = \int_{t_0}^{t_0+T} P(t)dt = \int_{t_0}^{t_0+T} \frac{1}{R_L}\left(M(t)\frac{di_{tr}(t)}{dt} + i_{tr}(t)\frac{dM(t)}{dt}\right)^2 dt, \tag{7}$$

Where, V_L referred to as the voltage of the equivalent load (battery) [9]. Moreover, the average power is the power equivalent to transfer the same energy,

$$P = \frac{1}{T}\int_{t_0}^{t_0+T} P(t)dt = \frac{1}{T}\int_{t_0}^{t_0+T} \frac{1}{R_L}\left(M(t)\frac{di_{tr}(t)}{dt} + i_{tr}(t)\frac{dM(t)}{dt}\right)^2 dt. \tag{8}$$

In equations from (5) to (8), the mutual inductance M is obtained from simulations and i_{tr}, i_{re} are the input parameters for the simulations, as described previously. Equation (8) is valid both dynamic and static charging, but it can be shortened for static charging,

$$P_{static} = \frac{1}{T}\int_{t_0}^{t_0+T} \frac{1}{R_L}\left(M\frac{di_{tr}(t)}{dt}\right)^2 dt, \tag{9}$$

since for static charging, the mutual inductance is constant. As the previous equations (8) and (9) show, the transferred power is proportional to i_{re}. Thus, the charging power can be increased if tthe transmitter current is increased.

In addition, the magnetic flux densities were measured for the performance analysis and for especially for comparison between FDM and TDM models in chapter 2.5. Two measurement lines, Vertical Measurement Line (VML) and Horizontal Measurement Line (HML), were used for that purpose, and magnetic flux densities were evaluated on these lines (Figure 6).

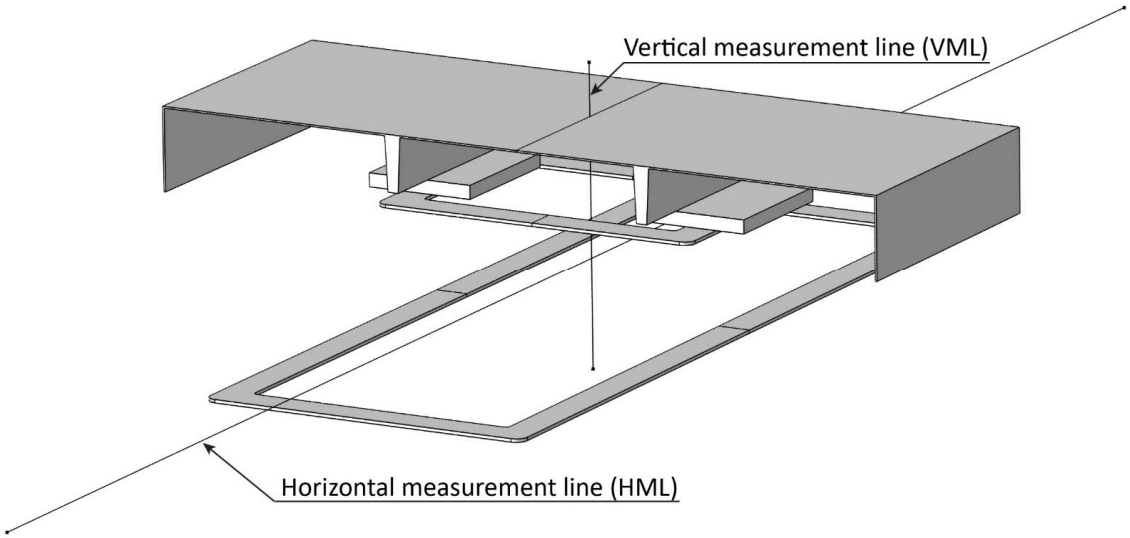

Figure 6. Measurement lines relative to the charger geometry. The line between the coils is referred to as a horizontal measurement line (HML), and the line going through the coils is referred to as a vertical measurement line (VML). These lines have the following lengths; HML 4 m and VML 0.55 m. The direction of HML can be neglected due to symmetry, but VML is pointing upwards.

The magnitudes of the magnetic flux densities in these lines provide a good approximation about the charger behavior, and thus, this data is useful for the analysis and comparison.

2.4 Model specification

Now, when the overall modeling principles are introduced, the models are specified more precisely. The specification includes mesh validation, selecting core and shield materials, and the validation of impedance boundary condition. Table 1 present the nominal parameters of the charger provided by Cirimele's doctoral thesis.

Table 1. Nominal parameters of the charger.

Parameter	Value	Unit
Nominal power	20	kW
Nominal mutual inductance	14.2	μH
Operating frequency	85	kHz
Primary coil current RMS	36	A
Primary coil current PK	50.912	A
Secondary coil current RMS	75	A
Secondary coil current PK	106.066	A
Equivalent load	3.65	Ω

Parameter	Value	Unit
Coils distance	0.25	m
X misalignment	0	m
Y misalignment	0	m

2.4.1 Mesh validation

Specification starts with mesh selection. In general, selecting an appropriate mesh for models is a significant task for any FEM problem. A finer mesh will provide more accurate results, but more importantly, some phenomena might not be modeled at all with too coarse mesh. Such phenomena are for example boundary layer of fluid flow (computational fluid dynamics CFD) and skin effect of alternating current. However, the finer mesh will also demand more computing resources and takes a longer time to solve. Therefore, the designer has to do a compromise between accuracy and computing efforts. Sometimes, different boundary conditions can also be used to make the model smaller without losing accuracy, for example through impedance boundary and infinite element domain conditions. Skin effect and boundary conditions are considered in Paragraph 2.4.4 but this paragraph concentrates only on computing efforts and density of the mesh.
COMSOL provides a physics controlled meshes where the user can set the desired mesh size from extremely coarse to extremely fine. In this thesis, four of these mesh sizes, normal, fine, finer and extra-fine, are compared. The overviews of these four meshes are illustrated in Figure 7 to Figure 10.

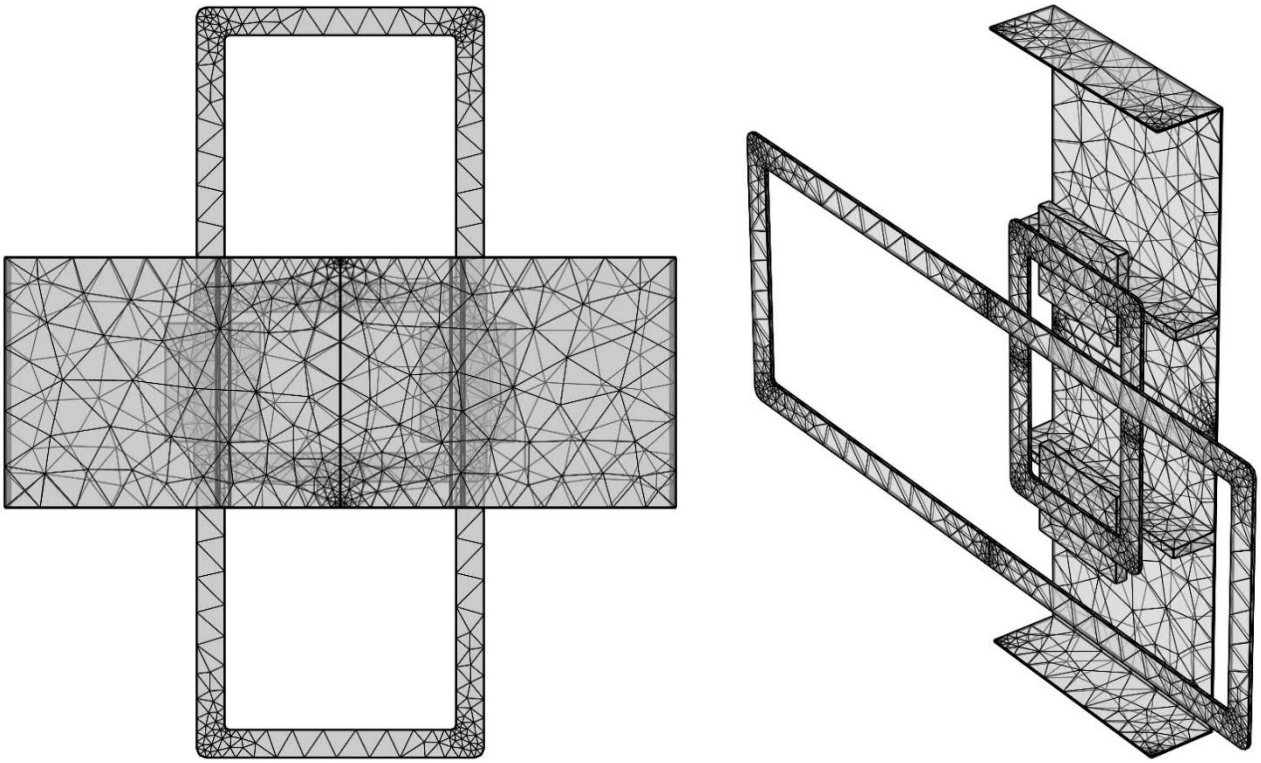

Figure 7. Normal mesh size. Normal mesh is the least demanding computing-wise out of the meshes under study. Notably, the transmitter coil has coarse mesh.

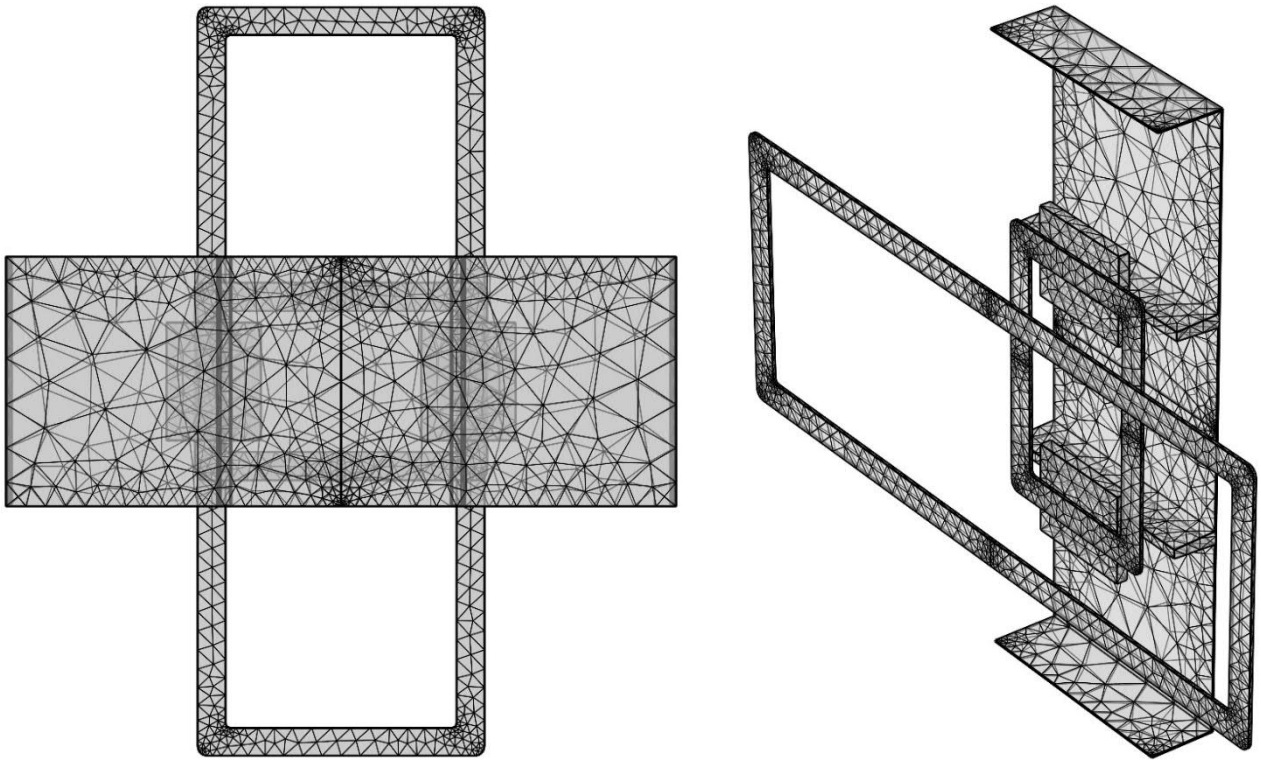

Figure 8. Fine mesh size. With Fine mesh, the edges of the aluminum shield have been meshed with smaller elements than with the Normal mesh. Fine mesh size was used for most of the parametric simulations when multiple solutions were needed.

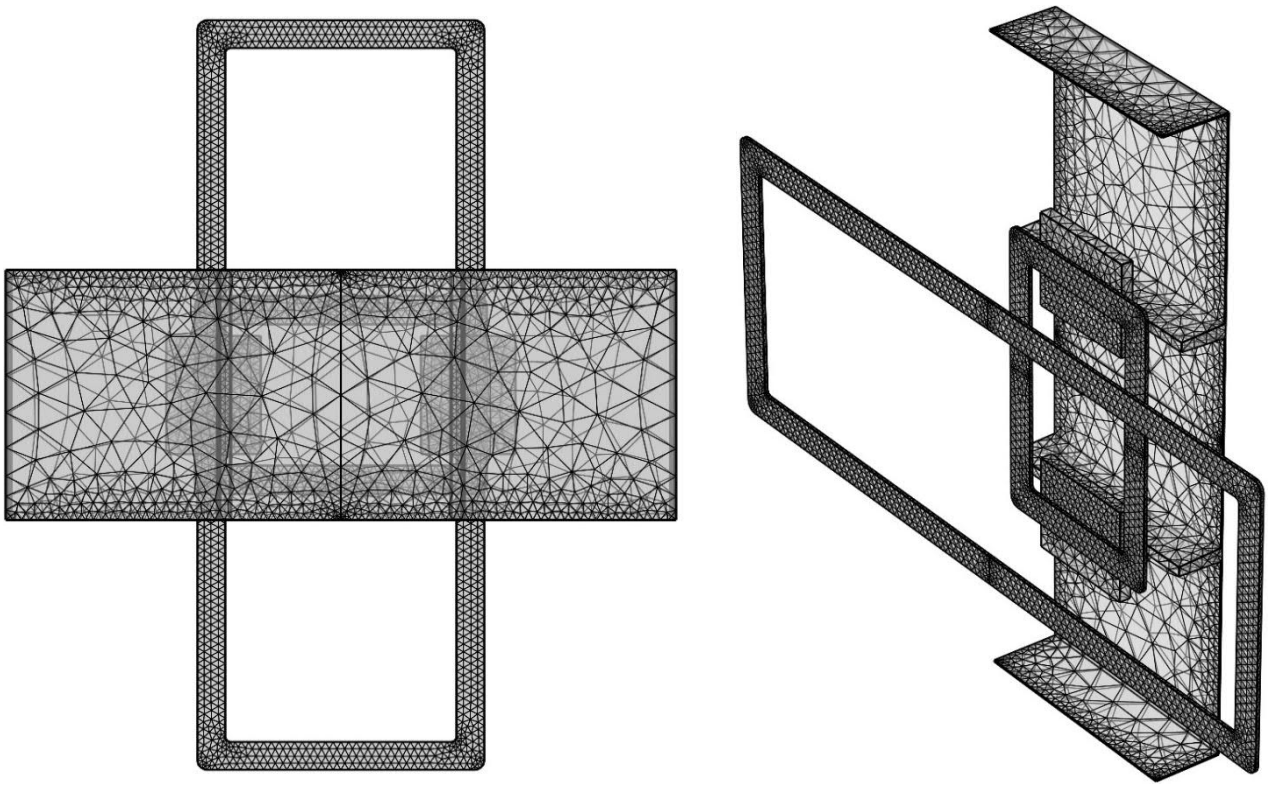

Figure 9. Finer mesh size. Finer mesh size provides rather dense mesh which is still usable for misalignment analysis.

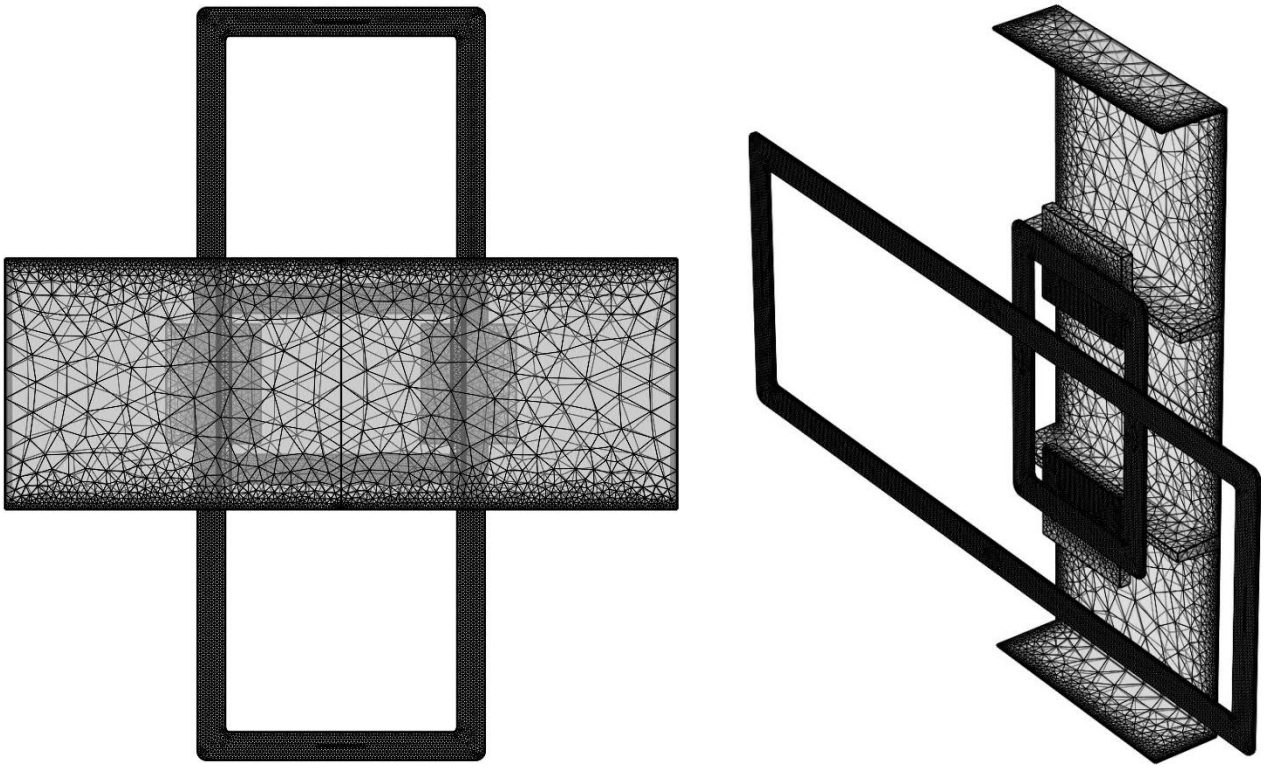

Figure 10. Extra-fine mesh size. Extra-fine mesh size provides the most accurate results of these four mesh sizes but it is too heavy for misalignment analysis. However, this high-density mesh can be used for example to the few of the most interesting simulations.

In conclusion, all of these COMSOL's physics controlled meshes are prioritizing the edges of aluminum shield and coils which seems to be a quite effective meshing strategy. Next, the FDM is simulated with all of these four meshes in nominal conditions with two air gaps 20 and 25 cm (Table 1), and the results are presented in Table 2, Table 3, Figure 11, Figure 12, Figure 13 and Figure 14. First, Table 2 gives an overview of the element counts and computation times for all four meshes.

Table 2. Element numbers and computing time for one solution and for full sweep (FS). The full sweep includes one quadrant of the possible misalignments: 0 – 1.2 m for driving direction (DR), 0 – 1 m for sideway direction (SD) and all five separation distances. Full sweep totals (11x13x5) 715 solutions and it is latter mirrored in MATLAB to produce the full maps for ranges ± 1.2 m in DR and ± 1 m in SD. The computing times for FS were acquired by multiplying the time for one solution with 715 respectively. Simulations were made with PC described in paragraph 1.4.

Mesh	Elements	Time for one (s)	Time for FS (h)
Extra-fine	1915418 domain elements 159836 boundary elements 6275 edge elements.	1059	210
Finer	370065 domain elements 35591 boundary elements 3004 edge elements	206	40.3
Fine	107891 domain elements 11800 boundary elements 1749 edge elements	59	11.7
Normal	59357 domain elements 7519 boundary elements 1377 edge elements	43	8.5

As Table 2 shows, the element count is proportional to the mesh density. Extra-fine having the most element and Normal having the least. The element count will further affect the computing times. Thus, making the Normal mesh the most desired one. Moreover, solving FS for Normal and Fine meshes is possible in one day but Extra-fine mesh takes over a week. Next, the magnetic flux densities with the meshes are compared under nominal conditions. Figure 11, Figure 12, Figure 13 and Figure 14 show the distribution of the magnetic flux density at the two measurement lines HML and VLM for air gaps 20 cm and 25 cm.

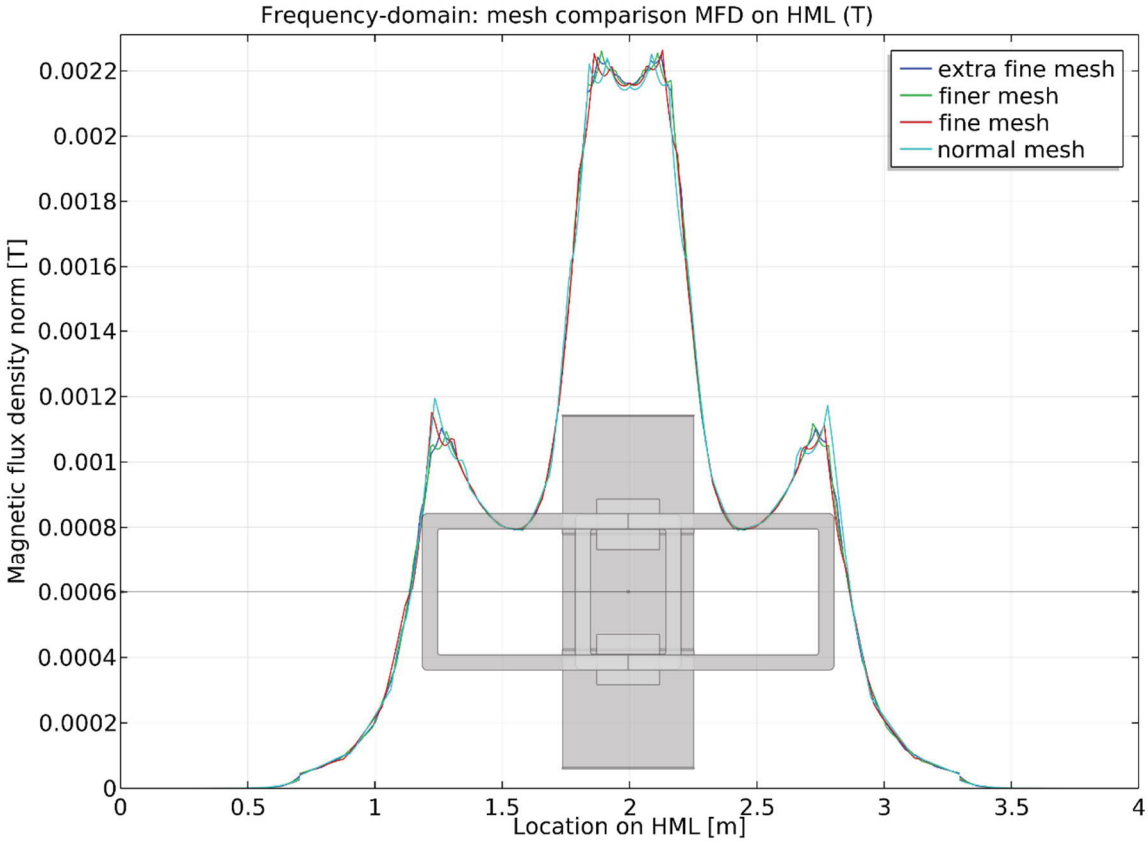

Figure 11. Comparison between four different physics controlled meshes with an air gap of 20 cm. Comparison is based on magnetic flux density on HML with Normal, Fine, Finer and Extra-fine meshes. The schematic of the charger geometry is illustrated on the chart as well. Fine and normal meshes produce pikes on top of the ends of the transmitter and receiver coils while Fine and Extra-fine meshes produce smoother curves. Nevertheless, in most parts, the difference between meshes is little and the curves follow each other very well.

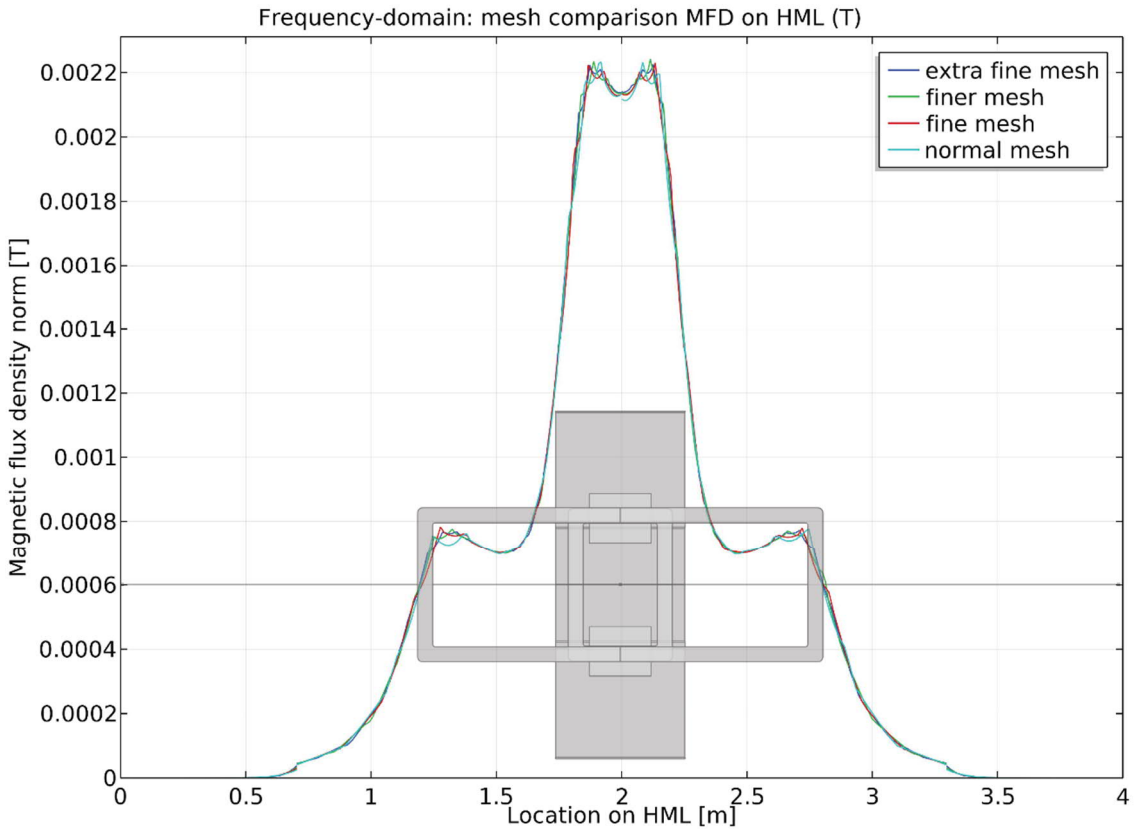

Figure 12. Comparison between four different physics controlled meshes with an air gap of 25 cm. Comparison is based on magnetic flux density on HML with Normal, Fine, Finer and Extra-fine meshes. The schematic of the charger geometry is illustrated on the chart as well. With this 25 air gap, the meshes match each other even better than with a 20 cm air gap as in the previous picture.

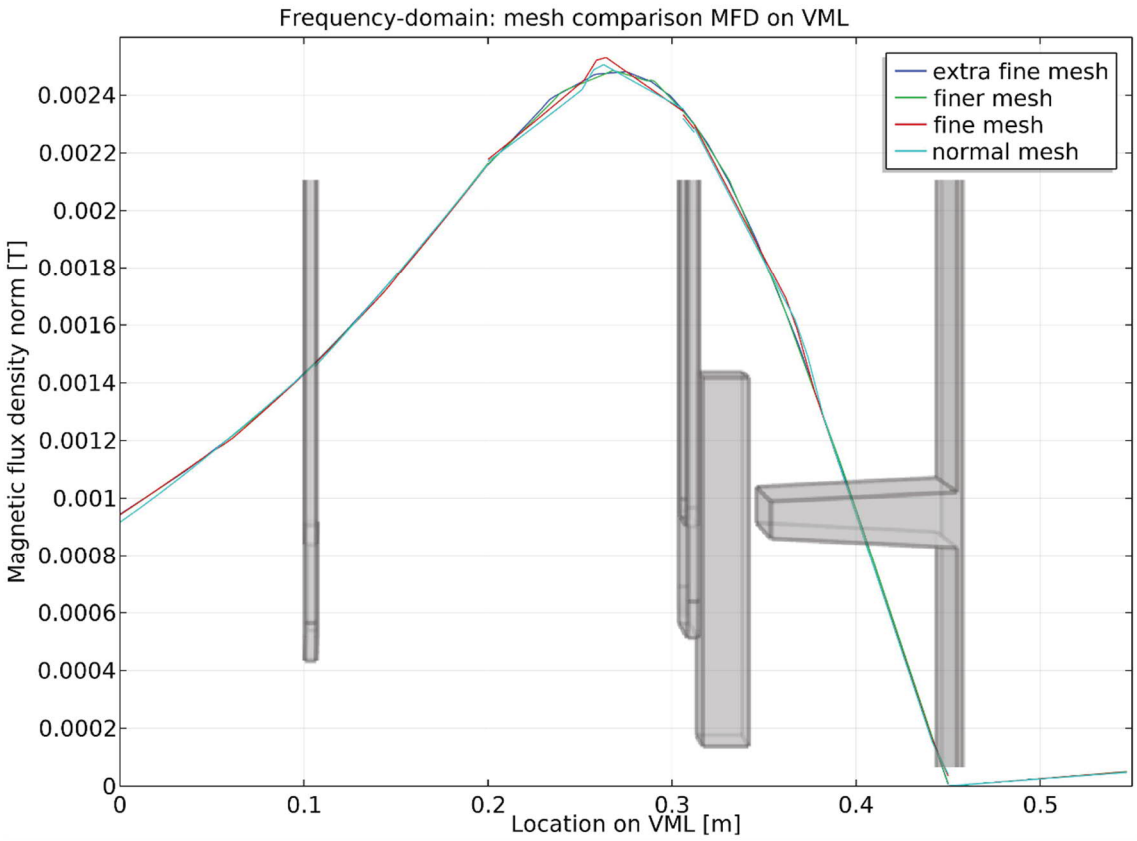

Figure 13. Comparison between four different physics controlled meshes with an air gap of 20 cm. Comparison is based on magnetic flux density on VML with Normal, Fine, Finer and Extra-fine meshes. The schematic of the charger geometry is illustrated on the chart as well. Finer and Extra-fine meshes produce smoothest graphs while Fine and Normal meshes have crooks near of the receiver coil. However, these minor defects do not affect the solution much and in most parts, the meshes match each other well.

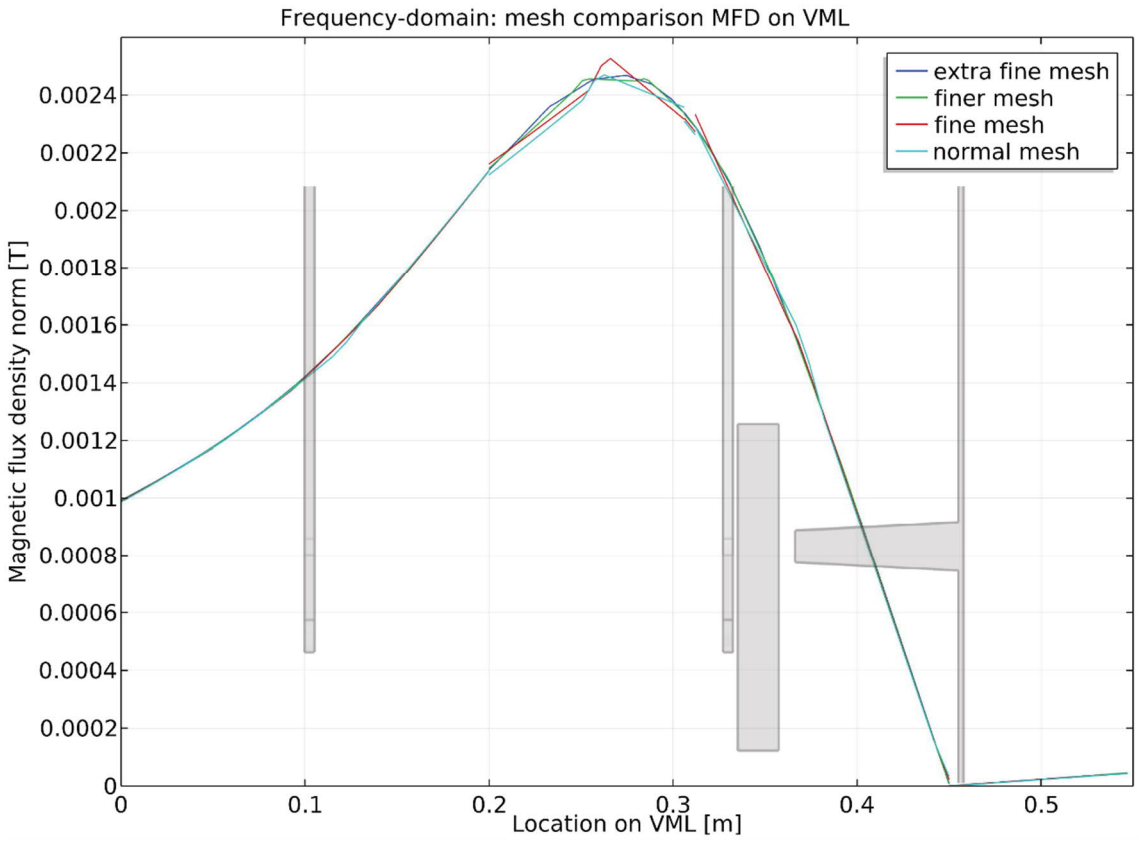

Figure 14. Comparison between four different physics controlled meshes with an air gap of 25 cm. Comparison is based on magnetic flux density on VML with Normal, Fine, Finer and Extra-fine meshes. The schematic of the charger geometry is illustrated on the chart as well. Finer and Extra-fine meshes produce smoothest graphs while Fine and Normal meshes have crooks near of the receiver coil. However, these minor defects do not affect the solution much and in most parts, the meshes match each other even better than with a 20 cm air gap.

As previous figures Figure 11, Figure 12, Figure 13, and Figure 14 showed, the four meshes produce similar graphs for magnetic flux densities at the measurement lines. Thus, it can be concluded that already the coarsest mesh can model all phenomena that are included in the densest mesh. At least, if there is any phenomenon included in the densest mesh that is not modeled with the coarsest mesh, it cannot have much effect. Next, Table 3 compares the change in mutual inductance and ferrite core and shield losses with air gaps 20 cm and 25 cm.

Table 3. Mesh comparison in terms of mutual inductance, ferrite core loss, and shield loss for air gaps 20 cm and 25 cm. An increase in the mesh density will also affect the mentioned parameters. However, this change is small and smooth and not a leap-like. Values for the 20 cm air gap are in parenthesis.

Mesh	Mutual inductance (µH)	Ferrite core loss (W)	Shield loss (W)
Extra-fine	-14.669 (-18.204)	7.7920 (7.8260)	63.934 (65.193)

Mesh	Mutual inductance (μH)	Ferrite core loss (W)	Shield loss (W)
Finer	-14.635 (-18.162)	7.7621 (7.7984)	65.081 (66.456)
Fine	-14.565 (-18.096)	7.7059 (7.7578)	66.952 (68.373)
Normal	-14.512 (-18.016)	7.6941 (7.7325)	67.384 (68.404)

As Table 3 showed, the values of mutual inductance, ferrite core losses, and shield losses are changing little when going from coarser mesh to finer mesh. However, the change is minimal and there is no big jump between the finest and coarsest meshes, which suggests that all of the tested meshes are more or less suitable for the use of this thesis. At least, all of the significant phenomena are included in the analysis for all four meshes. Otherwise, there should be greater change in the values. Of course, there is a slight possibility that even the densest mesh is missing some phenomena, but it is considered unlikely. Moreover, the densest mesh is already very heavy computationally so it is not practicable to increase the mesh density further as then the full parametric simulation becomes unfeasible.

2.4.2 Selecting ferrite

Ferrite structures are used for guiding the magnetic fields efficiently, and thus they are a crucial part of the charger. Moreover, ferrite structures affect the overall efficiency of the charger in two ways. Firstly, guiding the magnetic fields from the transmitter coil through the receiver coil affecting directly to the mutual inductance. Better guiding increases mutual inductance and thus increasing efficiency, as described in equation (1). Secondly, ferrite structures cause losses due to eddy currents. These eddy current losses can be calculated using integral over the surface and depend on the chosen material, geometry, and excitation. The material and geometry of the ferrite are needed to choose carefully; a little effort in the design phase can save much energy and money over charger lifetime. For that reason, three different materials and four geometries are analyzed. Materials are compared next and the geometries later on.

Ferroxcube manufactures the three ferrite materials, 3C81, 3C95 and 3F3, chosen for the comparison. In the original model, 3F3 was used because of the stable permeability at the working frequency and low specific power losses [5]. However, 3C81 and 3C95 seemed to be good options as well, and therefore, they are added in the study. Moreover, 3C81 and 3C95 have similar material properties as 3F3 and this study is intentionally kept close to the properties of the original ferrite. It was wanted to know how the change in ferrite core material properties affect the charger and perform an elementary sensitivity analysis. This knowledge can be used in the future for selecting even more efficient core materials. Besides, Ferroxcube alone produces too many different ferrites to simulate them individually in the scope of the thesis practically. Therefore, the primary comparison and selection process is introduced. The comparison was made in two parts - first, the manufacturer's datasheets are analyzed and then induced losses are simulated in COMSOL.

All three mentioned ferrite materials are manganese-zinc ferrites based on the MnZn composition with a general chemical formula of

$$\mathrm{Mn}_{\delta}Zn_{(1-\delta)}Fe_2O_4 \text{ [16].} \quad (10)$$

Another common ferrite type is nickel-zinc ferrite based on the NiZn with a general chemical formula of

$$Ni_{\delta}Zn_{(1-\delta)}Fe_2O_4 \text{ [16].} \quad (11)$$

Table 4, Table 5, and Table 6 show the general properties for MnZn and NiZn ferrites. In general, MnZn ferrites have lower resistivities than NiZn ferrites, and MnZn ferrites maintain these values better than NiZn ferrites as a function of temperature and frequency. However, changing frequency is not an issue as the operating frequency of wireless power transfer for light-duty vehicles is fixed at single nominal frequency of 85 kHz with a tuning variation from 79 kHz to 90 kHz [15] but, the stable resistivity of the manganese-zinc ferrites can be considered an advantage since EV could be exposed to broad temperature range.

Table 4. General electrical resistivity for MnZn and NiZn ferries as a function of temperature [16].

Temperature (°C)	**MnZn resistivity (Ωm)**	**NiZn resistivity (Ωm)**
-20	≈ 10	N/A
0	≈ 7	≈ 5.10^7
20	≈ 4	≈ 10^7
60	≈ 2	≈ 10^6
100	≈ 1	≈ 10^5

Table 5. General electrical resistivity for MnZn and NiZn ferries as a function of frequency [16].

Frequency (MHz)	**MnZn resistivity (Ωm)**	**NiZn resistivity (Ωm)**
0.1	≈ 2	≈ 10^5
1	≈ 0.5	≈ 5.10^4
10	≈ 0.1	≈ 10^4
100	≈ 0.01	≈ 10^3

Table 6. General relative permittivity for MnZn and NiZn ferries as a function of frequency [16].

Frequency (MHz)	MnZn relative permittivity (ε_r)	NiZn relative permittivity (ε_r)
0.001	N/A	≈ 100
0.01	N/A	≈ 50
0.1	$\approx 2.10^5$	N/A
1	$\approx 10^5$	≈ 25
10	$\approx 5.10^4$	≈ 15
100	$\approx 10^4$	≈ 12

Next, Table 7 presents initial relative permeability, amplitude relative permeability, magnetic flux density, electrical resistivity, Curie temperature and density for the three ferrite materials. Furthermore, the values of the initial relative permeabilities were chosen for the value of relative permeabilities for the simulations.

Table 7. Material properties of 3C81, 3C95 and 3F3 [16].

Property	Conditions	3C81	3C95	3F3	Unit
μ_i	25 °C; ≤10 kHz; 0.25 mT	2700±20%	3000±20%	2000±20%	-
μ_a	100 °C; 25 kHz; 200 mT	5500±20%	≈5 000	≈ 4000	-
B	25 °C; 10 kHz; 1200 A/m	≈ 450	≈ 530	≈ 440	mT
	25 °C; 10 kHz; 1200 A/m	≈ 360	≈ 290	≈ 370	
ρ	DC; 25 °C	≈ 1	≈ 5	≈ 2	Ωm
T_C	-	≥ 210	≥ 215	≥ 200	°C
Density	-	≈ 4800	≈ 4800	≈ 4750	kg/m^3

Considering the stability of the initial relative permeability, Figure 15 presents the initial relative permeabilities as a function of temperature. The figures show that 3C95 has the most stable initial permeability curve in the typical temperature range of an EV. 3C95 also seems to have the lowest specific power loss of the three materials. Figure 16 shows that at the

operating conditions of the charger (100 kHz and 100 mT), 3C95 has the smallest specific power loss while 3F3 having the highest. Nevertheless, all of the materials have a thin B-H loop with enough high saturation limit (Figure 17). Thin B-H loop indicates low losses while a high saturation limit allows the material to operate on the linear area [17]. As a result of these traits, high and steady permeability maintaining stable performance, and a low specific power loss, 3C95 can be considered the best option according to the manufacturer's datasheets. Next, the materials are evaluated more trough simulation and numerical analysis.

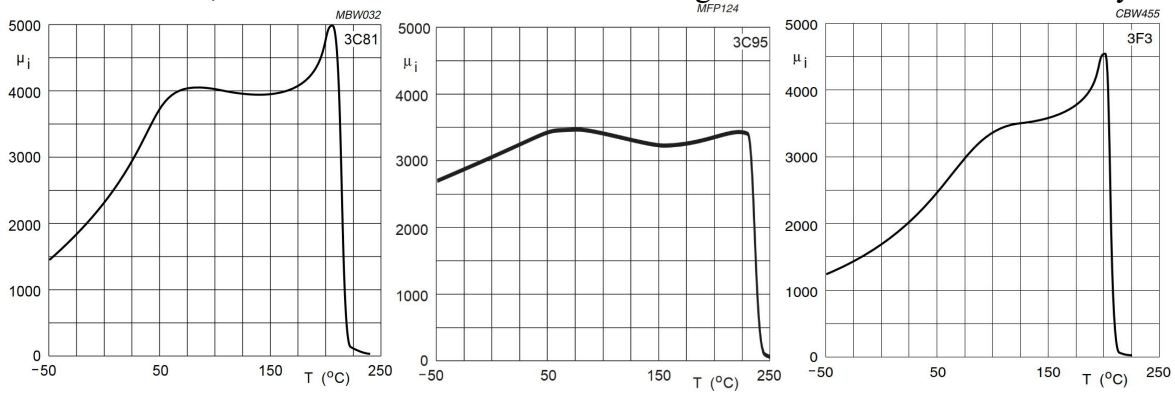

Figure 15; a, b and c. The initial relative permeability of 3C81 (a), 3C95 (b) and 3F3 (c) [16]. *Figure shows that 3C95 provides the most stable relative permeability as a function of time.*

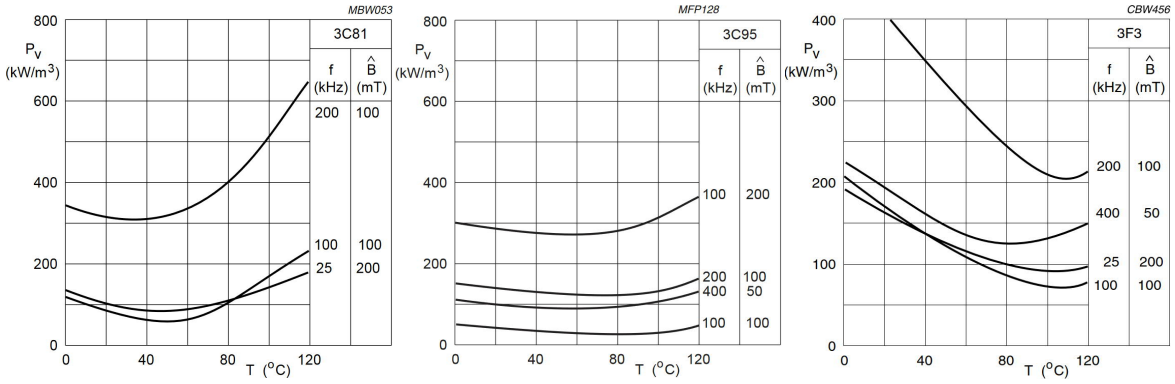

Figure 16; a, b and c. Specific power losses of 3C81 (a), 3C95 (b) and 3F3 (c) [16]. *The lines for 100 kHz and 100 mT describe best the actual usage of the charger. The middle sub-figure shows that 3C95 has the smallest specific power loss of the three materials.*

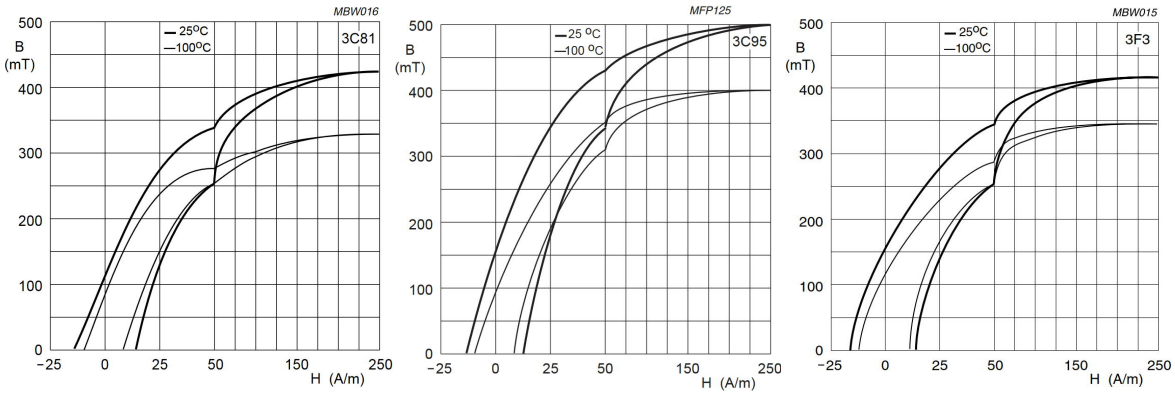

Figure 17; a, b and c. Typical B-H loops of 3C81 (a), 3C95 (b) and 3F3 (c) [16]. *All three materials have a thin B-H loop, which is typical for soft magnetic materials. Moreover, all of the materials have saturation limits high enough for the charger.*

The analysis of the manufacturer's datasheets hints that 3C95 seems to be the best option, but the actual performance can be revealed only by simulating the materials. The numerical analysis reveals the effects of three main ferrite properties, permeability, permittivity and resistivity. The materials were studied in terms of mutual inductance, shield losses and ferrite core losses. High mutual inductance and low losses indicate decent performance and vice versa.
The analysis involves the three specified ferrites (3C81, 3C95, and 3F3), including all possible combinations of the permeabilities and resistivities totaling nine different combinations (Table 8). In addition, three different permittivities 1, 100 and 100000 were added to the analysis totaling 27 different material combinations. This narrow sensitivity analysis uncovers the individual effect of each material property even if there might not be existent material for all the possible material property combinations. However, it gives the guidelines for choosing the best material in future research.

Table 8. Nominal material parameters for 3C81, 3C95 and 3F3 [18].

Material	Resistivity (Ωm)	Relative permeability
3C81	1	2700
3C95	5	3000
3F3	2	2000

The charger was analyzed at its nominal position (zero misalignments, 25 cm air gap). Ferrite losses were evaluated using COMSOL's ready-made "Volumetric loss density, electromagnetic" (mf.Qh) variable and integration over the ferrite core volume,

$$P_{loss} = \int_{V_{Ferrite}} \text{mf.Qh}\, dv\,. \tag{12}$$

To confirm the COMSOL's ready-made variable, the losses were also calculated with

$$P_{loss} = \frac{1}{2} \int_{V_{ferrite}} \vec{J} \cdot \vec{E}^{*}\, dv\,, \tag{13}$$

where $\vec{J}$ and $\vec{E}$ are denoted current density and electric field. It turned out that these two methods give exactly the same result for the ferrite losses and therefore, the equations can be interpreted as correct. Mutual inductance was evaluated as described in 2.3 and shield losses similarly as ferrite core, as will be described in 2.4.3. Figure 18 shows the results of this analysis.

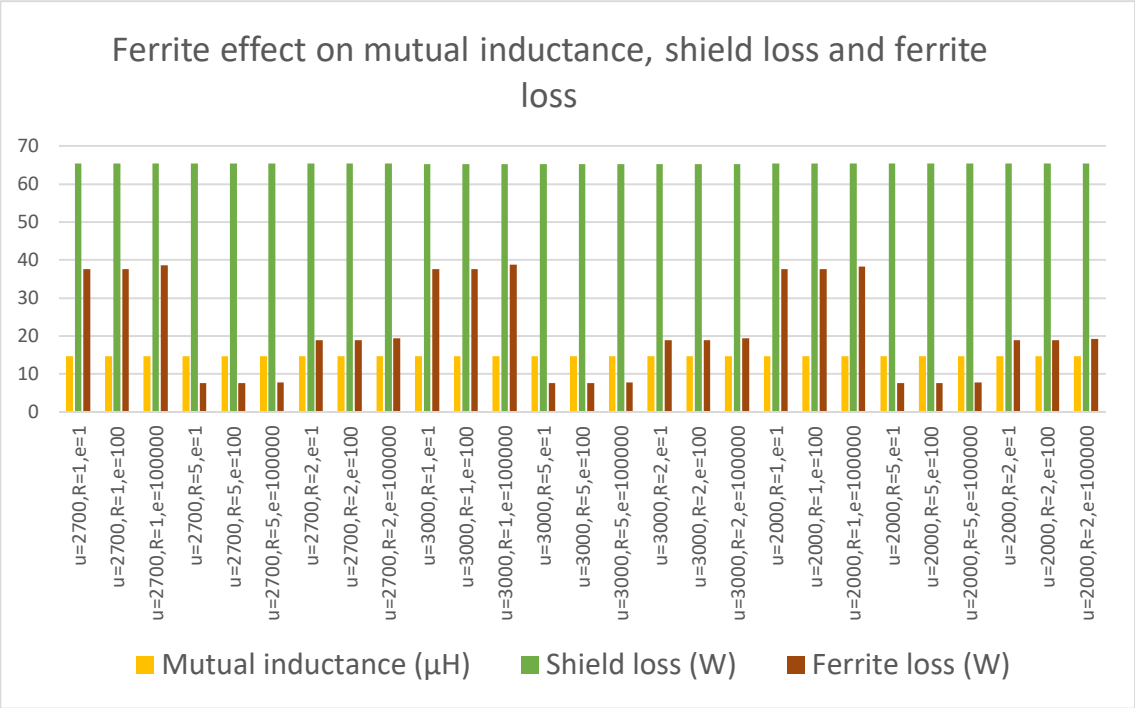

Figure 18. The effect of different material property combinations on mutual inductance, shield losses, and ferrite core losses. Ferrite material has no to minimal effect on mutual inductance and shield loss. However, it has a high effect on ferrite loss as one might expect. The average ferrite loss of all combinations was 21.472 W.

As Figure 18 shows, ferrite material does not affect much the mutual inductance and the shield loss. To be more precise, average mutual inductance was 14.581 µH with a standard deviation (STD) of 0.0096 µH and average shield loss was 65.254 W with an STD of 0.032 W. Furthermore, average ferrite loss was 21.472 W with an STD of 12.49 W. Therefore, the most suitable ferrite material can be found by looking at the ferrite losses. Hence the next figure, Figure 19, shows the relative ferrite loss of each material combination compared to the average loss.

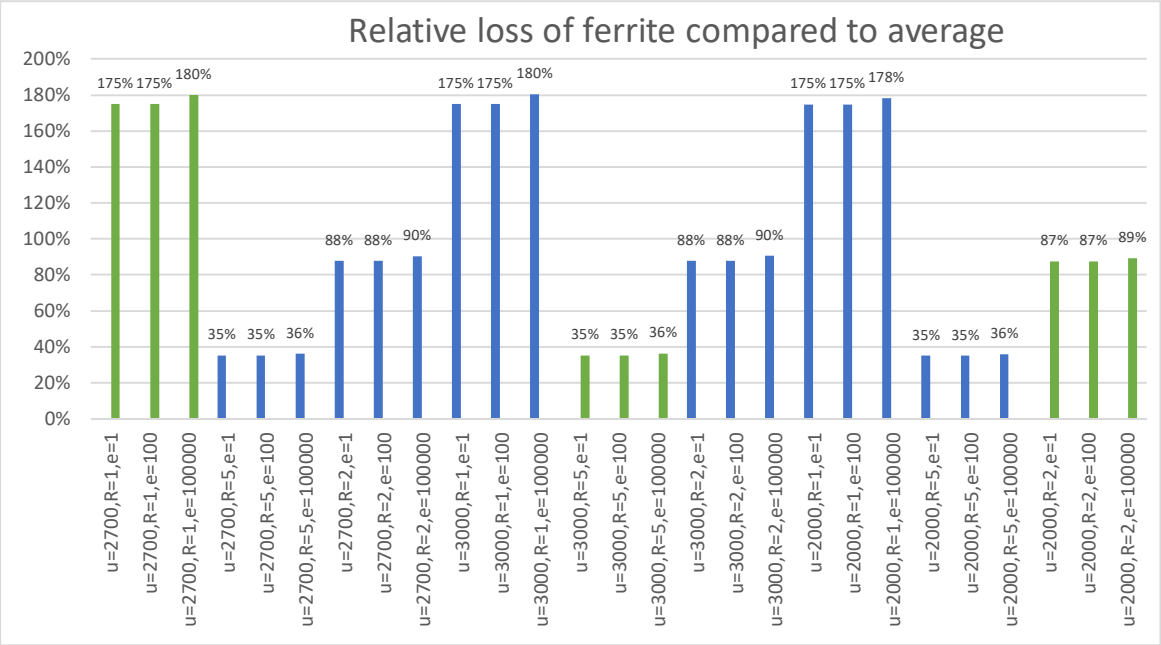

Figure 19. The relative loss in ferrite cores for all material property combinations rounded to the nearest integer. Resistivity has the most significant effect on the ferrite losses, and permittivity has a low affect, and permeability has practically zero effect. Green bars correspond to the 3C81, 3C95 and 3F3 ferrites with different permittivities. First three correspond 3C81, the ones in the middle correspond 3C95 and the left ones correspond 3F3. Blue bars represent the rest combinations which may or may not be existent materials. However, 3C95 causes as little loss as the two shortest blue groups. This means that 3C95 is quite an efficient core material for this charger, but it must be considered that this sensitivity analysis was quite narrow.

As Figure 19 shows, 3C95 can be considered the most efficient core material of the three materials. Moreover, 3C95 was also the most suitable according to the manufacturer's datasheets so it was selected for the core. Resistivity has the most significant effect on ferrite core losses; increasing electrical resistivity from 1 Ω m to 5 Ω m can drop the relative losses up to 144 %. Permittivity has the second-most effect but still only a maximum of 5 %. Lastly, permeability has the least effect on ferrite core losses, a maximum of 2 %. However, this study covers only a small range of possible ferrite properties and if a more extensive range is studied, the percentages may vary. The used range is still justified since it managed to find new material for ferrite core that is better than the original choice.
Moreover, this analysis showed how these numerical methods could be applied to a wireless charger and presented the principles of this kind of analysis. Next, the new ferrite assemblies are shortly presented, but, the main analysis is considered more in paragraph 3.3.

Four new ferrite assemblies were designed and compared to the original design. The comparison is based on mutual inductance, efficiency and mass. Typically EVs are designed to be lighter than ICE vehicles to increase the range and efficiency of an EV [4]. Moreover, in [4], it was found through simulations that change in the vehicle's battery mass is affecting the most to the EV's consumption, more than the change in coefficients of drag and rolling resistance or vehicle frontal area. Hence, emphasizing the importance of ferrite assembly analysis especially because the ferrite cores are mounted to the VA. The four new designs are named based on the appearance of the designs. Figures from Figure 20 to Figure 23 present the original design with the four new designs.

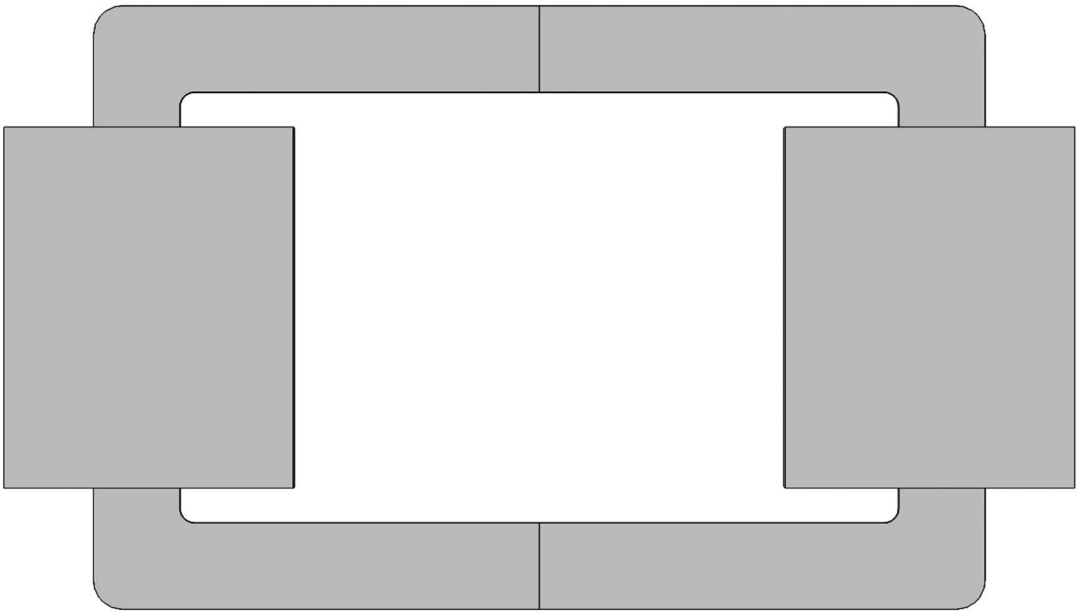

Figure 20. The Original ferrite assembly. This assembly was designed and optimized in [5] *which provides a good starting point for the analysis.*

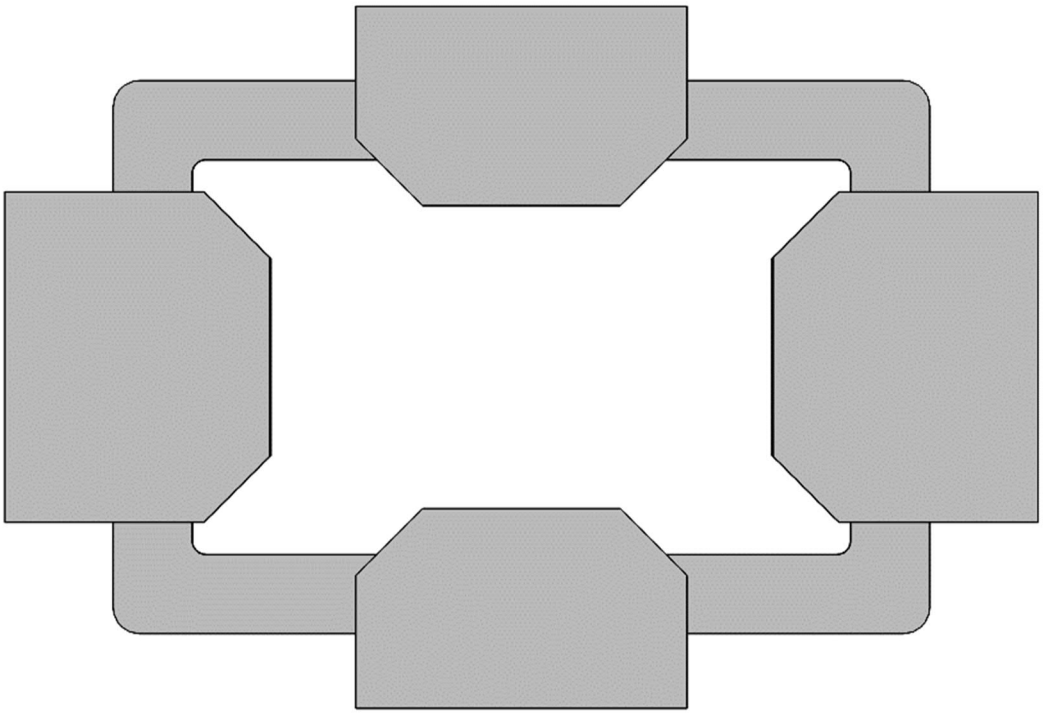

Figure 21. The Monolith ferrite assembly. This design is based on the Original design. Square corners inside the receiver were removed, and two more pieces of ferrite were added in the hope of getting higher mutual inductance. However, this makes the Monolith model heavier than the Original design.

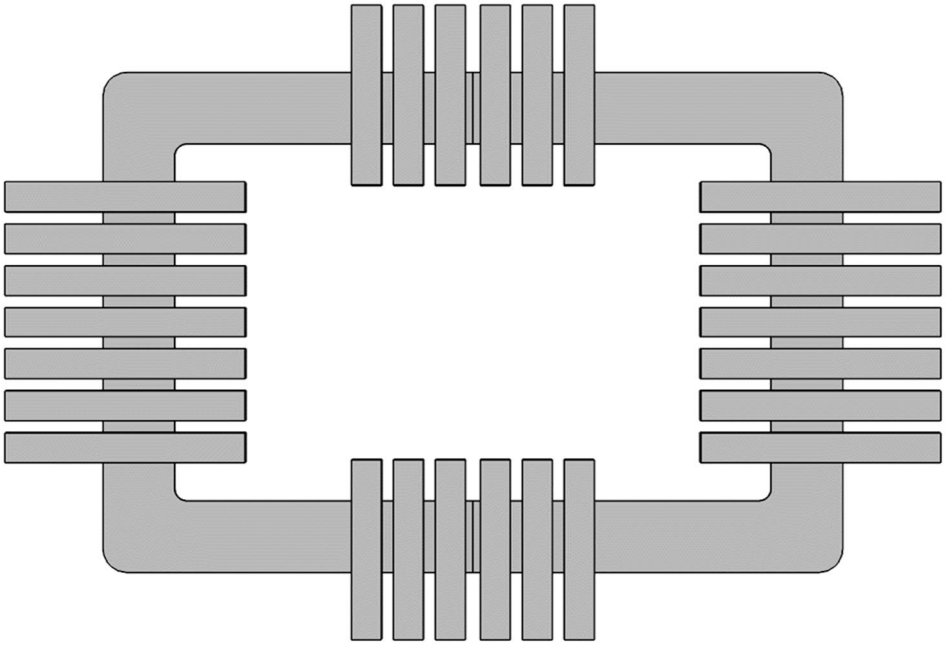

Figure 22. The Sticks ferrite assembly. This design is a light weighted version of the Monolith design. It was assumed to provide as high mutual inductance as the Monolith design but with less mass.

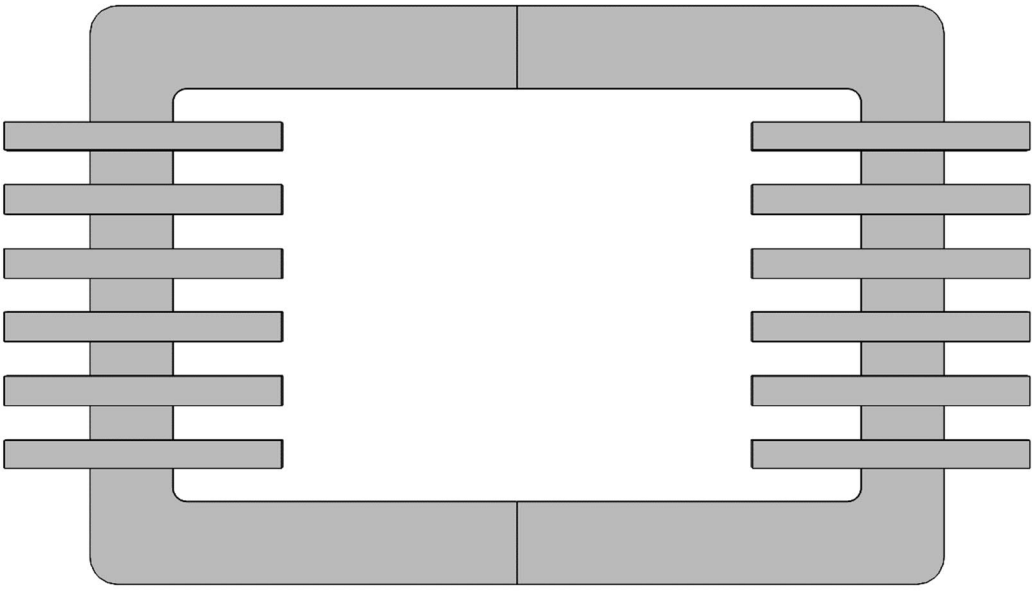

Figure 23. The Striped ferrite assembly. This model represents the light weighted version of the Original design. It was assumed that it would provide performance similar to the Original design but with less mass.

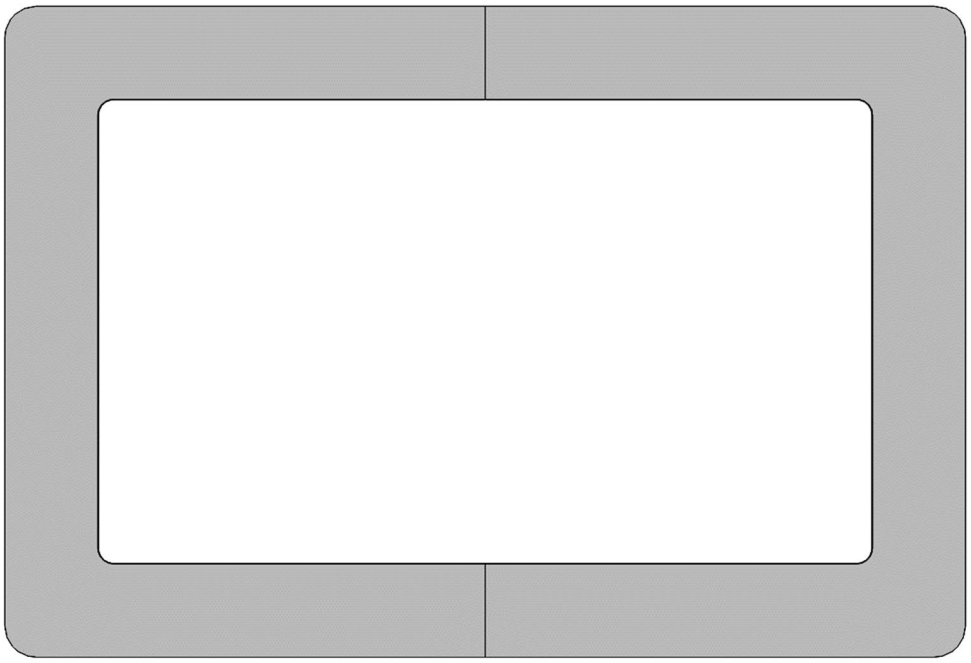

Figure 24. Lastly, there is the Empty ferrite assembly. This design was added to the study to see how much the ferrite increases the performance.

It was assumed that the Monolith and Sticks assemblies would increase the mutual inductance and also the mass of the charger's vehicle assembly (VA). On the contrary, Striped and Empty were assumed to decrease both the mutual inductance and mass of the VA. These assemblies are analyzed in chapter 3.3, and next, shield material is selected.

2.4.3 Selecting shield material

The shield is preventing the magnetic fields from going inside of the vehicle and it also contributes to the guiding of the magnetic fields as a ferrite core. In [5], two materials were proposed; 1100 aluminum and 304 stainless steel, and 1100 aluminum was preferred since "it can guarantee a lighter solution with a lower value of induced losses thanks to its high conductivity" [5]. In this thesis, a third material is added to the comparison; 1050 aluminum. 1050 aluminum was added for this comparison as it is one of the most corrosion-resistant of all aluminum alloys, and it is also used in the automobile industry [19] with a slightly higher electrical conductivity than 1100 aluminum. This is done in order to reveal the effect of shield conductivity in induced losses. Besides, the model is built to help these kinds of design problems.
The corrosion resistance of all these three materials will make the shield withstand against environmental especially against the salting of the roads during winters. Moreover, all these three materials have good formability in terms of metal cold and hot forming, metal press forming, metal deep forming and weldability [20], so all of them can be used to make complex-shaped shields. Lastly, the shield should also work as a heat sink for the charger [5]. As a consequence of these material properties, all three materials are suitable for the shield, and thereby the material parameters are analyzed to find the most efficient of them. Table 4 shows the material parameters of the selected three materials.

Table 9. Material properties for possible shield materials [21]. ** Average of tensile and compression ** tensile modulus. The compression modulus is about 2 % higher than the tensile modulus.*

Parameter	1100-H14 aluminum	304 stainless steel Annealed Sheet	1050-H14 aluminum	Unit
Electrical conductivity	33.45	1.39	34.48	MS/m
Relative permeability	1	1.02	1	N/A
Thermal conductivity	222	16.5	227	W/(mK)
Heat capacity	904	500	900	J/(kgK)
Modulus of elasticity	68.9*	193	69**	GPa
Density	2710	8000	2705	kg/m^3

As Table 4 shows, 1050 aluminum has the highest electrical and thermal conductivity combined with the lowest density. Moreover, 304 stainless steel has the highest density and lowest conductivities which hints that it has the highest induced losses combined with low heat dissipation and heavy structure compared to aluminum. Hence, 304 stainless steel is not considered and the model is now used to evaluate induced losses for the two aluminum grades.

Induced losses in the shield can be estimated with impedance boundary condition (IBC) or by solving the electromagnetic field in the shield domain. IBC assumes that there is no electromagnetic field inside of a domain, and it prevents the domain from being meshed [22]. Consequently making it particularly useful for domains with small skin depth. If the IBC is used, induced losses are calculated as integral over the shield surface area. COMSOL provides built-in "Surface loss density, electromagnetic" (mf.Qsh) variable for the integration:

$$P_{loss} = \int_{S_{shield}} \text{mf.Qsh}\, ds\,. \tag{14}$$

The losses can also be evaluated based on current density and electric field, as in the ferrite case. The general formula for losses is

$$P_{loss} = \frac{1}{2}\delta \int_{S_{shield}} \vec{J} \cdot \vec{E}^{*}\, ds\,, \tag{15}$$

where δ denotes skin depth [9]. Furthermore, COMSOL provides surface current density variable $\vec{J}_{surf}$ which allows the losses to be calculated without skin depth as follows,

$$P_{loss} = \frac{1}{2} \int_{S_{shield}} \vec{J}_{surf} \cdot \vec{E}^{*} \, ds \, . \tag{16}$$

The other way of simulating a shield is not to use the SIBC. Then the shield losses can be evaluated the same way as for ferrite. However, the shield geometry is rather complicated for efficient meshing as it has large dimensions combined with tiny ones. This causes false results if the mesh too coarse. For example, if any of the meshed presented in chapter 2.4.1 is used with ferrite style volume integration without IBC, shield losses are about 0.02 W whereas with IBC they are around 65 W. This is due to the small skin depth of aluminum which would require a proper boundary layer mesh (Figure 25). The four meshes described in chapter 2.4.1 do not produce enough dense mesh near the boundaries of the shield so it is more comfortable to use IBC and equation (14). Besides, IBC decreases the computation time as well.

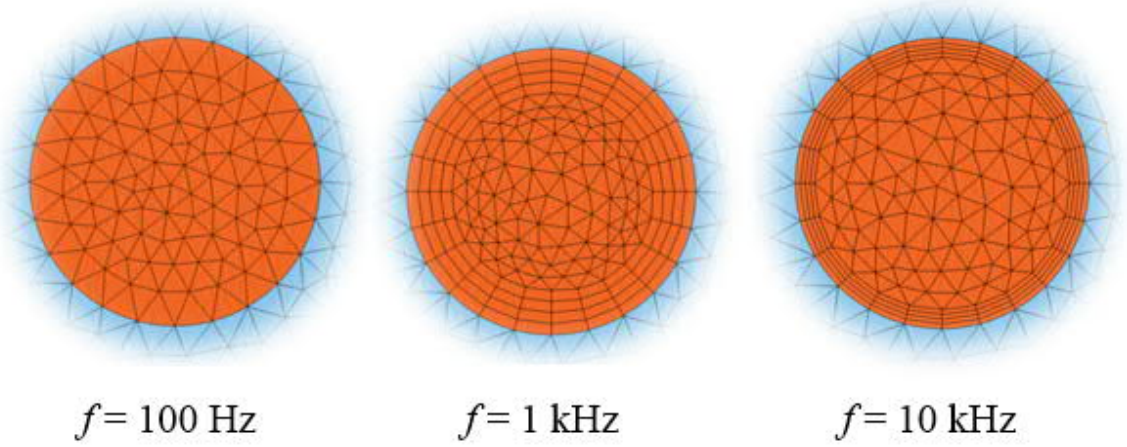

Figure 25. When excitation frequency is increased from 100 Hz to 10 kHz, the skin depth of a conductor decreases, which requires more dense mesh near the edge of the conductor. When skin depth becomes very small, it is more efficient to use IBC as it assumes no electromagnetic field inside of a domain and forces all fields at the surface.[22]

The final decision is made according to the materials' performance in five categories: induced losses, mutual inductance, thermal conductivity, modulus of elasticity and density. The following Table 10 compares the two aluminum grades in these five categories.

*Table 10. Comparison between aluminum grades 1100-H14 and 1050-H14. Cells with better values are highlighted with green. 1050-H14 is a better choice in four of the five categories while it is a draw in one category. * Average of tensile and compression ** tensile, compression modulus is about 2 % higher than the tensile modulus.*

Parameter	1100-H14 aluminum	1050-H14 aluminum	Unit
Induced losses	66.184	65.220	W
Mutual inductance	14.661	14.661	µH
Thermal conductivity [21]	222	227	W/(mK)

Modulus of Elasticity [21]	68.9*	69**	J/(kgK)
Density [21]	2710	2705	kg/m3
Total score	1	5	

As Table 10 shows, the 1050-H14 performs slightly better than 1100-H14 in four of the five categories. Although the difference between these aluminum grades is tight and both grades could be considered, 1050-H14 was still selected. Moreover, there can be even better materials than 1050-H14 aluminum, but the comprehensive material assessment is out of the scope of this thesis, and only the basic idea of material selection using the model is introduced in this thesis. Furthermore, the same principles suit also for more comprehensive material selection. Table 11 shows an overview of the selection principles. However, deciding the correct weight for each property remain to the engineer.

Table 11. The basic principles for selecting shield material.

Material property	Reason
Maximize	
Electrical conductivity	Decreases induced losses
Thermal conductivity	Improves cooling
Elastic modulus	Enables lighter structure
Modulus of elasticity	Enables stiff and light structure
Minimize	
Density	Decrease the weight
Material price	Decreases shield price
Things to consider	
Galvanic corrosion	Wrong material pairs can lead to rapid corrosion
Formability	Affects manufacturing costs and possible shapes
Durability	Increases lifetime

2.4.4 Skin and proximity effects

Two phenomena characterize the flow of AC-current in conductors. These phenomena are called skin and proximity effects, and they play a significant role in high-frequency applications. Both effects are increasing the resistance of a conductor with slightly different mechanisms. A rough division can be made; skin effect happens inside of a conductor whereas proximity effect happens between two conductors. Next, both phenomena are described briefly, and then the real-life solution for these problems and modeling aspects are considered.

Proximity effect happens with two or more conductors lying parallel to another. When current flows in a conductor, it produces a circular magnetic field around the conductor. That magnetic field is affecting other conductors, which makes the conductors interfere with each other through eddy currents. The conductors are then producing longitudinal eddy-currents to other conductors which will pack the current in the conductors to opposite or adjacent borders depending on the current direction. Thus, the current is crowded into a smaller cross-section which increases the resistance similar to the skin effect.

Skin depth describes the depth at which the AC-current flows, and one can be assumed that all current flows above the skin depth and no current flows deeper than the skin depth. The skin effect happens in conductors when excitation frequency is high and when the conductor has high conductivity and permeability. The skin effect means that almost all current flows near the conductor surface by distributing the current density unevenly. Unlike DC-current, AC-current packs at the surfaces of the conductor depending on the excitation current and therefore the AC-resistance of the conductor is higher than DC-resistance. It can be thought through a parable; skin effect decreases the suitable cross-section of a conductor making it harder the current to pass. Moreover, a hollow conductor is more efficient than a solid conductor for AC-current as the not utilized part is removed. Skin depth can be calculated with the following formula

$$\delta = \sqrt{\frac{2\rho}{\omega\mu}}\sqrt{\sqrt{1+(\rho\omega\varepsilon)^2}+\rho\omega\varepsilon} \approx \sqrt{\frac{2\rho}{\omega\mu}} for, \omega \ll \frac{2\pi}{\rho\varepsilon}, \quad (17)$$

where ρ, μ and ε are referred to as electrical resistivity, permeability, and permittivity. Next, the skin depths are presented in Table 12.

Table 12. Different skin depths and material properties for modeled parts and materials.

Part	Electrical resistivity (Ωm)	Relative permeability	Relative permittivity	Skin depth (mm)
Ferrite core 3C95 [16]	5	3000	100000	156.5
Aluminum shield [21]	$2.9\ 10^{-8}$	1	1	0.294
Copper coil [23]	$5.8\ 10^{7}$	1	1	0.227

As Table 12 showed, ferrite has much higher skin depth than aluminum and copper, and ferrite is then possible to simulate efficiently with linear mesh. Aluminum shield, on the other hand, needs IBC or boundary layer mesh, as described in chapter 2.4.3. In spite that copper has approximately the same skin depth as aluminum, it is modeled differently as it forms the two coils of the charger.
In real-life applications, a litz-wire is used for conductors with high frequency to overcome the skin and proximity effects. A litz-wire consists of multiple tiny wires that are covered with an insulating layer. Furthermore, these tiny wires are then twisted or braided in such a way that they form a criss-cross pattern where the tiny wires are sometimes at the center of the bundle and sometimes on the surfaces. This braiding technique wakens the skin and proximity effects, thus increasing efficiency. Furthermore, the charger uses a litz-wire with 2050 individual (thickness of one strand is 0.1 mm) enameled strands in five groups.

Figure 26. An example of a litz-wire with enameled strands in five groups.[24]

To truly simulate this kind of wire, one must model every 2050 tiny strands. However, this is practically impossible, and thus simplifications are needed. As Figure 26 showed, the litz-wire overcomes the skin and proximity effects and homogenizes the AC-current in the whole wire. This feature is the key to simulating litz-wire as it offers the advantage of using evenly distributed current density in the wire which is available in COMSOL. Now, when the model is fully specified, it is possible to move to the TDM.

2.5 TDM validation

As described in 2.2, the original model provided by Cirimele was validated through real-life measurements. Therefore, it can be assumed that the new slightly modified FDM version of that can also be trusted, and it can be used as a reference for the TDM.
The creation of TDM was quite straightforward; the solver type was changed from frequency-domain solver to time-dependent solver. Moreover, the excitation currents were applied using wave functions and movement was added using moving mesh functionality. The most significant difference between the FDM and the TDM is that the FDM gives only one solution for one frequency, whereas the TDM model gives a solution for each time-step. The TDM was verified using the measurement lines described in chapter 2.3. Magnetic flux densities were evaluated on these measurement lines and that analysis proofs that the TDM

matches the FDM. As seen in the following comparison (Figure 27, Figure 29, Figure 28 and Figure 30).

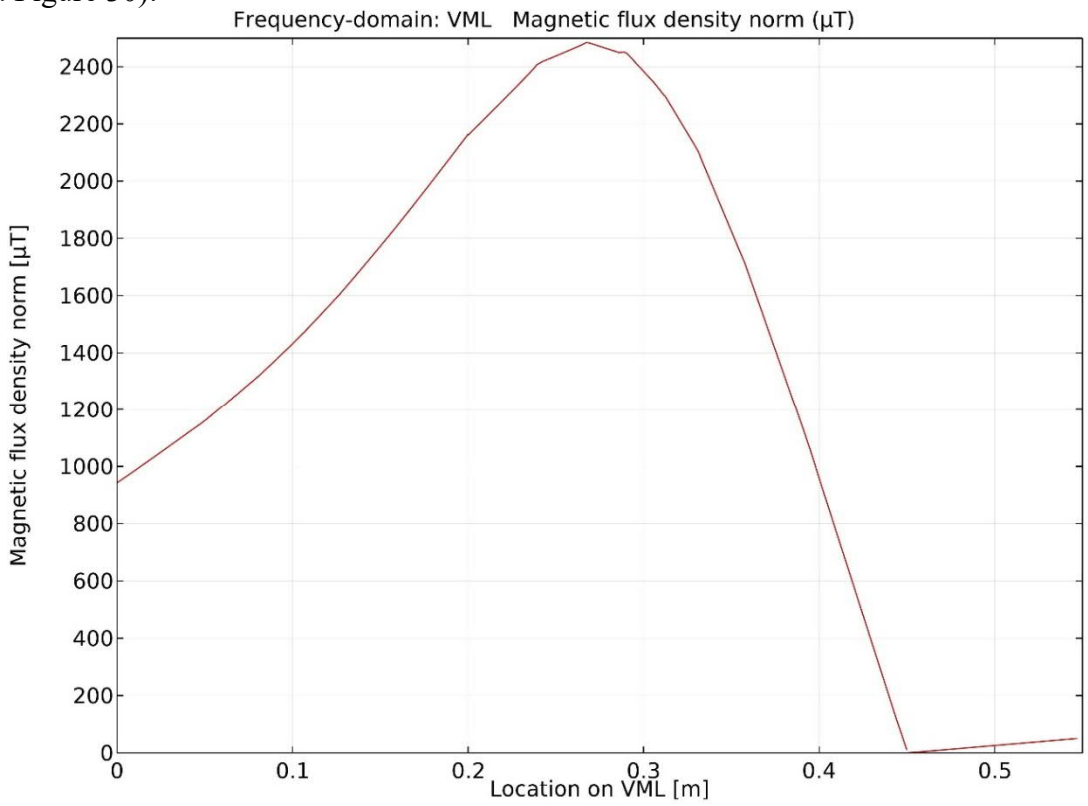

Figure 27. Magnetic flux density on VML with FDM.

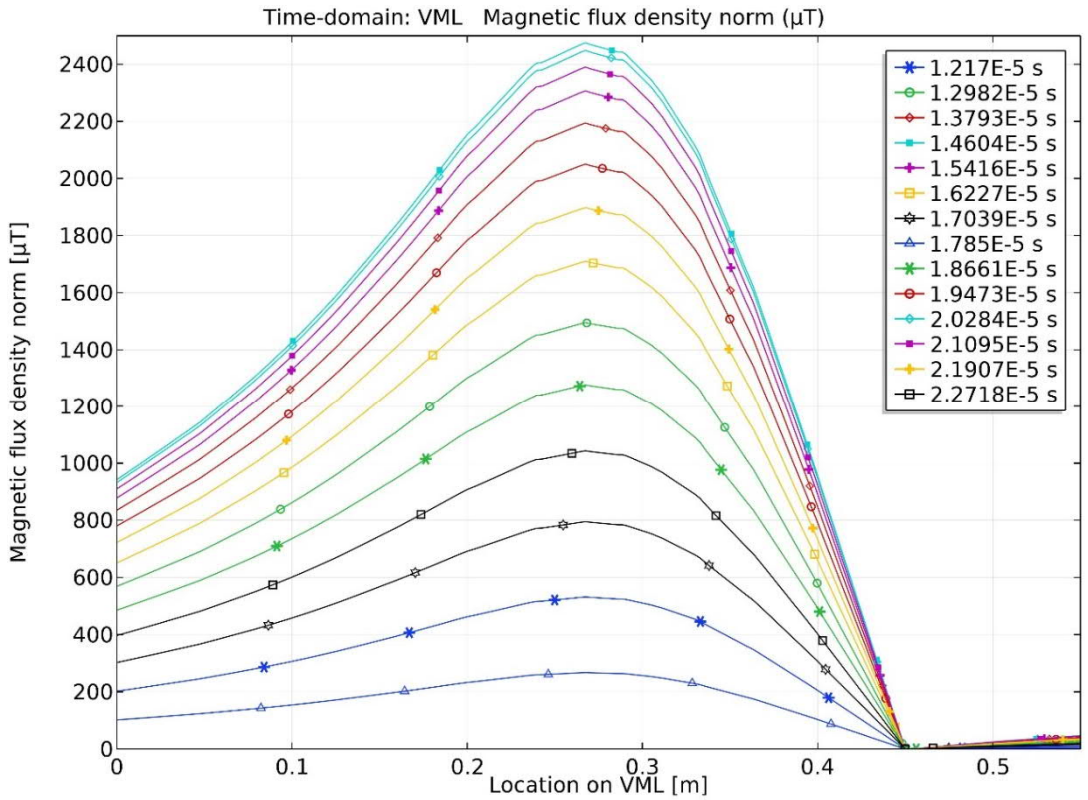

Figure 28. Magnetic flux density on VML with TDM. Highest lines matches with the FDM.

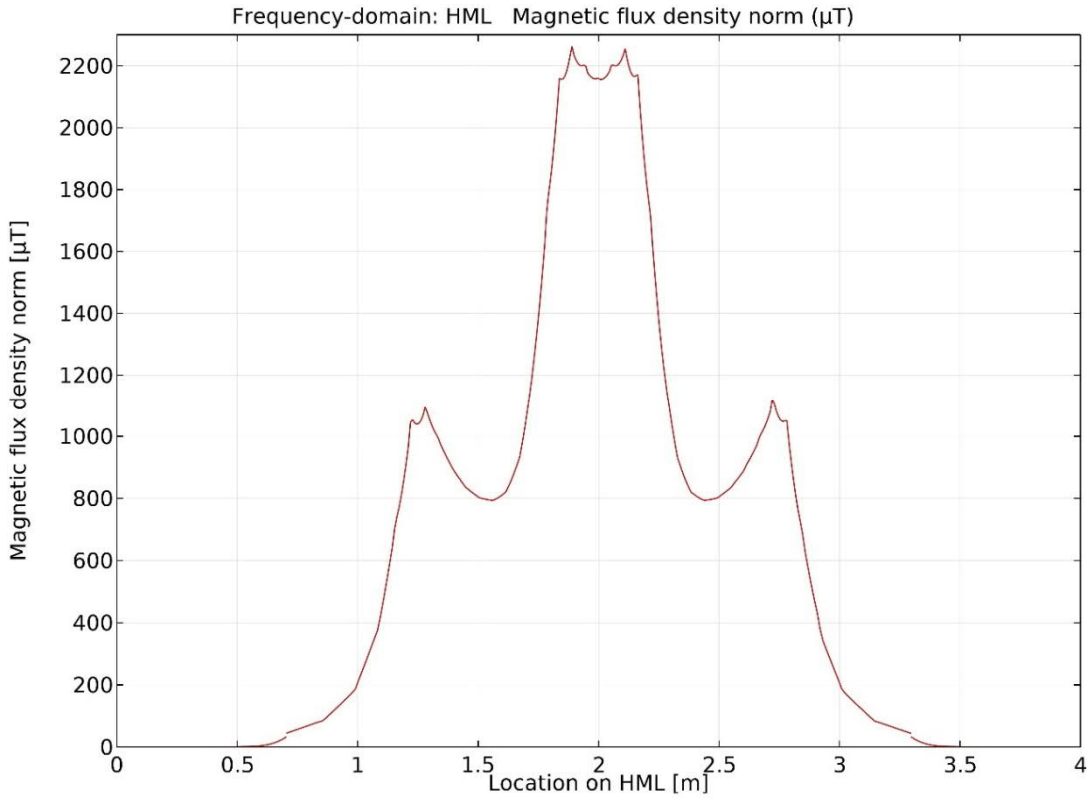

Figure 29. Magnetic flux density on HML with FDM.

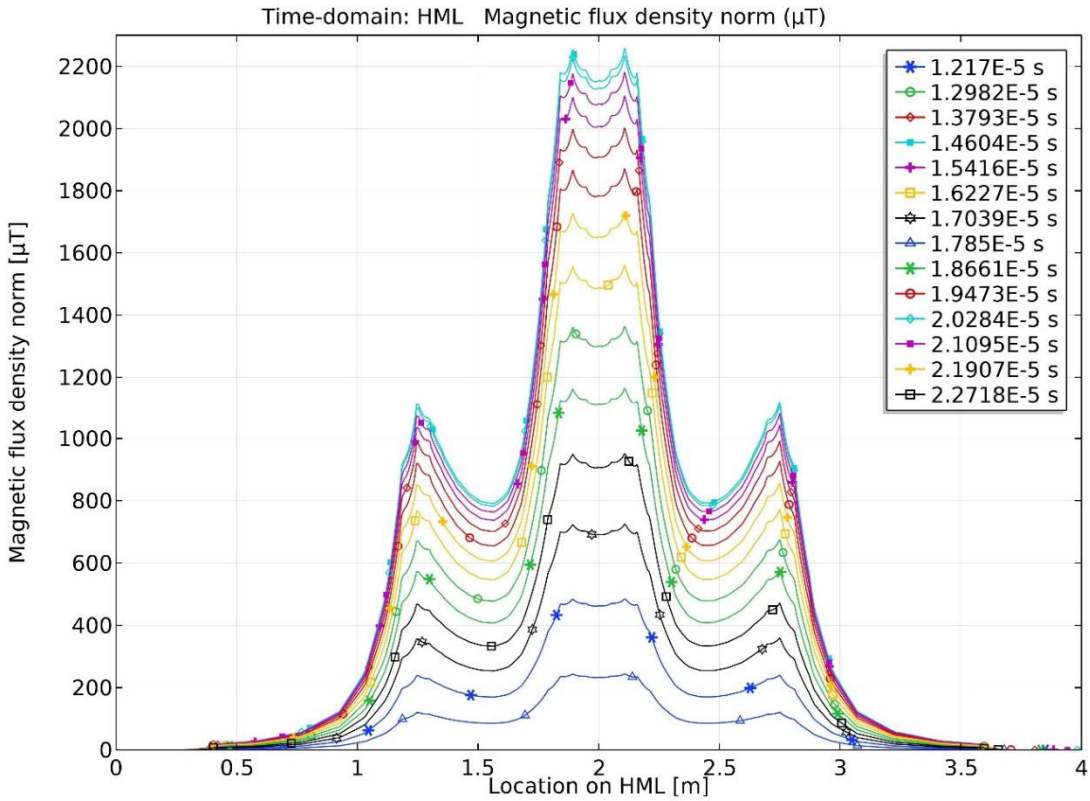

Figure 30. Magnetic flux density on HML with TDM. Highest lines matches with the FDM.

As the previous comparison graphs showed, the FDM model has produced a single graph, while TDM has produced a graph for each time step. However, the highest graphs of the TDM with VML and HML matches the values of FDM. Hence, it can be deduced that these models describe the same thing. Moreover, the mutual inductance between these models was also studied (Figure 31).

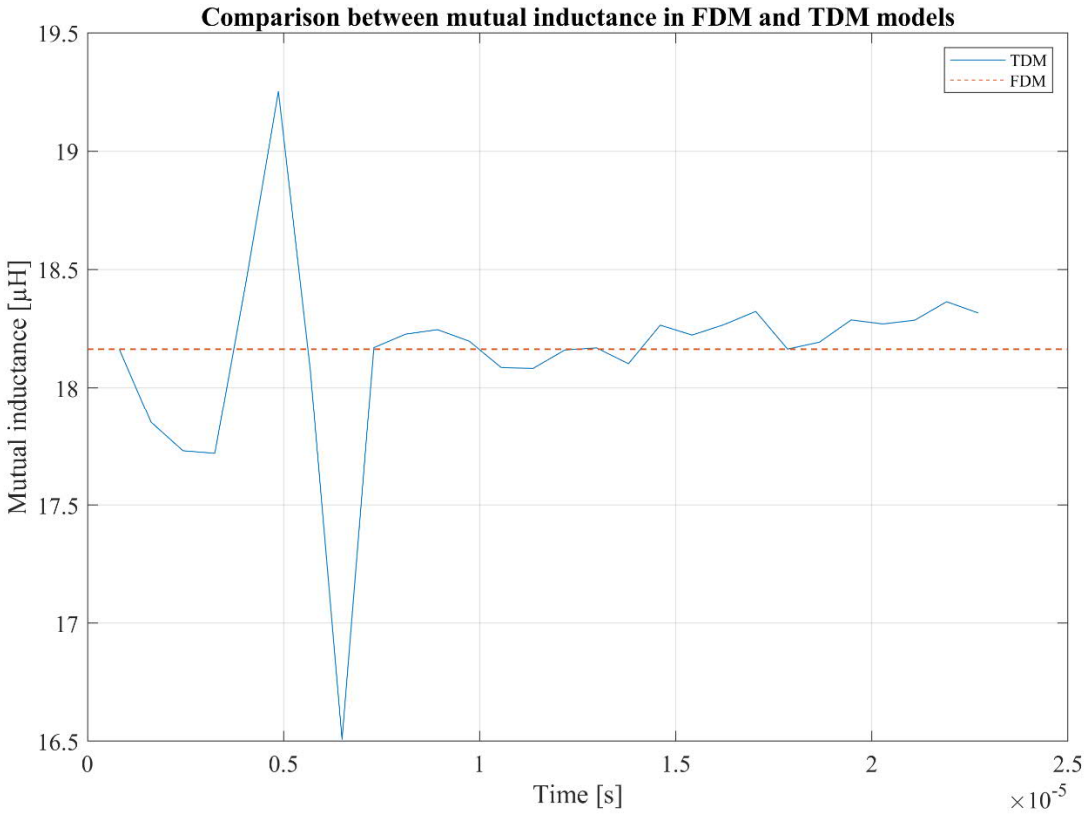

Figure 31. Mutual inductance comparison. Blue line represents mutual inductance in TDM and red dotted line in FDM. At the beginning of the simulation, the TDM differs much from FDM but, the graph shows that the mutual inductance in TDM converges to the same values as in FDM. The little error is probably caused by numerical error as TDM outputs only at some time-steps.

As a result of matching mutual inductances and matching magnetic flux densities, the TDM model can be considered correct. Furthermore, the TDM model can then be used for simulating dynamic wireless charging. Next, in the following chapter, the performance of the charger is analyzed. Then the vehicle speed is considered and lastly, different ferrite assemblies are analyzed.

3 Results

3.1 Performance analysis

As described in 2.3, the performance was analyzed in two phases. First, the parametric FDM is simulated with the nominal transmitter and receiver currents in order to acquire mutual inductances for different misalignments (Table 1 shows the nominal values provided by Cirimele). This initial simulation reveals mutual inductances which are used for transmitter current tuning. Furthermore, the transmitter current is tuned for each of the five air gaps and misalignments in order to maintain the same nominal maximum power of 20 kW for all positions.

3.1.1 Mutual inductance maps

Misalignment between coils in X, Y and Z directions has an effect on mutual inductance between the coils. Air gap (magnetic gap) is computed with 5 cm, 10 cm, 15 cm, 20 cm and 25 cm distances covering all three Z-classes in [SAE TIR J2954]. Vehicle misalignment in Y-direction (vehicle driving direction DR) was ±1.2 m with 10 cm steps, and in X-direction (sideways direction SD) was ±1.0 m with 10 cm steps. The symmetry of the charger was exploited by simulating only from 0 m to 1.2 m for DR, and from 0 m 1m for SD, and thus, this misalignment analysis includes 11x13x5 715 data points (Figure 32).

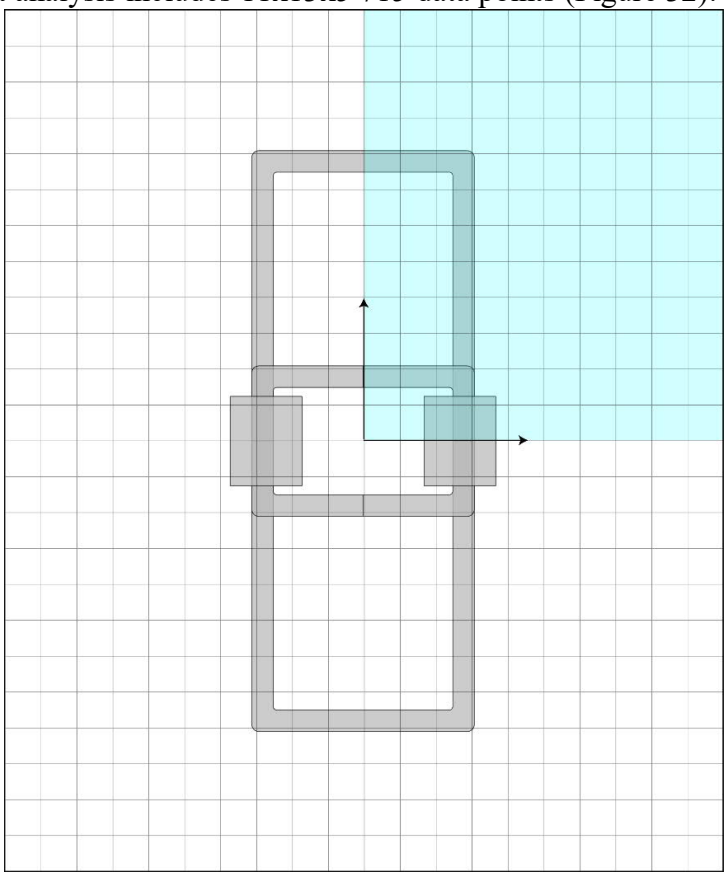

Figure 32. Illustration of the misalignment analysis. Transferring unit is stationary while the receiving unit was misplaced. The origin of the receiving unit is at the center of the receiver coil and the grid shows all of the points where the receiving unit was moved. Since the charger is symmetrical in both the driving and the sideway directions, only one quadrant of this grid needs to be analyzed and the rest of the data is acquired by mirroring the one quadrant. The cyan rectangle represents this one quadrant.

Then a 3D matrix was then created in MATLAB, including the mirrored data points for all air gap totaling a matrix of 21 by 25 by 5 with 2625 data points (individual solutions). This 3D data matrix made the plotting of the data very easy. Next, the following figures show the mutual inductances for all five air gaps under study, mutual inductance is illustrated in 2D (Figure 33 to Figure 37) and in 3D charts (Figure 38 to Figure 42). In the figures with 2D contour graphs, the thicker dashed lines are used to indicate two lines where the mutual inductance is at the border of ± 0 μH and at the border 20% of maximum mutual inductance. This high-performance line of 20% is located approximately ±70 cm within the vehicle center line in the DR and ±10 cm from the centerline in SD. In both 2D and 3D figures, the plotted values are absolute values meaning that actually, the values have different signs inside and outside of the border of ± 0 μH.

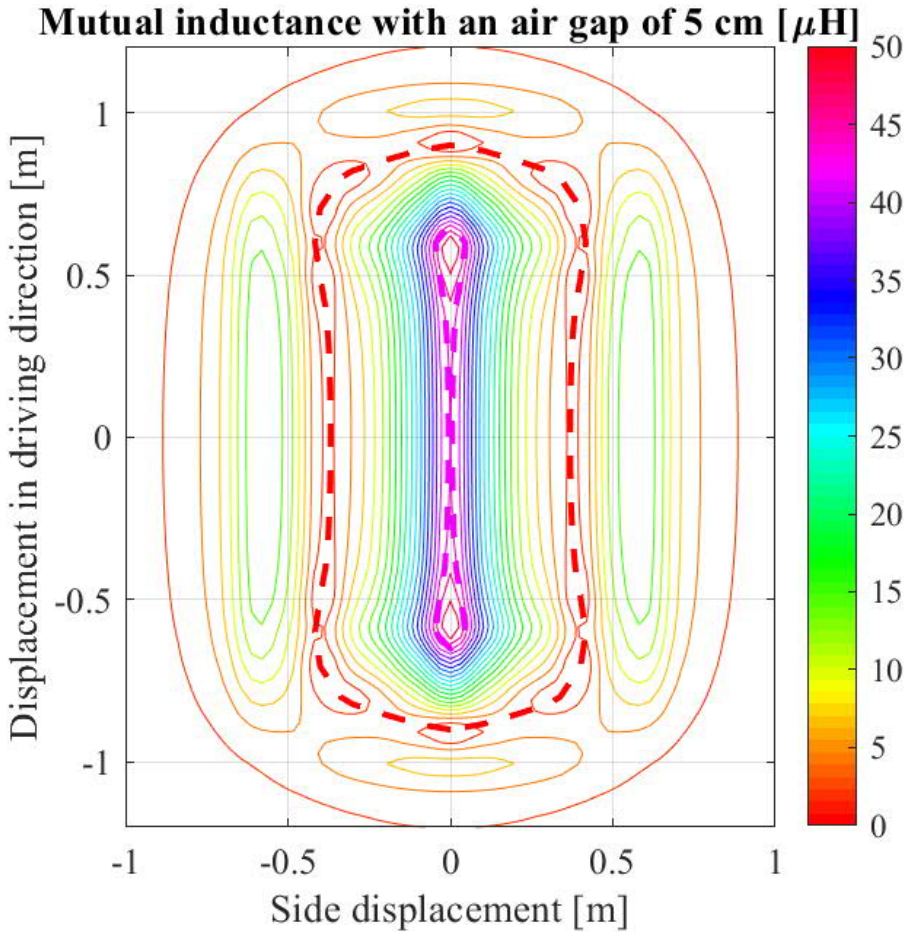

Figure 33. Mutual inductance with a magnetic gap of 5 cm. Thick dashed lines indicate the border of ±0 μH and the top 20% of maximum mutual inductance.

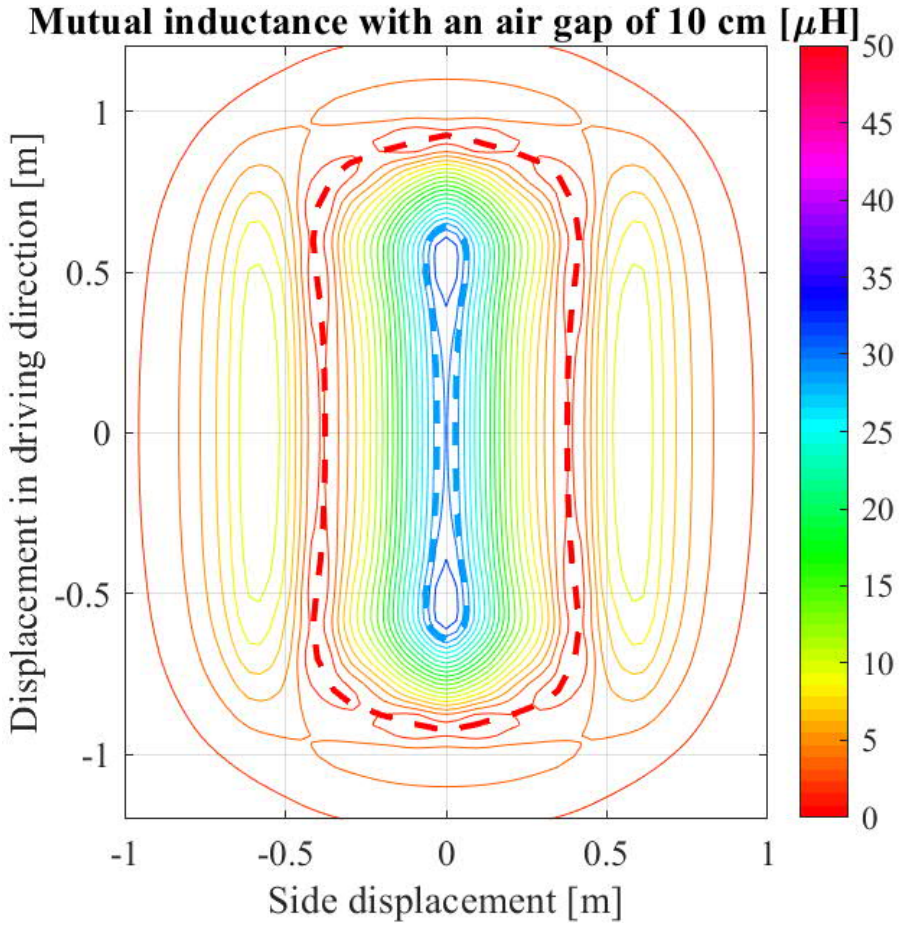

Figure 34. Mutual inductance with a magnetic gap of 10 cm. Thick dashed lines indicate the border of ±0 μH and the top 20% of maximum mutual inductance.

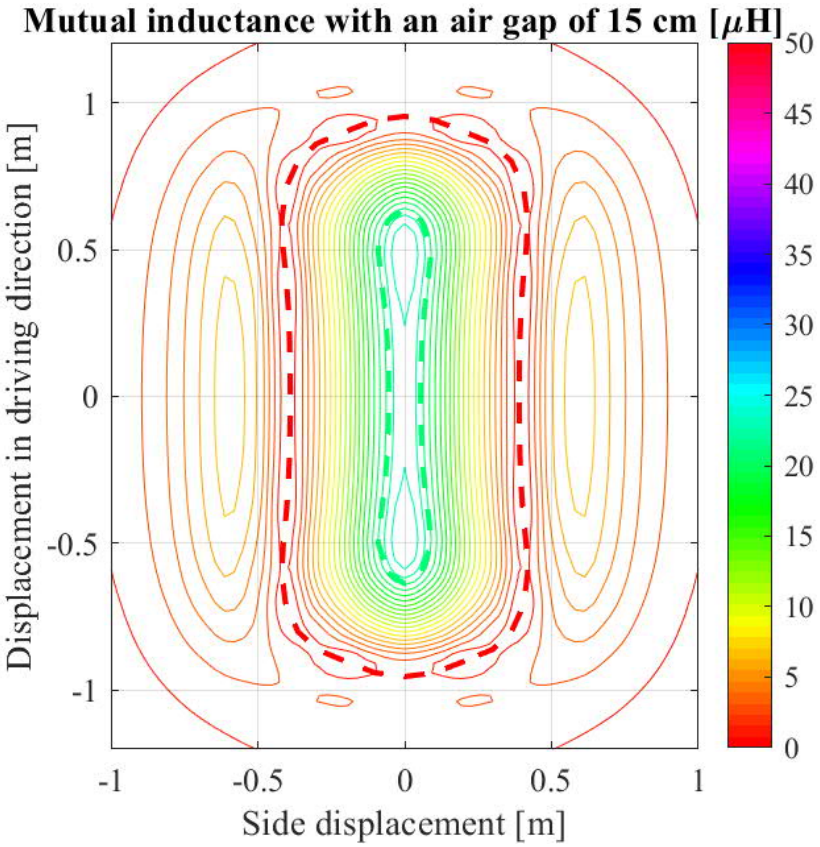

Figure 35. Mutual inductance with a magnetic gap of 15 cm. Thick dashed lines indicate the border of ±0 μH and the top 20% of maximum mutual inductance.

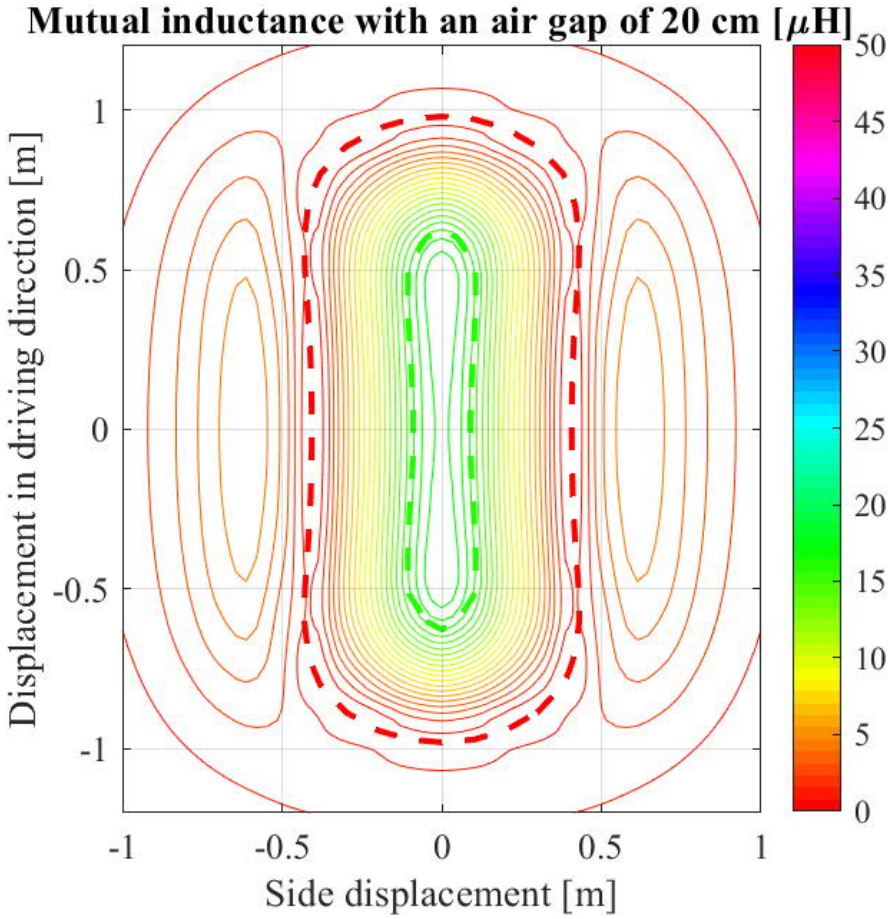

Figure 36. Mutual inductance with a magnetic gap of 20 cm. Thick dashed lines indicate the border of ±0 μH and the top 20% of maximum mutual inductance.

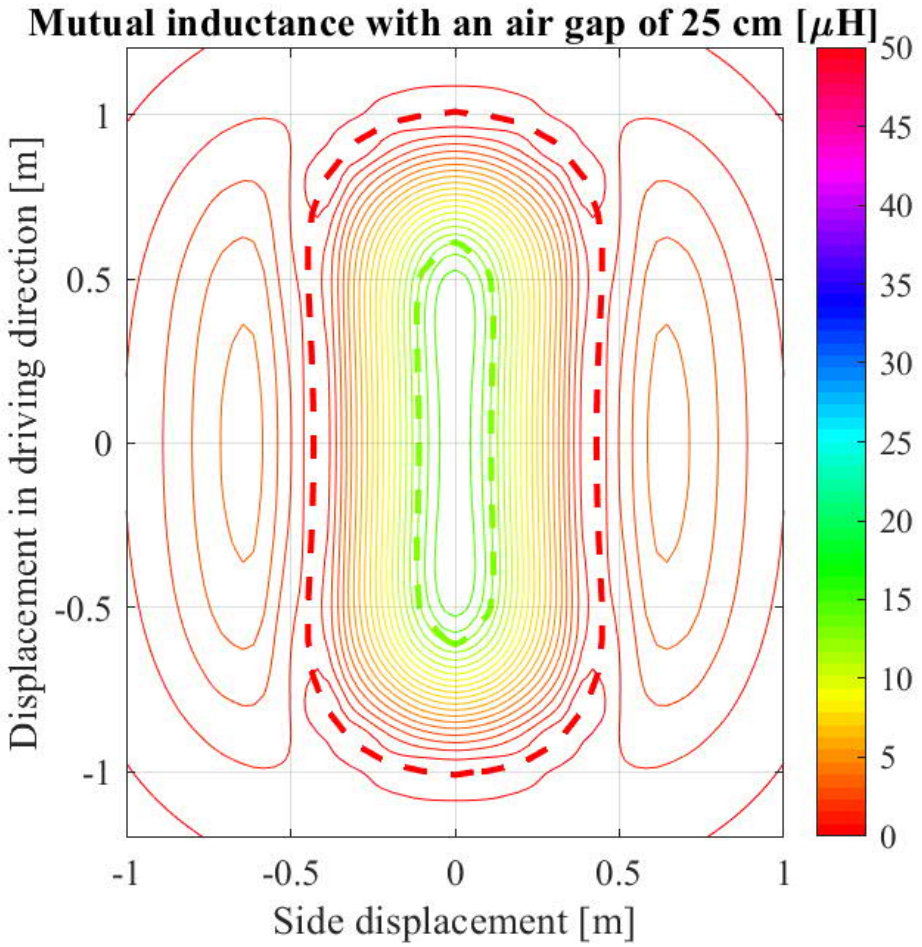

Figure 37. Mutual inductance with a magnetic gap of 25 cm. Thick dashed lines indicate the border of ±0 μH and the top 20% of maximum mutual inductance.

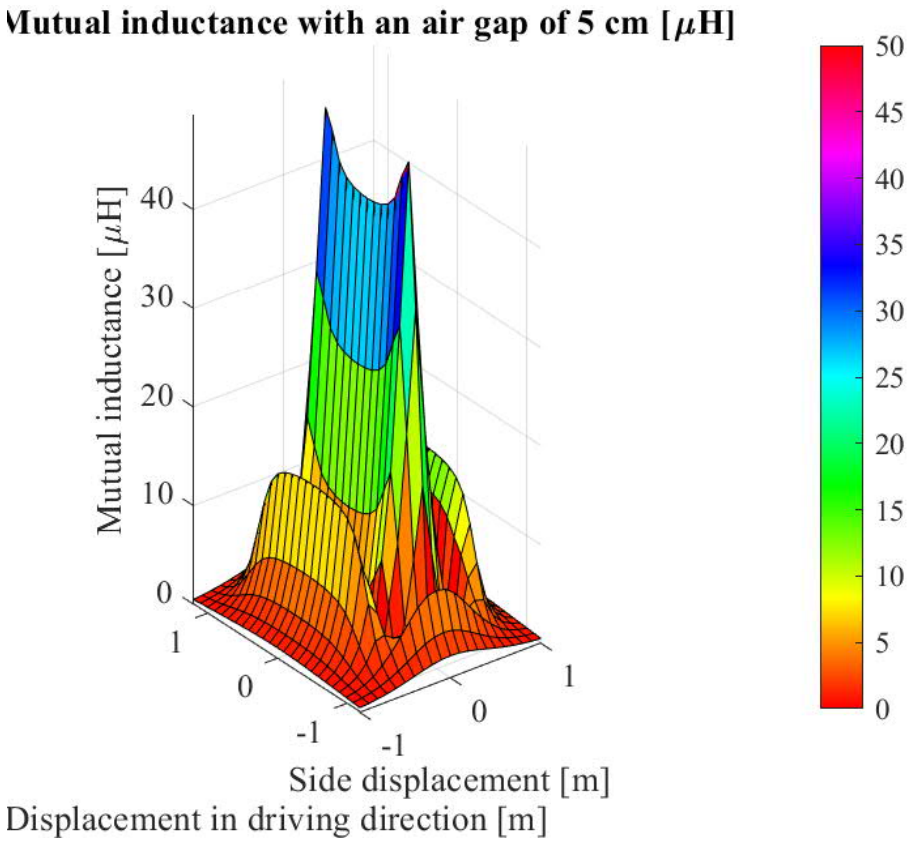

Figure 38. Mutual inductance with a magnetic gap of 5 cm. This is the smallest one of simulated air gaps, and it has the sharpest and highest map, which is prone to sideway misalignment.

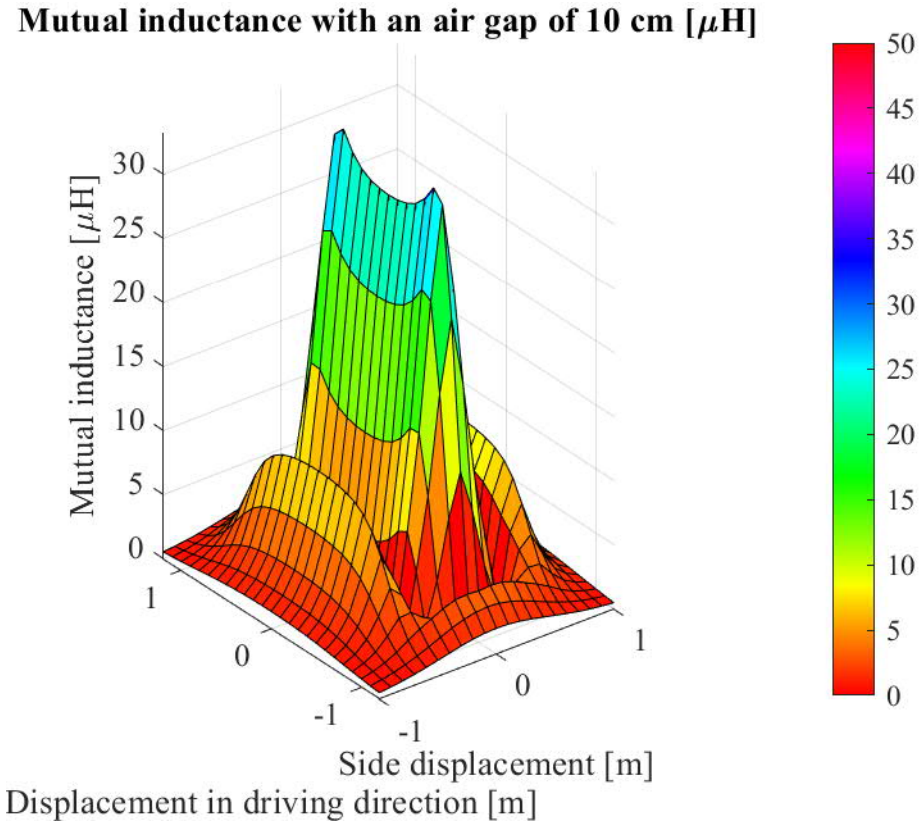

Figure 39. Mutual inductance with a magnetic gap of 10 cm.

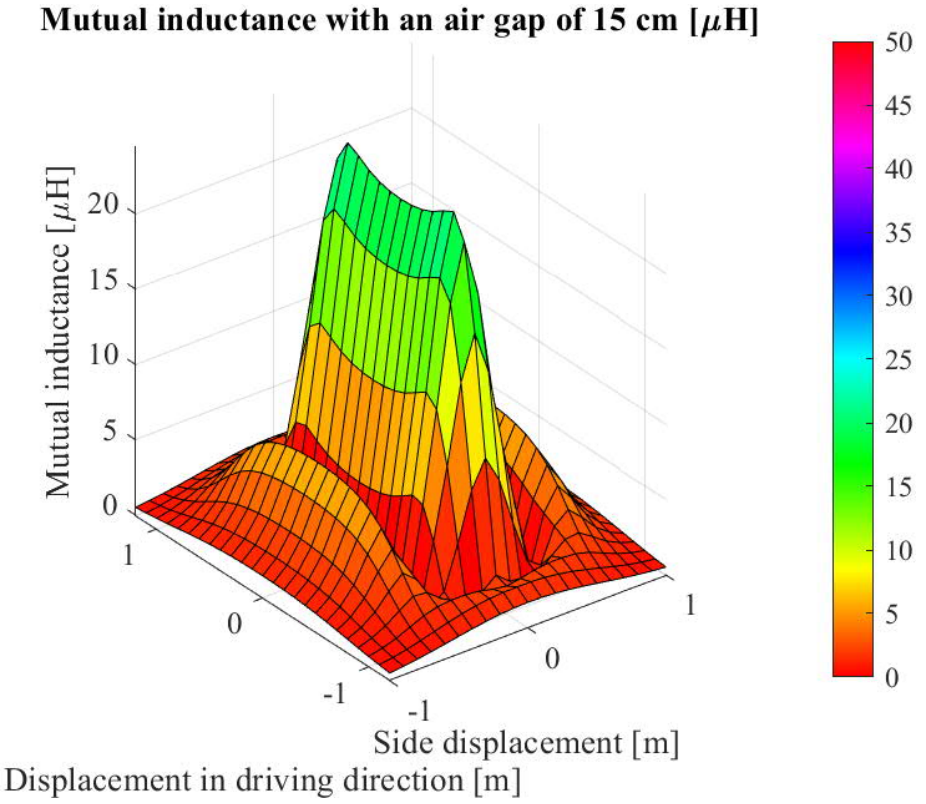

Figure 40. Mutual inductance with a magnetic gap of 15 cm.

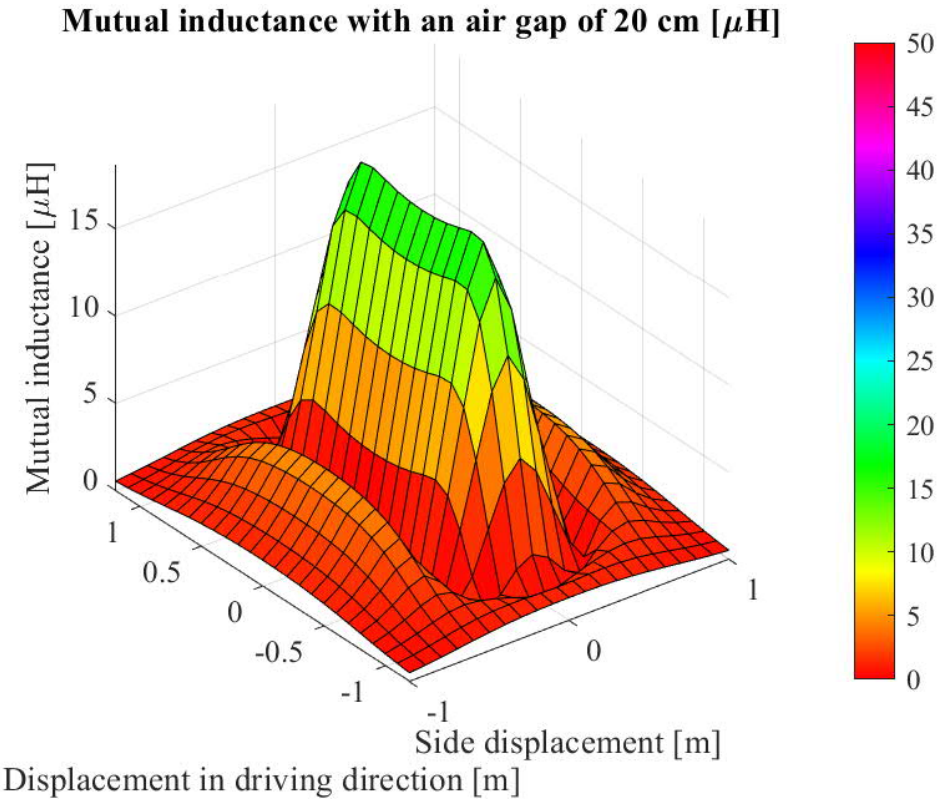

Figure 41. Mutual inductance with a magnetic gap of 20 cm.

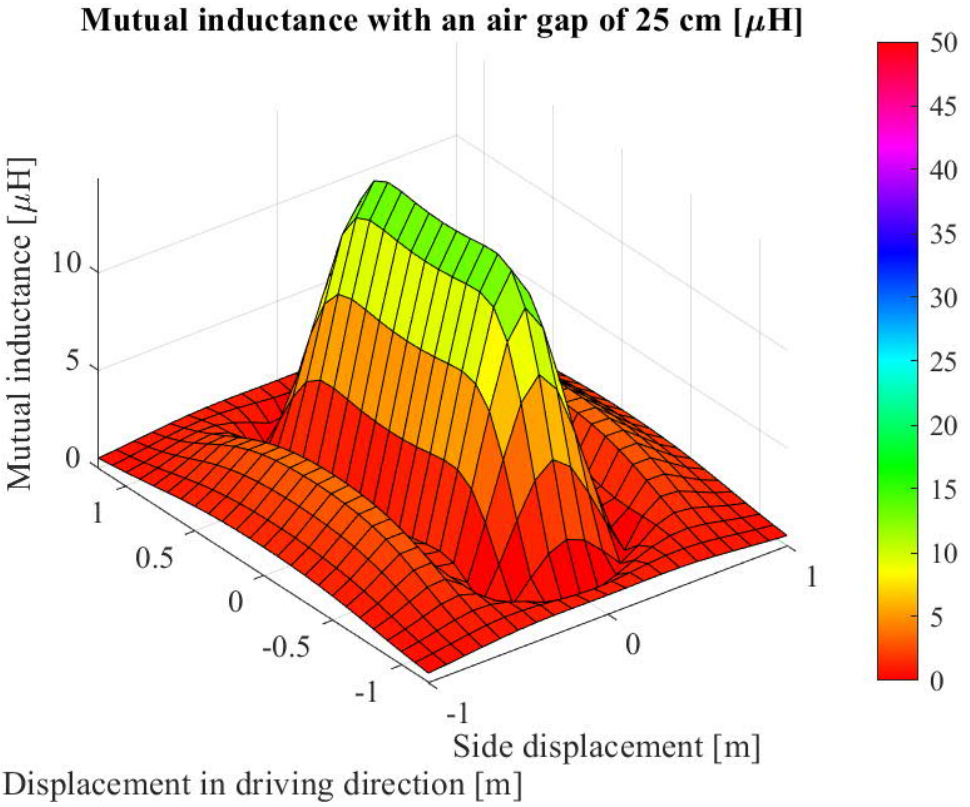

Figure 42. Mutual inductance with a magnetic gap of 25 cm. The largest air gap has the smoothest and shallowest map.

The previous figures presented the overall appearance of the mutual inductance of one air gap at the time. These images showed how the air gap is affecting mutual inductance. A small air gap is characterized by high mutual inductance with a very high gradient. Larger air gaps, on the other hand, produce smaller mutual inductances with a much smoother appearance. In addition, the mutual inductance was zero when the origin of the receiver coils was over the transmitter coil. This happens because then the magnetic field lines are parallel to receiver coil and no flux is going through the receiver coil. Based on the previous figures, an area within ± 0.6 m in DR and ± 0.1 m in SD is going to be used when average values are calculated because in that area the mutual inductance seems to have decent and steady values for all five air gaps (Figure 43). This area is called the measurement area (MA).

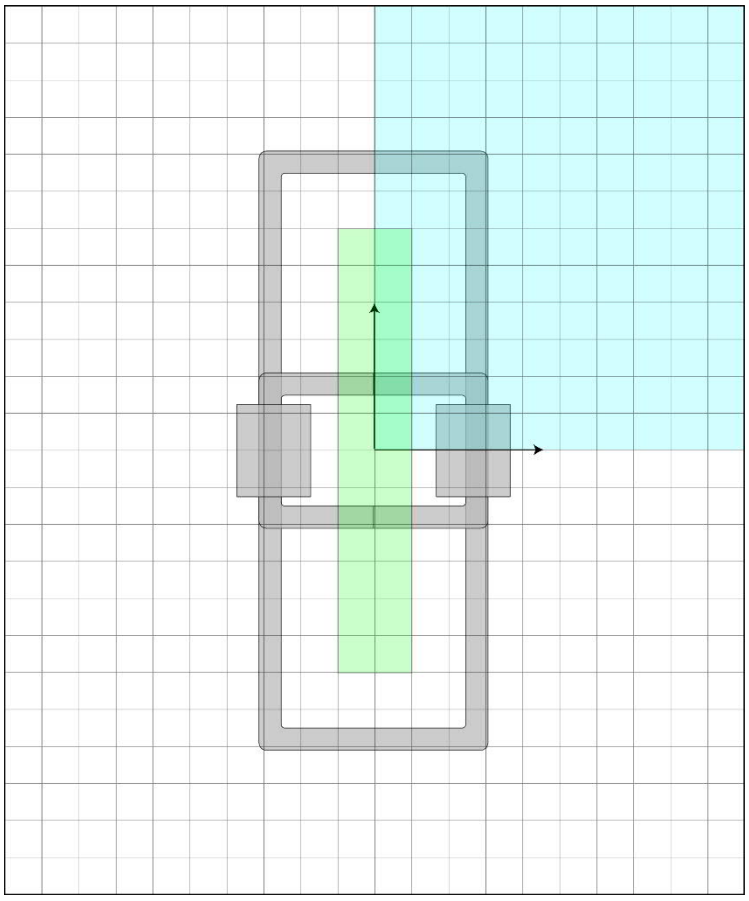

Figure 43. The light green area is called measurement area (MA) and it is decided to use when average values are calculated for mutual inductance and efficiency. The area was chosen because mutual inductances have decent and steady values. Moreover, it helps comparing the different air gaps when the measurement area is the same for all.

The following table, Table 13, shows the average mutual inductances for all five air gaps in the MA. It shows that the air gap is affecting exponentially to mutual inductance.

Table 13. Average mutual inductances in MA (misalignments ±0.6 in DR and ±0.1 in SD) for five air gaps.

Air gap [cm]	**Average mutual inductance [µH]**
5	34.77
10	26.86
15	21.09
20	16.80
25	13.56

Next, few tools for air gap comparison are presented in figures from Figure 44 to Figure 46. These figures show the effect of the air gap better than 2D and 3D charts. Moreover, these tools can be used for efficiency analysis because they show the averages of mutual inductance with certain misalignment limits. Also, the areas of over specific top percentages are showed. The first figure (Figure 44) shows the mutual inductance profiles with zero sideway error, the figure compares the air gaps and the exponential behaviour is easy to see. It shows how mutual inductance changes if the vehicle is driven forward or backward. With small air gaps, the mutual inductance increases rapidly which must be considered when the dynamic charger is designed. Moreover, in the same way, any path of the vehicle could be analyzed.

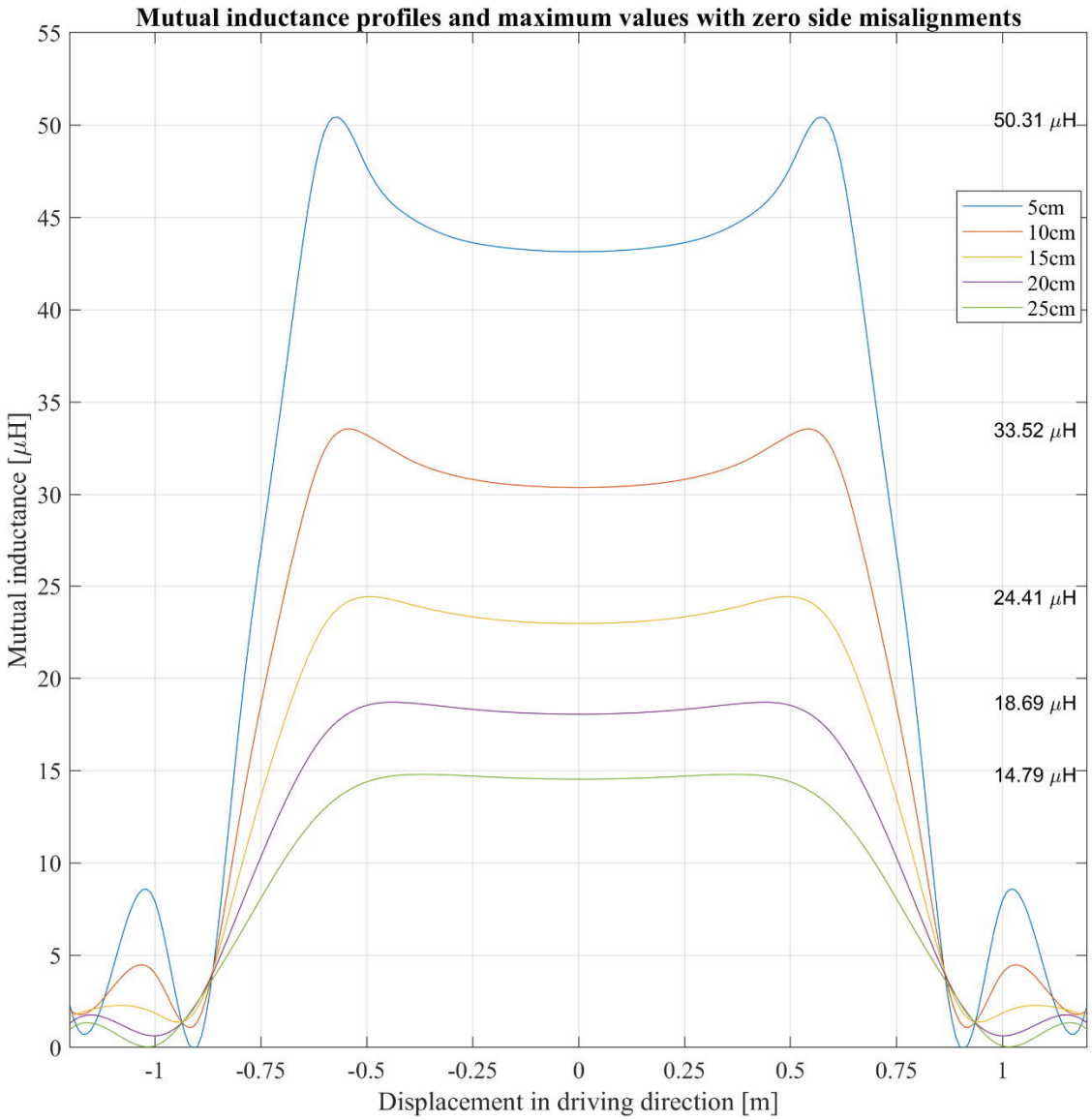

Figure 44. Mutual inductance profiles in the DR for all five air gaps from 5 to 25 cm with zero sideway error. The figure shows that mutual inductance is changing exponentially as a function of the air gap. These graphs were interpolated in MATLAB to make the appearance smoother.

The next figure (Figure 45) shows the average of the mutual inductance over a specific limit. The limit can either be the same fixed limit for all air gaps (for example 14 μH) or a percentual limit when the actual limit depends on the air gap (for example top 20%). This figure is

created with MATLAB, and the fixed and percent limits can be changed in the MATLAB script. Essentially this figure compares the shapes of the mutual inductance maps. Larger air gap usually means larger areas with a percent limit but smaller areas with fixed limits. There is also area multiplied by average mutual inductance -plots for both limit types called "power". It is not actual power transferring energy but it describes the effectiveness of the charging event. These plots indicate the effectiveness of that air gap because it is good to have a wide area with decent mutual inductance. That way the charging is efficient and small misalignment is not a very big problem.

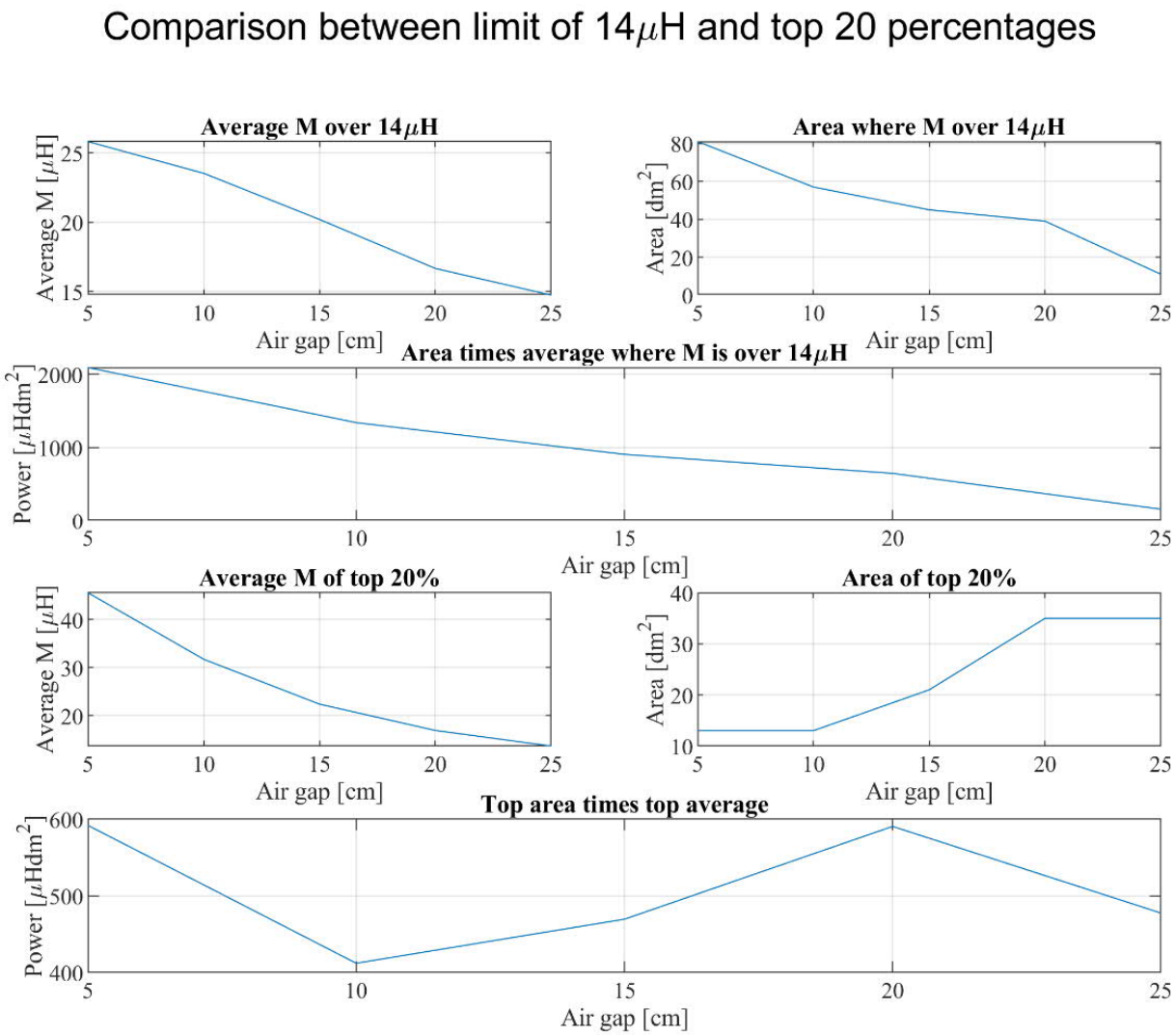

Figure 45 Comparing area and average mutual inductance between the hard limit of 14 μH and top 20%. The areas are different for each air gap because the area depends on both mutual inductance and limit. The area is simply the count of points were mutual inductance is over the specified limit. For example, the top right plot shows that with a 5 cm air gap, there are 80 misalignment points were the mutual inductance is over 14 μH. The top left plot, on the other hand, shows that the average mutual inductance of these misalignment points is slightly over 25 μH. The upper long plot shows the multiplication of area and average mutual inductance; it is called "power" as it describes the effectivity of the air gap. High "power" means that there is either high mutual inductance or larger area or both making it useful for charging. The three plots at the bottoms are the same but with percentual limits.

The next figure (Figure 46) compares the effect of different top percent limits with different air gaps. This figure essentially shows the effect of the percent limit on the area and average mutual inductance. It shows that when the air gap is increased, the area of over certain top percent is also increased. On the other hand, increasing the air gap will decrease the average mutual inductance over a satisfied top percent.

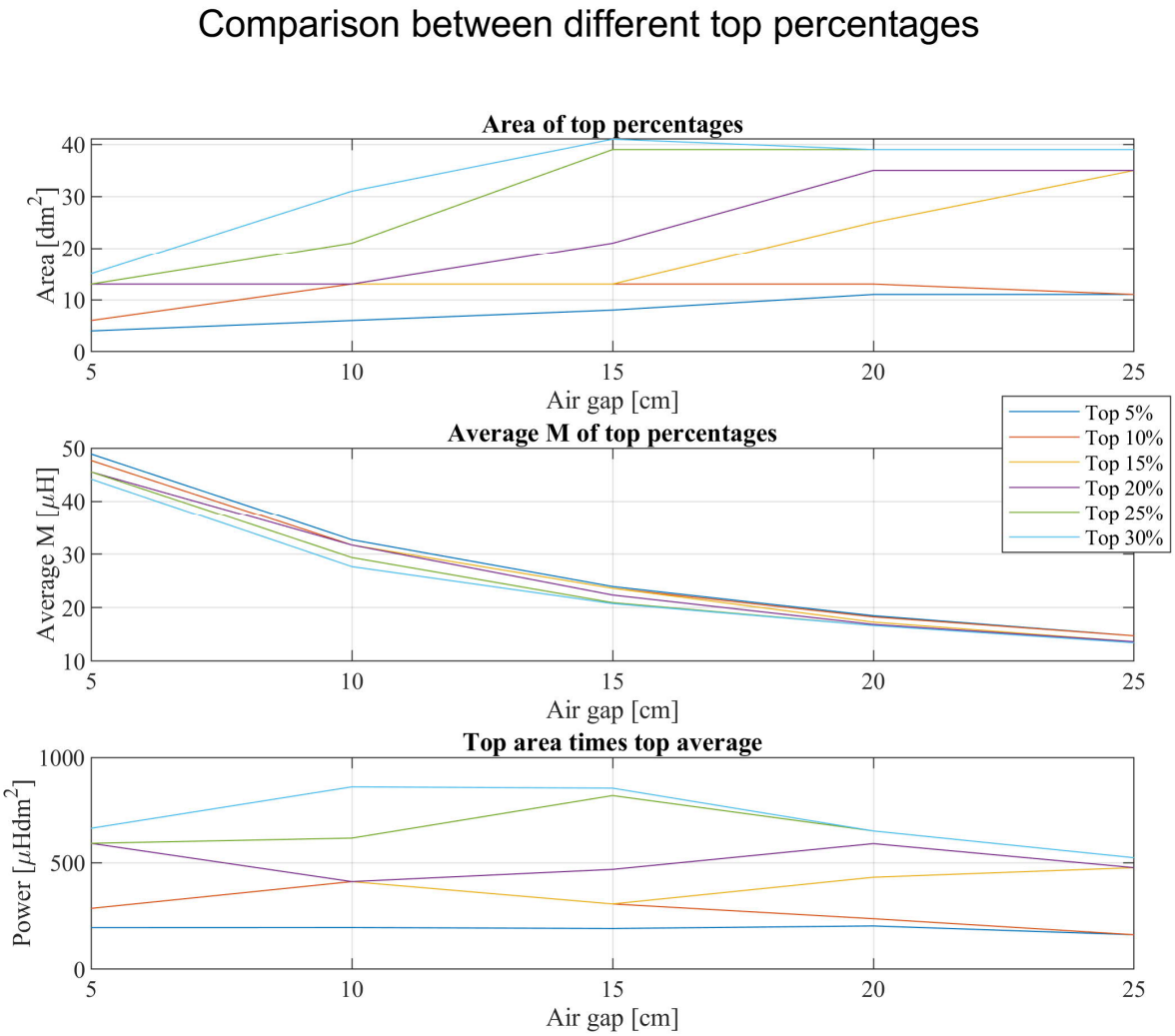

Figure 46. Comparing different top percentages with different air gaps. Increasing the air gap or top limit will also increase the area. However, the average mutual inductance in that area is inversely proportional to the air gap and proportional to the top percentages.

The last three figures shortly presented a few ways of analyzing mutual inductance. One could expand the analysis as needed but it will go out the scope of this thesis. The main focus was on evaluating the mutual inductance for current tuning and efficiency analysis.

3.1.2 Current tuning and transferred power

After the mutual inductances have been evaluated, the acquired data can be used for current tuning. This means that the transmitter and receiver currents are tuned individually for each misalignment to maintain the following conditions: transferred power is under 20 kW, transmitter current is under 36 A RMS, and receiver current is under 75 A RMS. The previous

values for power and currents are obtained from Cirimele's thesis and they provide very realistic constraints for the system. The currents were tuned as described in chapter 2.3 which produced the following figures from Figure 47 to Figure 51.

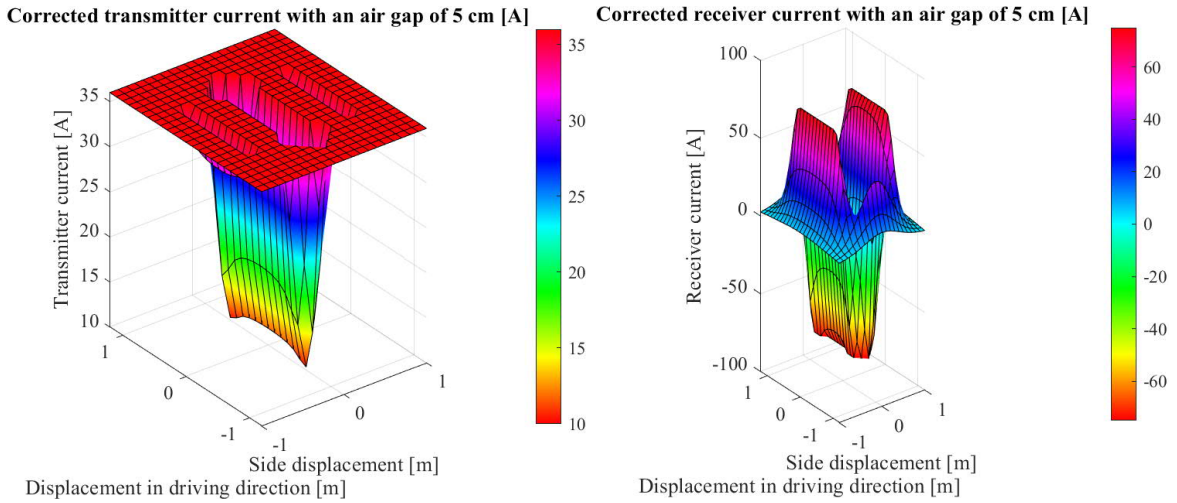

Figure 47. Corrected RMS transmitter and receiver currents with an air gap of 5 cm. With high mutual inductances, the transmitter current is limited more than with small mutual inductances.

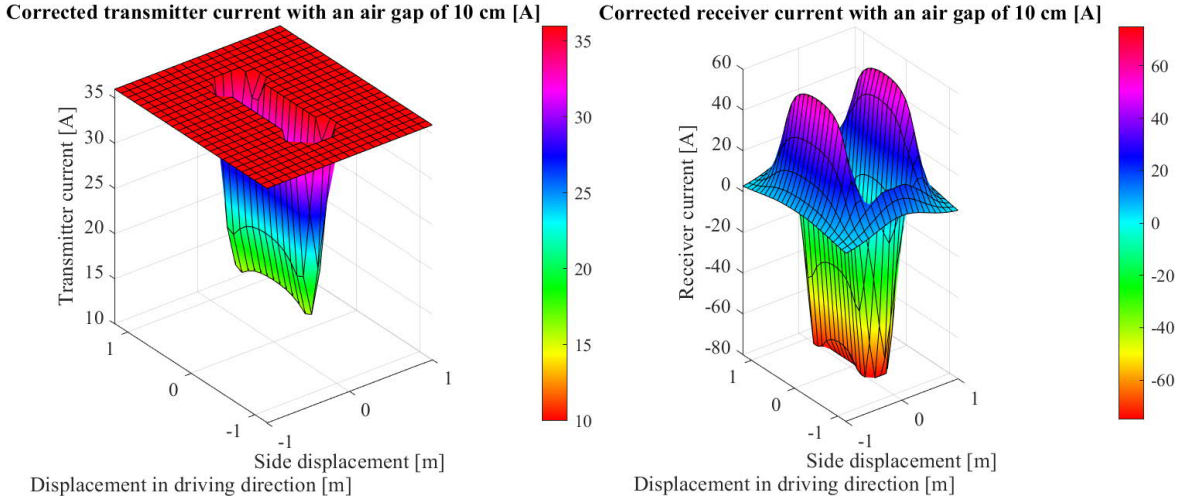

Figure 48. Corrected RMS transmitter and receiver currents with an air gap of 10 cm.

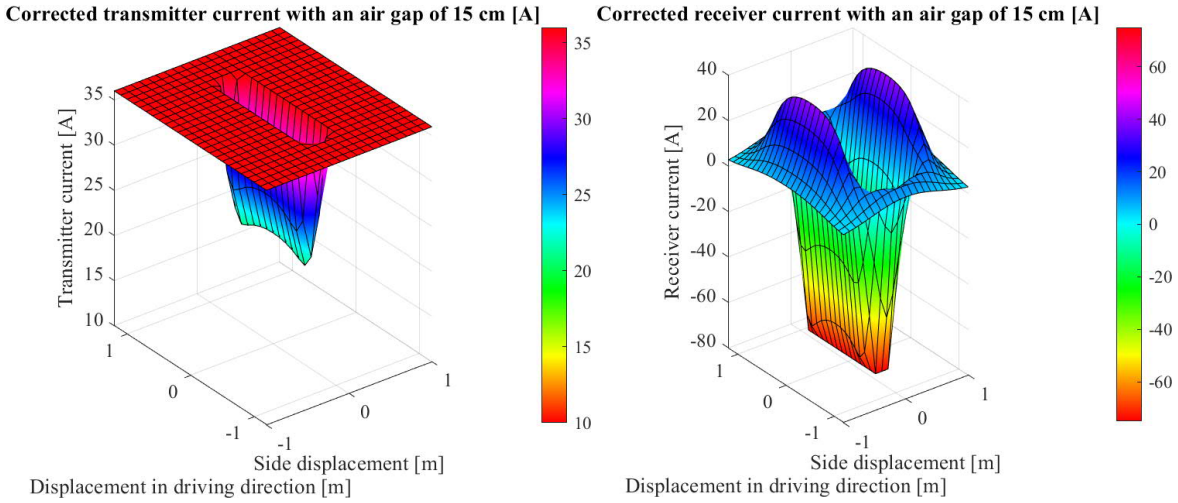

Figure 49. Corrected RMS transmitter and receiver currents with an air gap of 15 cm.

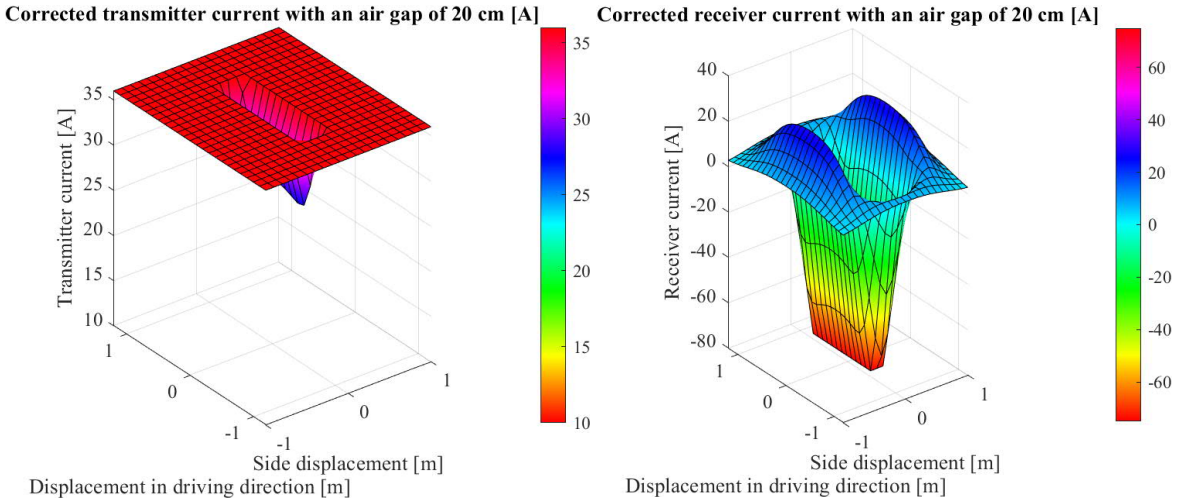

Figure 50. Corrected RMS transmitter and receiver currents with an air gap of 20 cm.

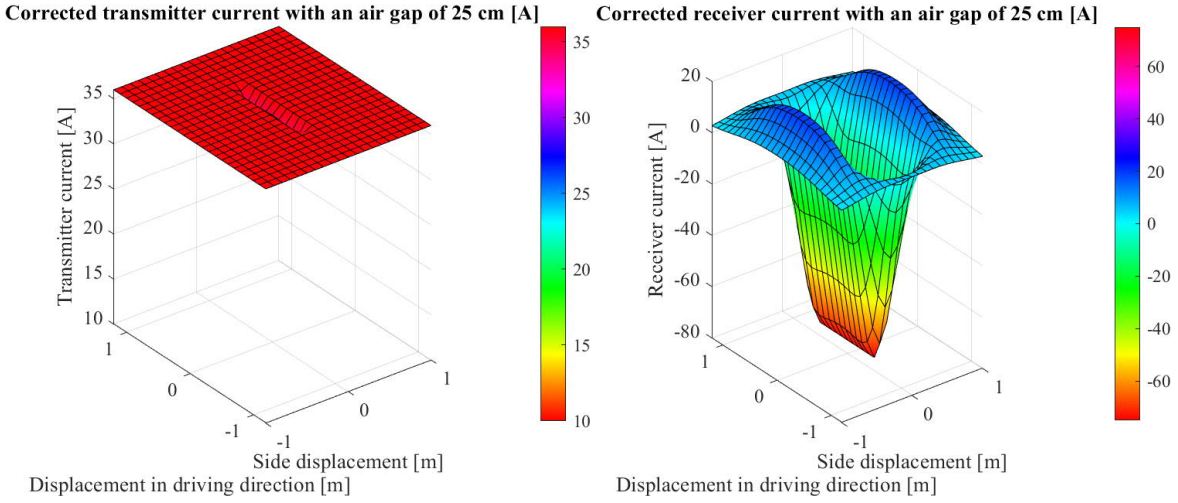

Figure 51. Corrected RMS transmitter and receiver currents with an air gap of 25 cm. When mutual inductance was low, both transmitter and receiver current were not limited.

Using the corrected currents and obtained mutual inductances, the power of the charger was evaluated (from Figure 52 to Figure 56).

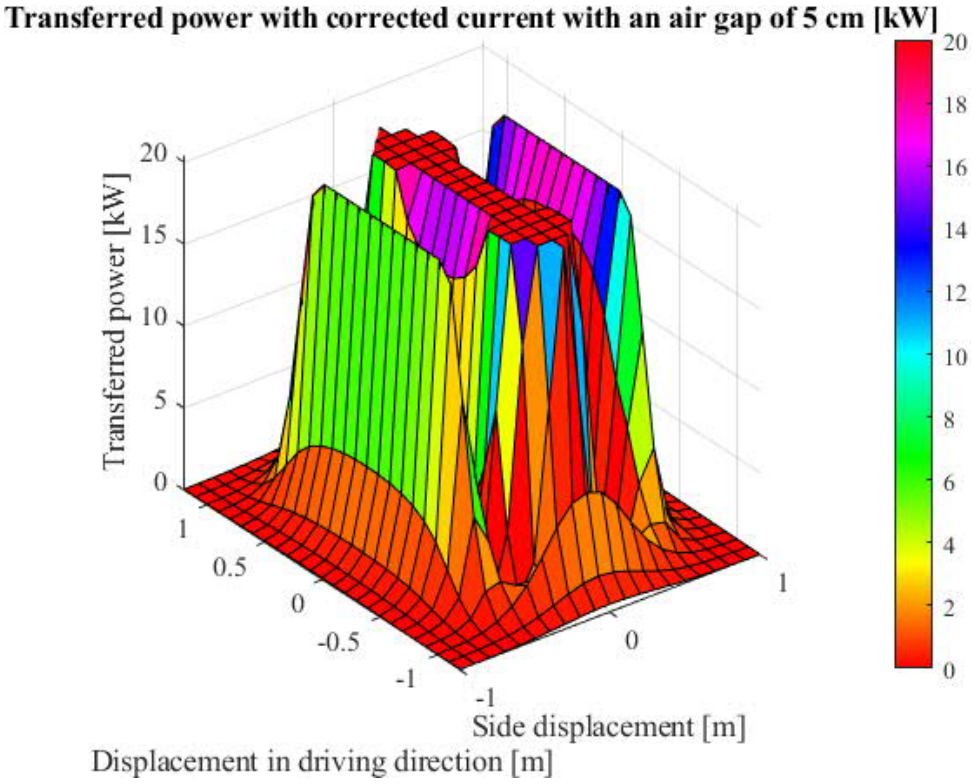

Figure 52. Transferred power with a 5 cm air gap.

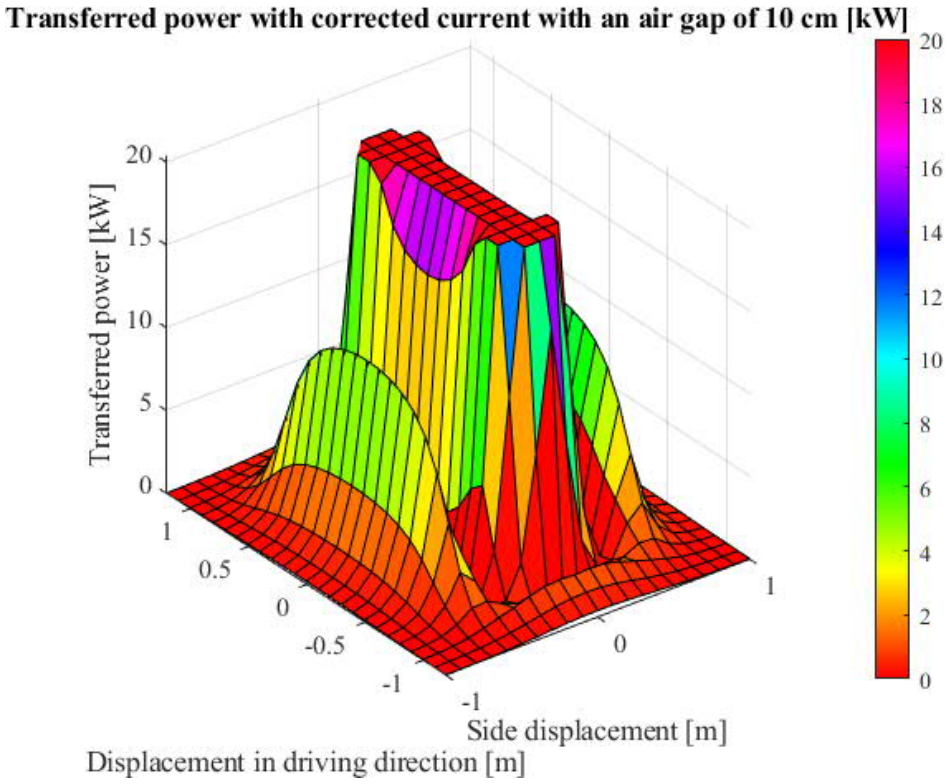

Figure 53. Transferred power with a 10 cm air gap. Transferred power is highest with small misalignments but with larger misalignments, the mutual inductance is insufficient for 20 kW power.

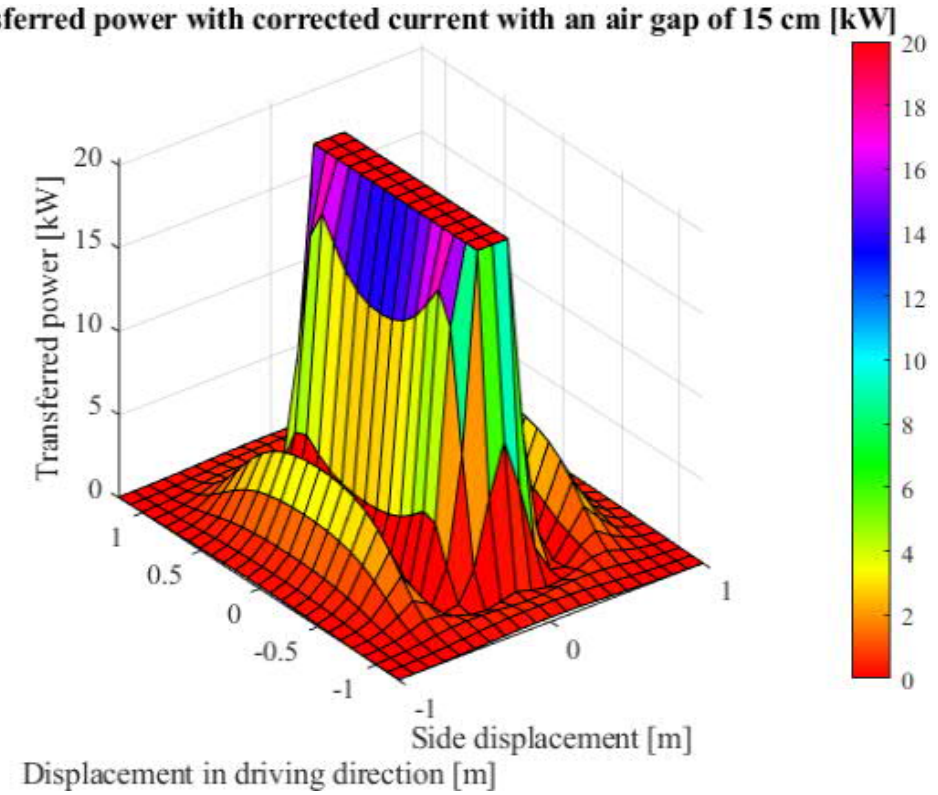

Figure 54. Transferred power with a 15 cm air gap. Transferred power is highest with small misalignments but with larger misalignments, the mutual inductance is insufficient for 20 kW power.

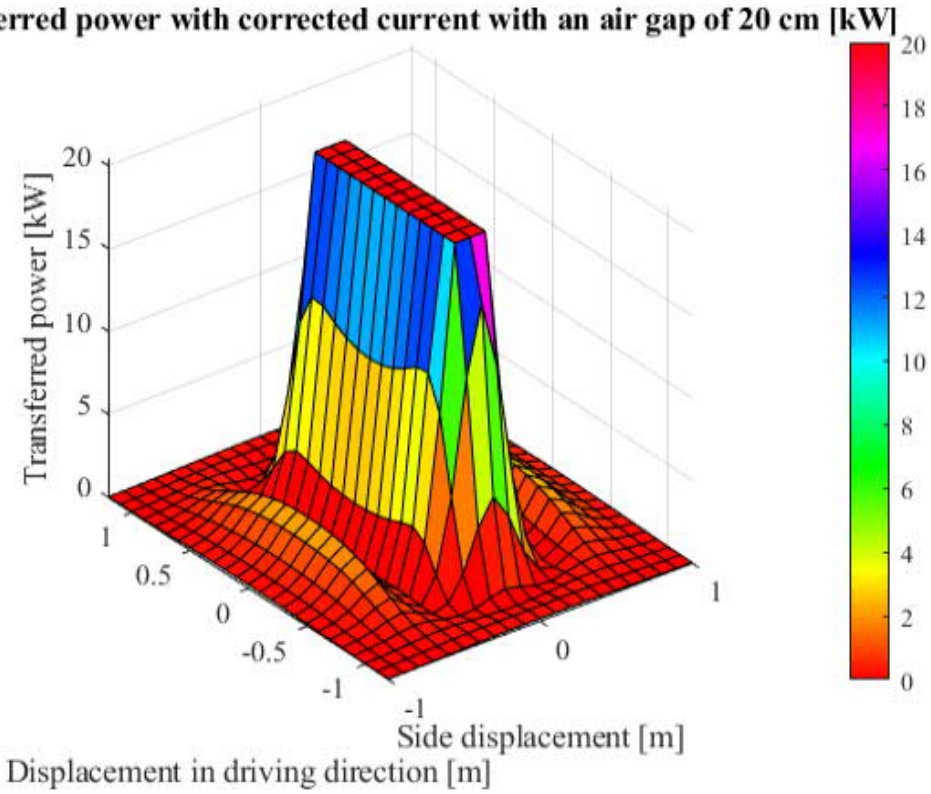

Figure 55. Transferred power with a 20 cm air gap. Transferred power is highest with small misalignments but with larger misalignments, the mutual inductance is insufficient for 20 kW power.

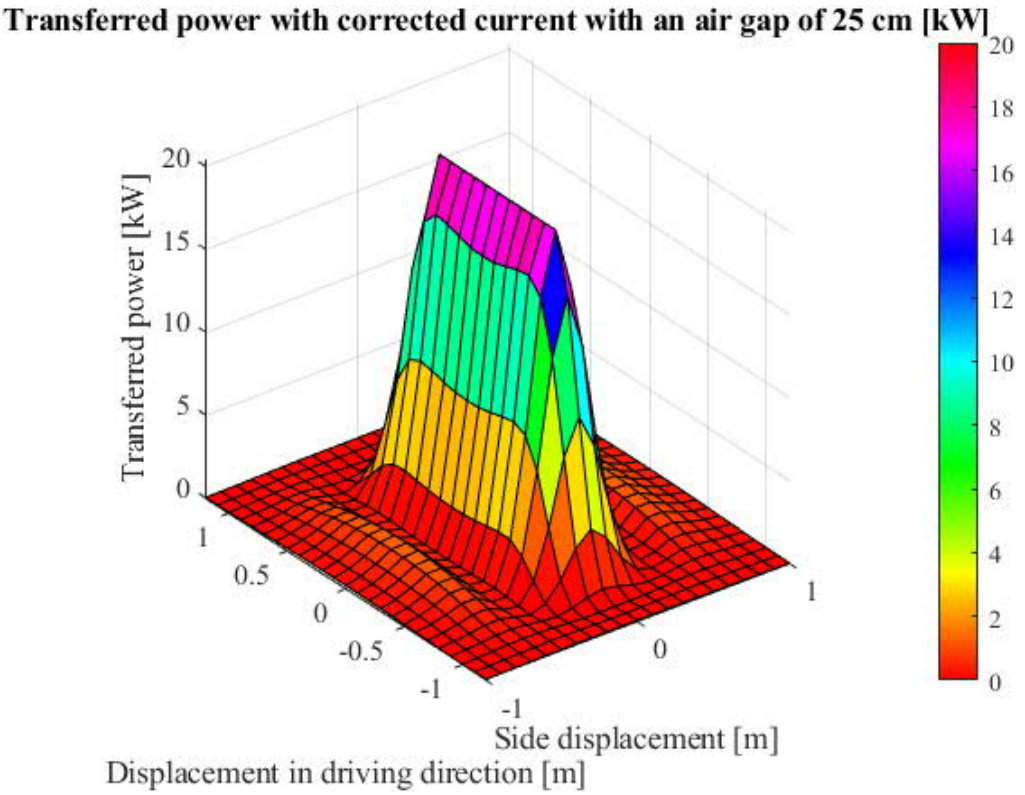

Figure 56. Transferred power with a 25 cm air gap. Transferred power is highest with small misalignments but with larger misalignments, the mutual inductance is insufficient for 20 kW power.

Transferred power was saturated to 20 kW with small misalignments with air gaps of 5 cm, 10 cm, 15 cm and 20 cm. However, with a 25 cm air gap, the mutual inductances were insufficient to provide as high power. Nevertheless, with all air gaps, the maximum power was acquired only with small misalignments as one would have expected. Next, the charger efficiency is analyzed with two different equations.

3.1.3 Efficiency

Charger efficiency is estimated using equations (1) and (2). Equation (1) was used with simulated mutual inductance and provided coil resistances along with the total equivalent load whereas equation (2) was used with actual transmitter and receiver currents, given resistances and simulated induced losses. Furthermore, the simulated model is based on Cirimele's thesis, so the provided resistance values can be used for coil resistances and, these measured values are an excellent way to take the skin and proximity effects into account as these effects are difficult to simulate with FEM [5]. Cirimele provides resistances 128 mΩ and 359.3 mΩ for transmitter and receiver coils, respectively. Efficiencies obtained using equation (1) are referred to as Cirimele's efficiencies, and efficiencies obtained using equation (2) are called Thesis' efficiencies. These names are given to make the comparison more manageable and the names are in use only in this thesis. Next, the two efficiencies are presented with figures from Figure 57 to Figure 61. In these figures, the data was interpolated using MATLAB interp2 spline function to get a matrix of 63x75x5 grid with 23 625 data points. This interpolation resulted in a very smooth graph for both visual and numerical use.

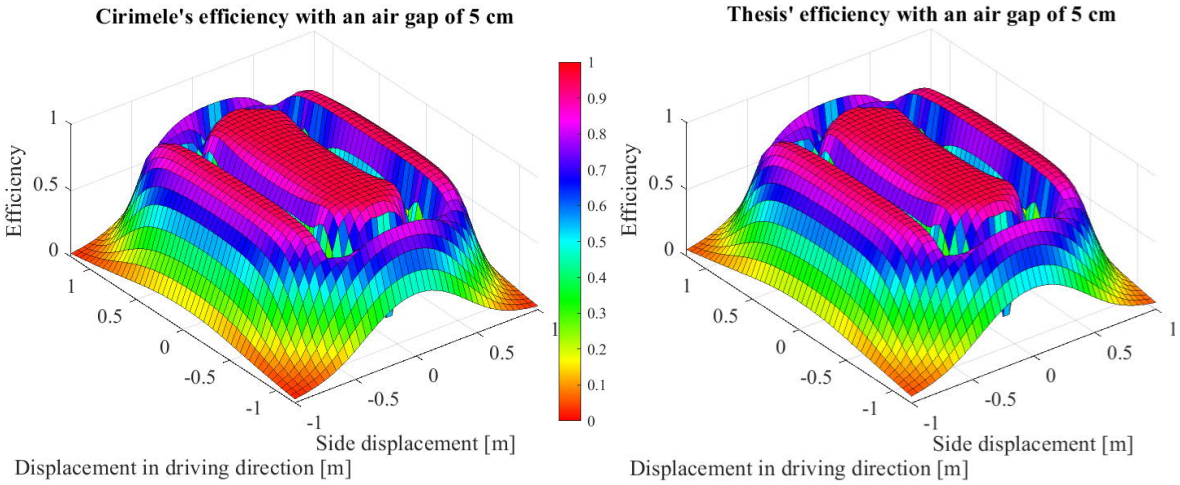

Figure 57. Cirimele's and Thesis' efficiencies with an air gap of 5 cm. Yet this first comparison shows that there is no significant difference between these two efficiencies.

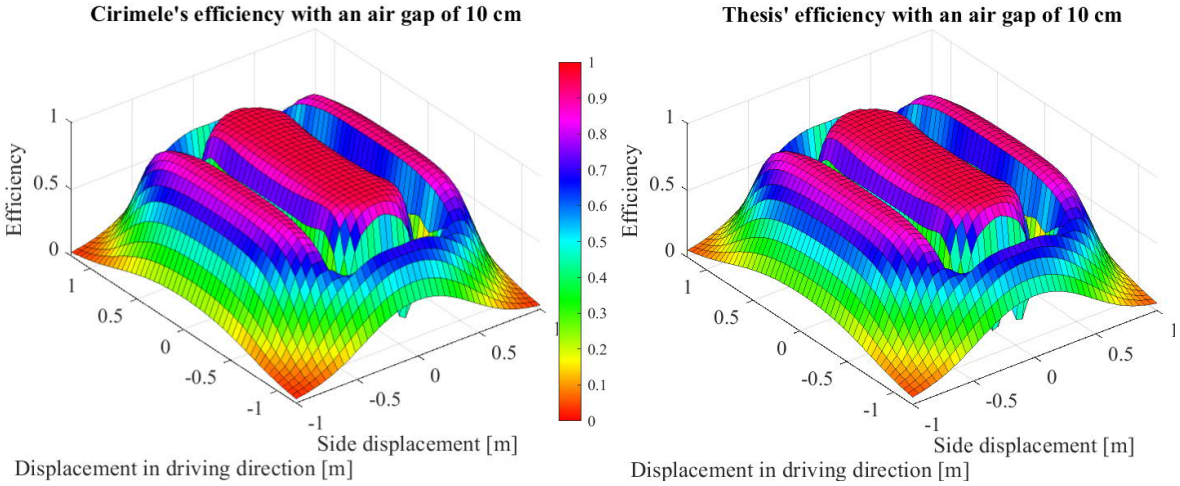

Figure 58. Cirimele's and Thesis' efficiencies with an air gap of 10 cm.

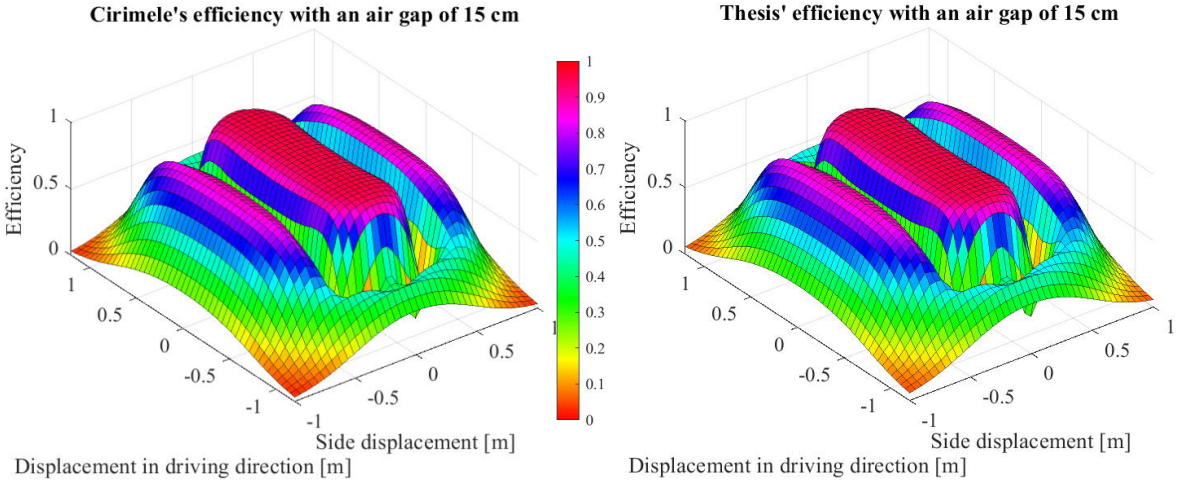

Figure 59. Cirimele's and Thesis' efficiencies with an air gap of 15 cm.

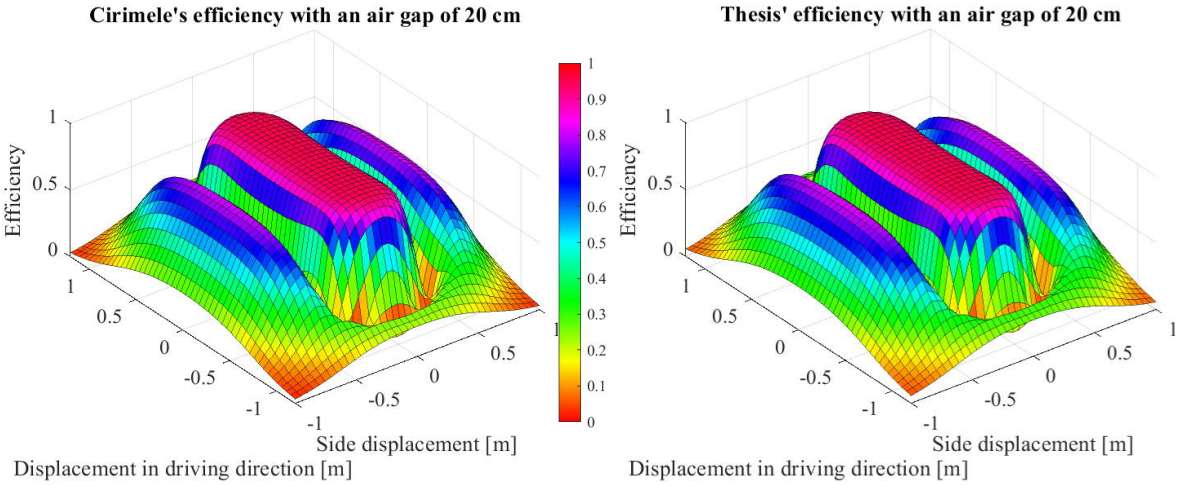

Figure 60. Cirimele's and Thesis' efficiencies with an air gap of 20 cm.

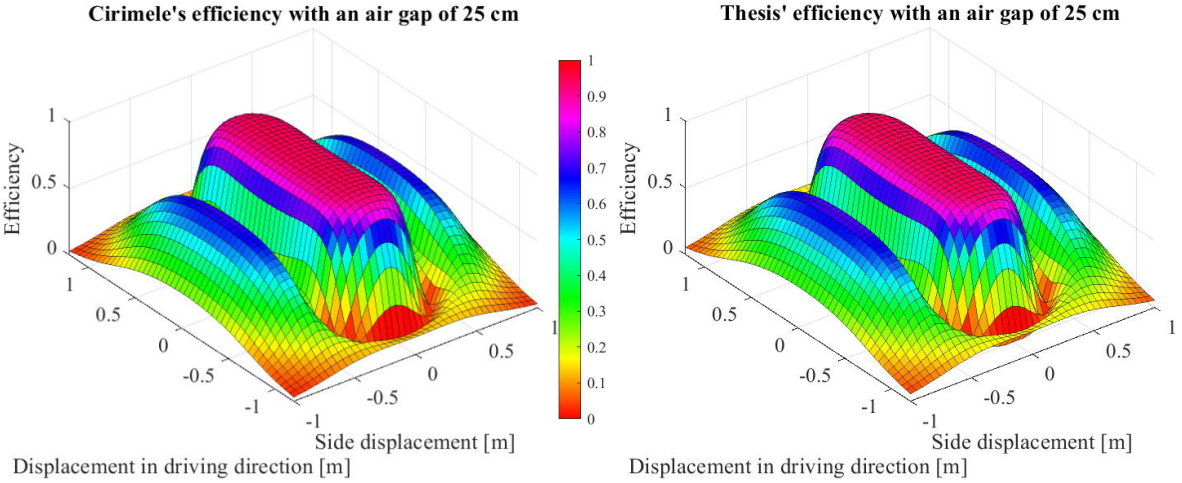

Figure 61. Cirimele's and Thesis' efficiencies with an air gap of 25 cm.

All the previous efficiencies match each other well, and no significant difference was found. Furthermore, both efficiencies described that the charger has high efficiency with small misalignments (over 90 %), and that the efficiency is zero when the mutual inductance is zero. However, these figures only showed the overall appearance of the efficiencies and therefore, the efficiencies were evaluated and compared on the MA (Table 14).

Table 14. Comparing Cirimele's and total efficiencies in MA (misalignments; ±0.1 sideways and ±0.6 in driving direction). Cirimele's efficiency tends to be slightly higher than the Thesis' efficiency for all air gaps, but no significant difference was found.

Air gap [cm]	Cirimele's efficiency [%]	Thesis' efficiency [%]
5	96.18	95.87
10	95.95	95.65
15	95.56	95.28
20	94.99	94.72
25	94.14	93.89

Although Cirimele's efficiency was slightly higher than the Thesis' efficiency on the MA, the difference is insignificant. Hence, it can be conducted that both of the equations can be trusted. However, this might not be the case for different wireless chargers where the induced losses can be more significant. Next, the vehicle speed and trajectories are considered.

3.2 Vehicle speed and trajectories

The effect of vehicle speed on mutual inductance was evaluated with three different speeds; 0, 60 and 600 km/h using the TDM. This analysis showed that vehicle speed has an insignificant effect on mutual inductance with the frequency of 85 kHz and within these speeds. To be more precise, the difference is not shown until the fourth or the fifth decimal, and it can be caused by computing error as much as by vehicle movement.
It was very computing heavy to simulate the full pass with TDM, and therefore the dynamic simulation was made near the nominal position during a short real-life time. It means that the coils were moved only very little relative to each other, but it is not a problem because the speed was correct. Moreover, it was noticed that the parametric FDM could also be used for dynamic simulations since one can extract the time-varying mutual inductances from the provided spatial mutual inductance maps if the vehicle velocity is known. This mutual inductance can be then inputted into a circuit simulator to reveal the real behavior of a wireless charger. It should be noted that this thesis is not considering the electrical circuits and so the fast pass over the charger may affect unpredictably since the mutual inductance is changing quite rapidly after all. Nevertheless, three full pass trajectories were analyzed using the data provided in the mutual inductance maps.

As stated earlier, the fast pass over the receiver can affect the charging but also the direction of travel has an effect. Trajectories affect if three ways: i) the mutual inductance gradient depends on trajectory ii) mutual inductance magnitudes depends on the trajectory, iii) time over the transmitter depends on the trajectory. Therefore, three different trajectories were analyzed in terms of mutual inductance using the FDM. The three inspected trajectories intersect at the center of the receiver coil (Figure 62).

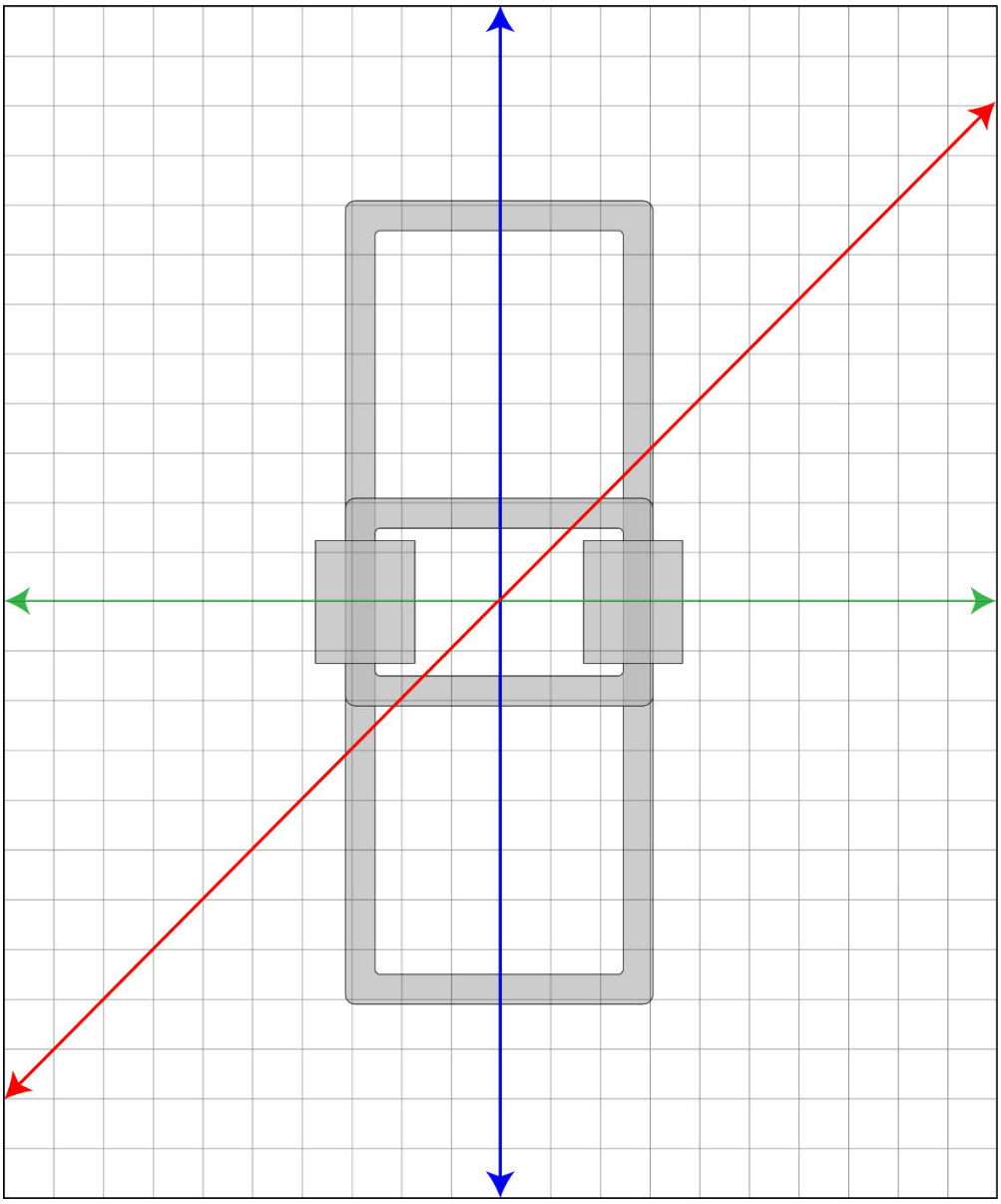

Figure 62. The three inspected trajectories. Blue in driving direction, green in sideway direction and red in diagonal.

The blue line in Figure 62 presents the preferred way in dynamic charging. Furthermore, the transmitter coil has been designed to offer a steady value of mutual inductance when a vehicle passes the charger in that direction [9]. Passing in sideway direction or diagonal, the mutual inductance is not as steady and the car passes the charger quicker which leads to not so effective charging. Figure 63, Figure 64 and Figure 65 present the mutual inductances for these three trajectories with all five air gaps.

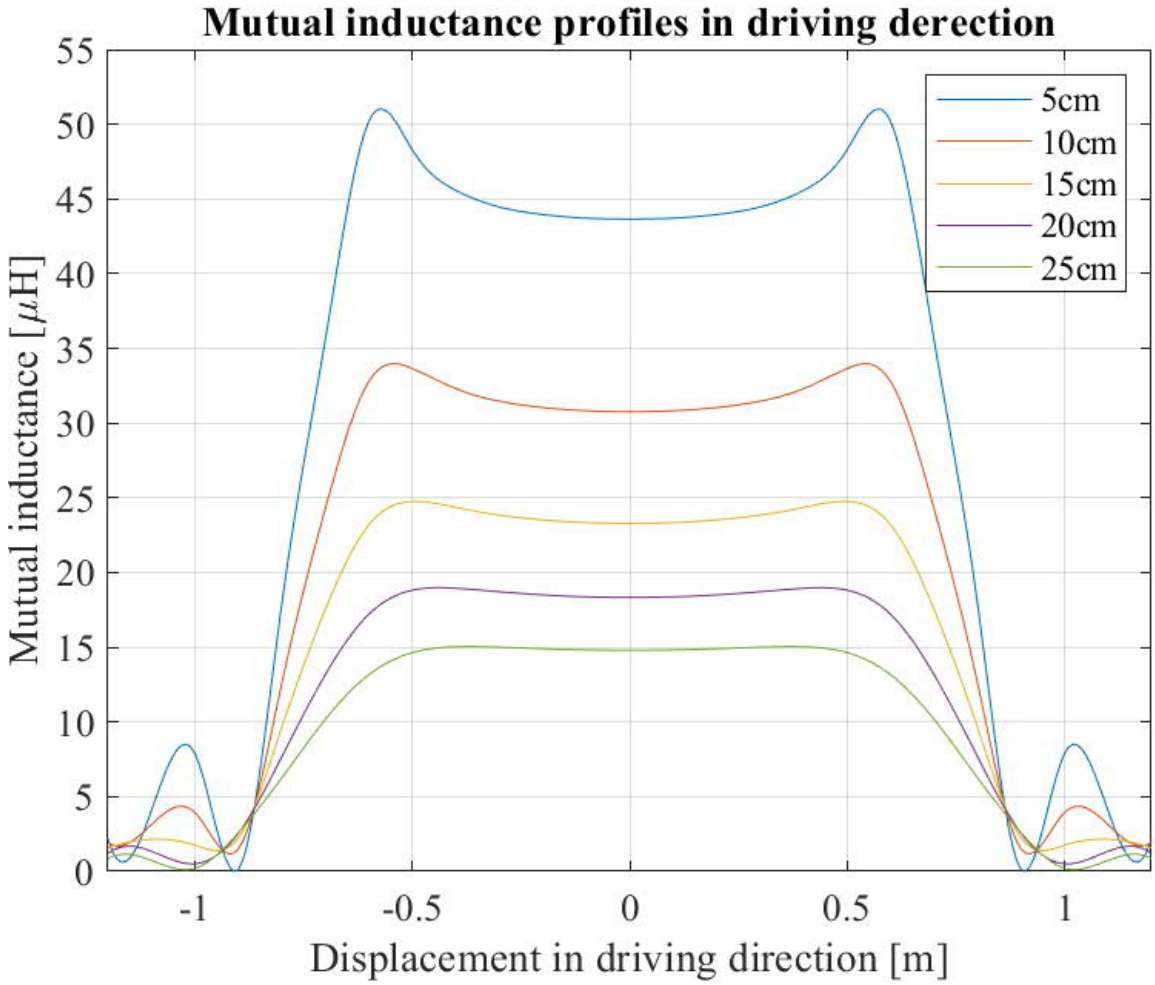

Figure 63. The trajectory in the driving direction. Mutual inductance has rather constant values when the vehicle passes the transmitter in driving direction which is also the preferred situation in dynamic charging. That way the charging could happen during a longer time than with the other two trajectories.

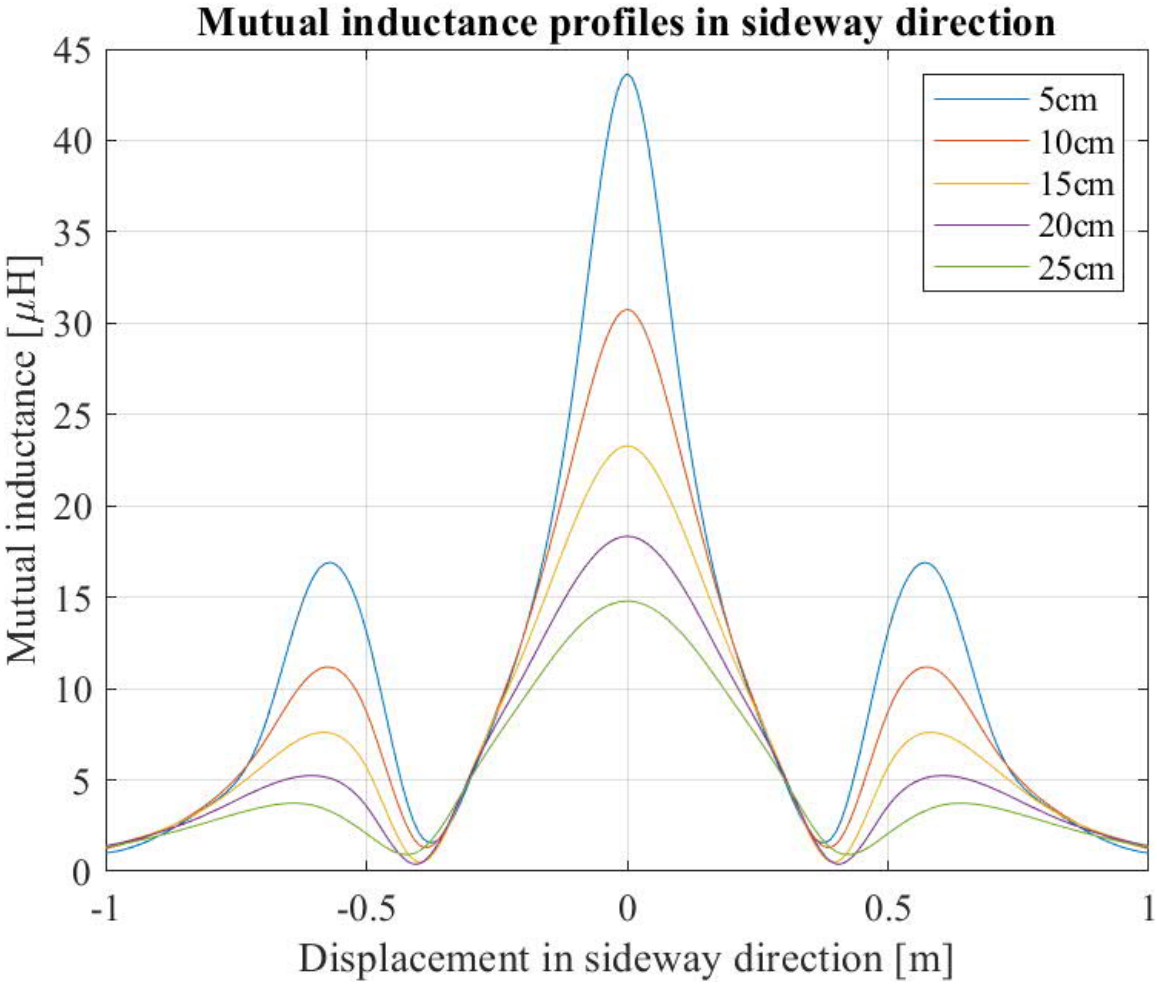

Figure 64. The trajectory in the sideway direction. When passing the charger sideways, the mutual inductance is lower than with a pass in driving direction. Moreover, the sideway direction does not provide a steady value for mutual inductance.

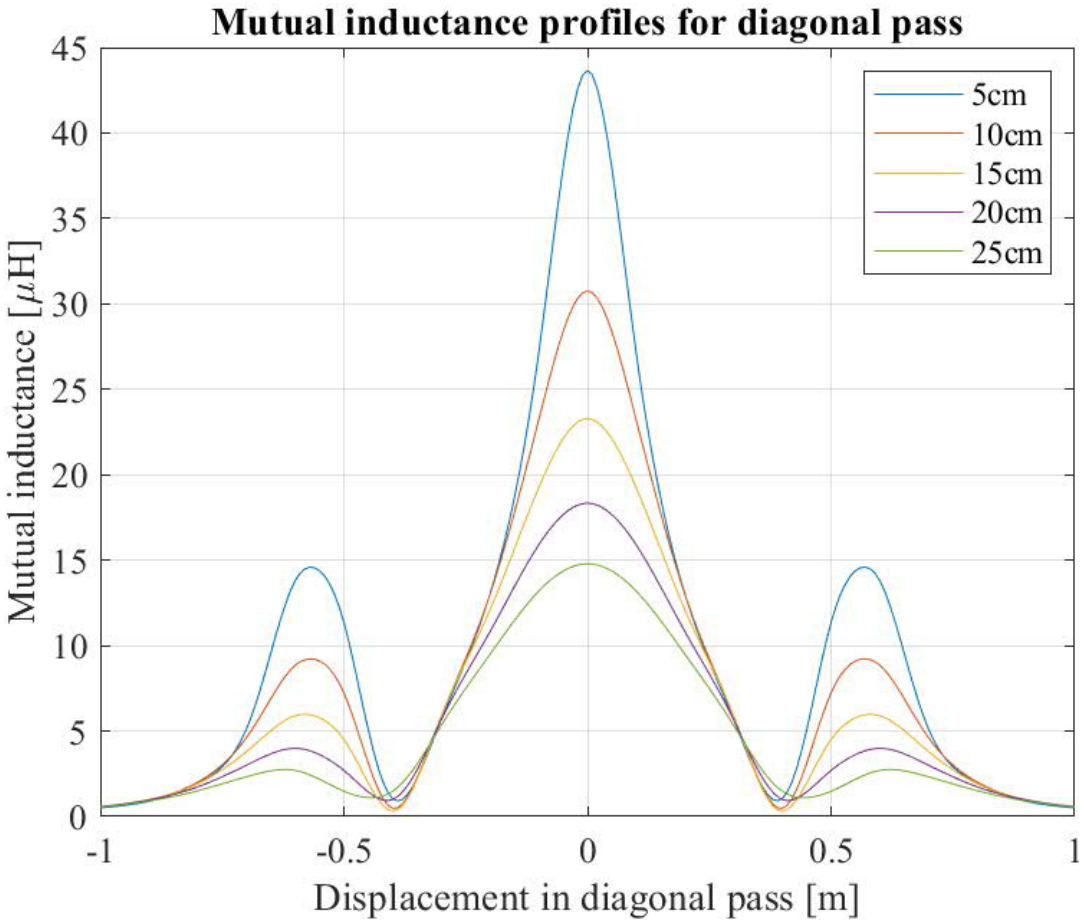

Figure 65. The trajectory in the diagonal pass. When passing the charger diagonally, the mutual inductance profiles resemble the previous situation with the sideway pass.

As the short analysis showed, the charging is most efficient in driving direction. This is caused by the relative shapes of the coils. Moreover, the charger was designed to offer efficient charging in driving direction, and it seems to work.

3.3 Different ferrite assemblies

The original ferrite assembly was compared with four new assemblies presented in figures from Figure 66 to Figure 70.

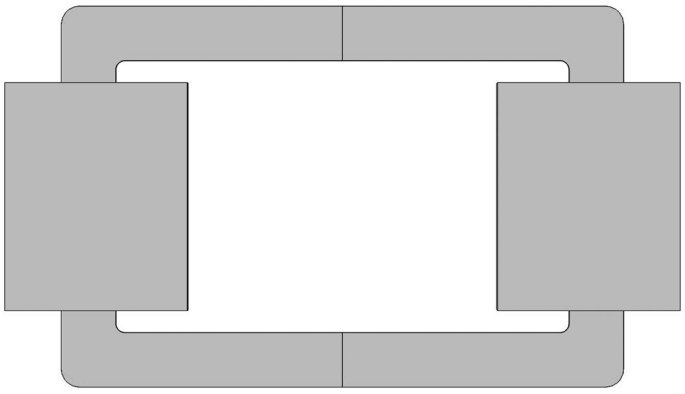

Figure 66. The Original ferrite assembly. This assembly was designed and optimized in [5]*, which provides a good starting point for the analysis.*

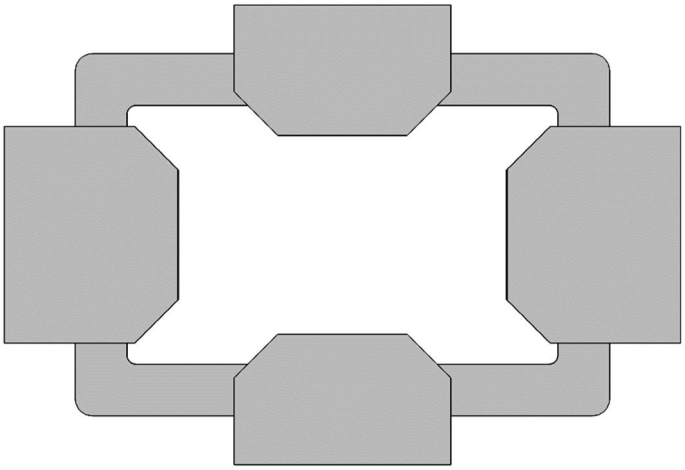

Figure 67. The Monolith ferrite assembly. This design is based on the Original design. Square corners inside the receiver were removed, and two more pieces of ferrite were added in the hope of getting higher mutual inductance. However, this makes the Monolith model heavier than the Original design.

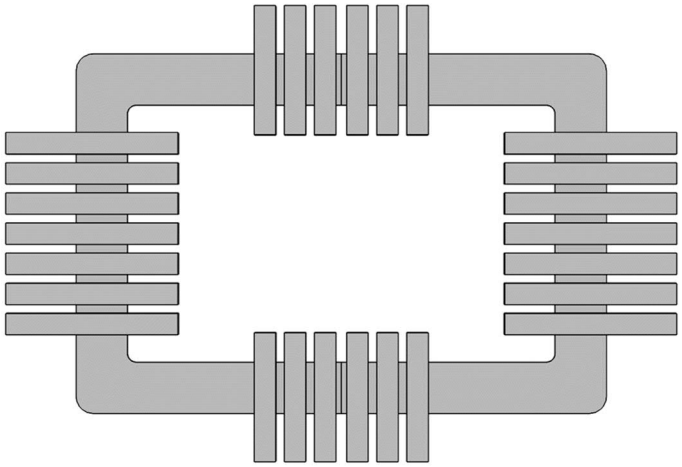

Figure 68. The Sticks ferrite assembly. This design is a light weighted version of the Monolith design. It was assumed to provide as high mutual inductance as the Monolith design but with less mass.

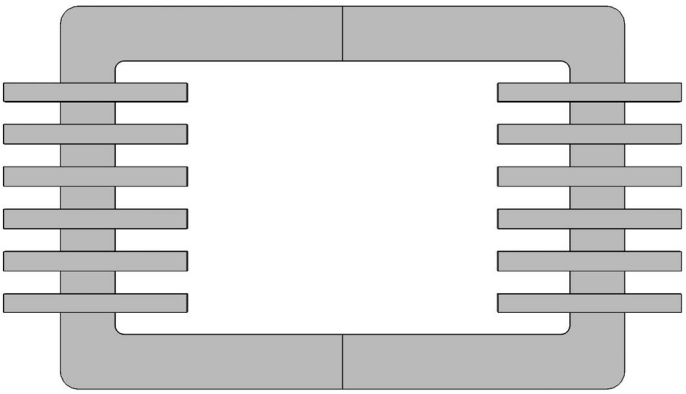

Figure 69. The Striped ferrite assembly. This model represents the light weighted version of the Original design. It was assumed that it would provide performance similar to the Original design but with less mass.

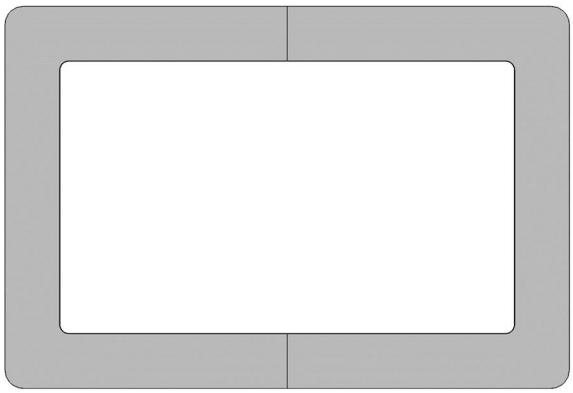

Figure 70. Lastly, there is the Empty ferrite assembly. This design was added to the study to see how much the ferrite increases the performance.

Monolith and Sticks were designed to increase mutual inductance, and Striped was designed to reduce the mass of the receiving unit. Moreover, Empty was added to the study to see the effect of the ferrite core. Furthermore, Figure 71 confirms that without any ferrite, as in Empty, the mutual inductances will be much lower than with other assemblies. Also, the figure shows how little there is difference between Monolith and Sticks assemblies and between Striped and Original assemblies.

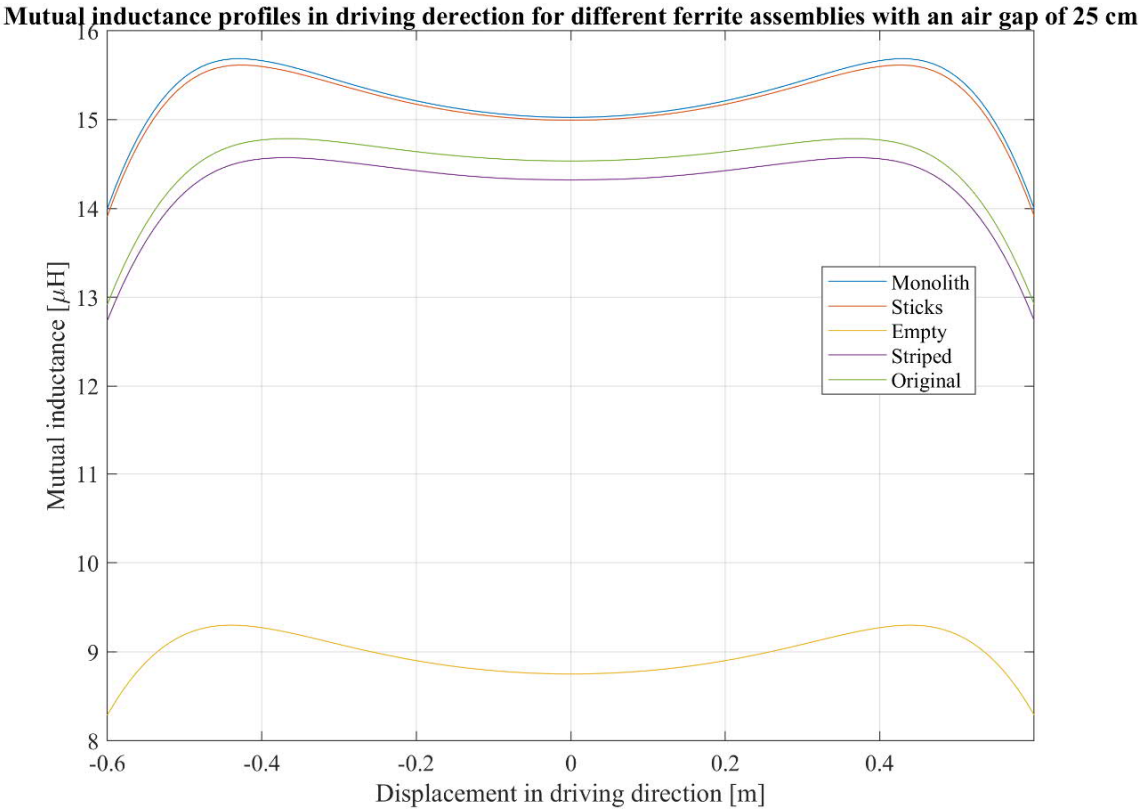

Figure 71. Mutual inductance profiles for different ferrite assemblies in driving direction with an air gap of 25 cm. This figure shows that without any ferrite, the mutual inductance is much lower than with a ferrite.

Next, mutual inductances and masses of these assemblies were compared. This comparison describes much about these different assemblies because mutual inductance affects charging

power and efficiency, whereas mass affects EV's consumption[4]. Table 15 present the mutual inductances of these assemblies in MA for both 20 cm and 25 cm air gaps with ferrite volumes and masses.

Table 15. Average mutual inductances for MA (misalignments; ±0,1 sideways and ±0,6 in driving direction) with all different ferrite designs. Also, ferrite assembly volumes and masses are presented. Ferrite density of ρ=4750 kg/m^3 was used.

Assembly	Average Mutual inductance 20 cm [µH]	Average Mutual inductance 25 cm [µH]	Ferrite volume [m^3]	Ferrite mass [kg]
Original	16.67	13.48	0.0025	11.875
Monolith	17.47	14.01	0.004125	19.494
Sticks	17.39	13.97	0.002875	13.656
Striped	16.32	13.29	0.00125	5.938
Empty	10.34	8.25	0	0

As predicted, the Monolith and Sticks assemblies were heavier than the original assembly but they also provide slightly higher average mutual inductance. On the other hand, Striped assembly provides almost the same mutual inductance than the original assembly but with much less mass. Figure 72 visualizes this relationship between the average mutual inductances and masses of these ferrite assemblies.

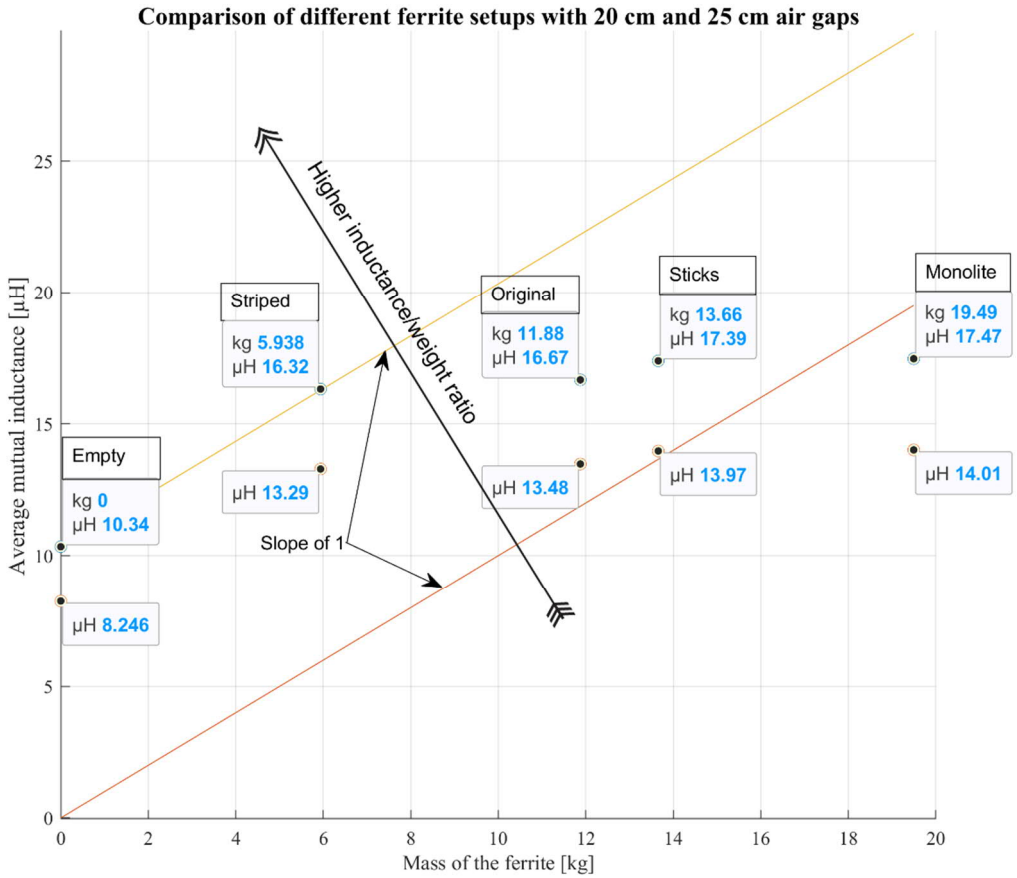

Figure 72. Comparison of the different ferrite assemblies with slopes of one for both 20 cm and 25 cm air gaps. If the mass is compared against the average mutual inductance, the Original design is roughly at the same level as the Sticks model, whereas the Monolith model is significantly heavier. Surprisingly, Empty and Striped assemblies are on the same slope line meaning that they are as good relative to this penalty function. Most importantly, Striped assembly is on a higher slope line, meaning that it could be a better solution than the Original assembly. However, the Empty assembly will be the best option if the mass is the most important selection criterion.

The previous figure shows that the Monolith assembly is the heaviest relative to mutual inductance while Original and Sticks are roughly at the same level. Furthermore, Striped and Empty are on the same highest level, Empty being lighter and Striped having a higher mutual inductance. This means that Striped and Empty are more suitable ferrite assemblies than the original when mass/mutual inductance ratio is considered. Furthermore, the efficiencies of these assemblies were also evaluated (Table 16).

Table 16. Comparing Cirimele's efficiencies in MA (for misalignments; ±0.1 sideways and ±0.6 in driving direction) with five different ferrite assemblies with a 25 cm air gap. There is no significant difference between the Original, Monolith, Sticks and Striped ferrite assemblies but Empty assembly has clearly the lowest efficiency.

Design	**Cirimele's efficiency [%]**
Original	94.14
Monolith	94.42
Sticks	94.40
Striped	94.07
Empty	90.52

When considering both the mass/mutual inductance ratio and efficiency, Striped ferrite assembly can be considered the best. Consequently, Striped assembly allows a lighter receiving unit than Original assembly, which decreases the EV consumption while having almost as high charging power and efficiency [4].

4 Discussion

At the very beginning, an Elmer model was under development, but due to limitations of Elmer, the development was terminated. Fortunately, Polito provided a good base model created with COMSOL. Polito model met the requirements, and it was confirmed by real-life measurements and was used, after slight modifications, for the misalignment and performance analysis as well for the ferrite analysis. The model proved to be a very useful tool for the use of this thesis. Next, the most significant aspect of the thesis is discussed.

4.1 Ferrite and shield materials

The first significant and foremost task was to select materials for shield and ferrite core. This step was crucial for the whole modeling process because the materials are wanted to be consistent throughout the process. Moreover, the material selection offers an excellent opportunity to test the model capabilities as well. The materials were wanted to be light-weighted with low losses. As a result, both ferrite core and shield materials were changed from the original design. The new materials, ferrite 3C95 and 1050-H14 aluminum, provide smaller losses which increased the charger efficiency.
Moreover, the material selection process revealed the main selection principles when light and efficient structure is wanted. Furthermore, this knowledge can be used in future research too as a baseline for more comprehensive material assessment. One interesting detail that was found was that the ferrite core should have high electrical resistivity, while shield material should have low electrical resistivity. Also, it was found that shield can be modeled with impedance boundary conditions, which reduced the computing efforts.

4.2 FDM vs TDM

FDM was suitable for misalignment and air gap analysis but not directly suitable for moving coils. Therefore the TDM model was created. Measurements verified the FDM model, and the TDM was compared to the FDM. These two models match each other quite well and can be used together for the comprehensive modeling of a wireless charger. TDM can be used for moving coils, as mentioned previously, but also for analyzing different waveforms and different time-varying parameters while FDM assumes that all variables are changing sinusoidally. However, TDM showed that mutual inductance is not dependent on the vehicle velocity but only the relative position of transmitter and receiver coil. Therefore, FDM could be used for analyzing different vehicle trajectories even though it uses a compilation of independent static solutions. Nevertheless, this is thanks to the TDM which proved that the velocity does not matter.

4.3 Performance analysis

At the beginning of the performance analysis, it was found that mutual inductance is proportional to the air gap between the coils. Moreover, the shapes of the mutual inductance maps are unique for each air gap due to the fact that a small air gap increases the coupling between the coils and larger gaps decreased it. Hence, the small air gap results in a high and sharp map, whereas larger gaps form smoother and lower maps. For this reason, the small air gaps are prone to misalignment errors while larger gaps can have larger positioning tolerances without losing the mutual inductance.
The mutual inductance maps were then further used for calculating the power and efficiency of the charger. Charging power was evaluated using corrected transmitter currents which

revealed that the charger is capable of 20 kW charging power with small misalignments with all of the five air gaps (5 cm, 10 cm, 15 cm, 20 cm and 25 cm). Furthermore, the efficiency was calculated with two different equations (equation (1) and equation (2)) to compare the difference between these two. The first equation was provided by Cirimele [5], and the other was a slightly modified version of that. It turns out that there was little difference between these two equations and it might due to low induced losses in the charger. Besides, it was found that mutual inductance, charging power and efficiency maps resemble each other.
Despite that these analyses showed high power and efficiency with high mutual inductance, the situation might differ in real life. Furthermore, research has shown that high mutual inductance also poses some problems. High mutual inductance increases the electric resistance of the charger and higher input voltage is needed [14]. Moreover, increasing the mutual inductance will not increase the efficiency endlessly but instead, there is an optimal value for mutual inductance [25]. However, the simulation of the electric circuit was not considered in this thesis. Nonetheless, the methods described in the thesis can also be applied for obtaining the optimal value of mutual inductance with the smallest losses and mass, as for obtaining the maximum value.

4.4 Vehicle velocity and trajectories

It was found that the vehicle velocity has an insignificant effect on the mutual inductance and the performance of wireless charging. Moreover, it is very computational heavy to simulate moving coils since the excitation frequency is very high. In order to get good results, multiple solutions are needed to compute in every period. This results in very tiny time steps, which will further increase the computing time since the coils hardly move during one period. Later on, it turned out that the FDM model can also be used to simulate coil movement by calculating multiple individual solutions and combining them into one big grid of solutions representing the movement. This is due to the fact that the velocity does not affect on mutual inductance, and movement can be therefore described with individual solutions, as mentioned previously.
Trajectories were considered by comparing three different vehicle trajectories. This comparison showed that the vehicle trajectory affects the mutual inductance profile during the pass over the charger. The mutual inductance profiles will further affect the charging power and efficiency. Moreover, it was found that passing the charger in the driving direction was the most efficient way. Driving direction provides the highest mutual inductance with constant values while passing in the sideway direction; the mutual inductances were smaller and not very stable.

4.5 Different ferrite assemblies

The last significant aspect was ferrite assemblies which also contributed most to the most significant findings. As the analysis showed, new ferrite assemblies Sticks and Monolith have little difference in terms of mutual inductance. However, both of these new assemblies have higher mutual inductances than the original design. Moreover, Sticks uses less ferrite than Monolith and can be, therefore, considered a better solution. Model Striped also performed sufficiently and it could be a good alternative too having better mass/mutual inductance ration than the Original design. It has a similar kind of mutual inductance map and averages as Original assembly but with less ferrite.
Furthermore, Striped assembly uses less ferrite than Original which leads to the lower energy consumption of EV [4]. Although hysteresis losses in ferrites have not been considered yet, using less ferrite could still provide smaller losses. Without considering losses, using less

ferrite the overall weight of the receiver is still decreased with the price. However, one should not seek to completely remove ferrite. The Empty ferrite assembly showed that without any ferrite the efficiency decreased roughly 4 % compared to the Original assembly.

4.6 Conclusion

The main findings of this thesis were: wireless charging can be simulated with commercial FEM software if right assumptions are made, wireless charger with prismatic coils can be optimized for higher mutual inductance and lower mass, vehicle speed does not directly affect to wireless charging. These findings contribute to the development of wireless chargers and they are in line with other research.

In future research, the sensitivity analysis started in chapter 2.4.2 could be expanded to greater variation. Moreover, the performance analysis could be confirmed and check the assumption made in this thesis. The new ferrite assemblies could also be further refined to obtain even better designs. After all, the goals of this research were reached and many things were covered. The thesis provides a good overview for anyone interesting wireless charging and it will be a platform for future research.

5 References

[1] "Electric Vehicle Database," 2019. [Online]. Available: https://ev-database.org/cheatsheet/range-electric-car. [Accessed: 11-Dec-2019].

[2] Z. Bi, T. Kan, C. C. Mi, Y. Zhang, Z. Zhao, and G. A. Keoleian, "A review of wireless power transfer for electric vehicles: Prospects to enhance sustainable mobility," *Appl. Energy*, vol. 179, pp. 413–425, 2016.

[3] M. Tampubolon, L. Pamungkas, H. Chiu, and Y. Liu, "Dynamic Wireless Power Transfer for Logistic Robots," *MDPI*, vol. 11, no. 3, pp. 1–10, 2018.

[4] W. J. Sweeting, A. R. Hutchinson, and S. D. Savage, "Factors affecting electric vehicle energy consumption," *Int. J. Sustain. Eng.*, vol. 4, no. 3, pp. 192–201, 2011.

[5] V. M. Cirimele, "Design and integration of a dynamic IPT system for automotive applications," Paris-Saclay, 2017.

[6] MICEV, "METROLOGY FOR INDUCTIVE CHARGING OF ELECTRIC VEHICLES (MICEV)," 2018. [Online]. Available: https://www.inrim.it/ricerca-sviluppo/qualita-della-vita/metrologia-lenergia-e-lambiente/micev. [Accessed: 25-Feb-2018].

[7] MICEV, "MICEV project homepage." [Online]. Available: https://www.micev.eu/. [Accessed: 14-Jan-2020].

[8] R. Ruffo, V. Cirimele, M. Diana, M. Khalilian, A. La Ganga, and P. Guglielmi, "Sensorless Control of the Charging Process of a Dynamic Inductive Power Transfer System with an Interleaved Nine-Phase Boost Converter," *IEEE Trans. Ind. Electron.*, vol. 65, no. 10, pp. 7630–7639, 2018.

[9] V. Cirimele, L. Pichon, and F. Freschi, "Electromagnetic modeling and performance comparison of different pad-to-pad length ratio for dynamic inductive power transfer," in *IECON Proceedings (Industrial Electronics Conference)*, 2016, pp. 4499–4503.

[10] COMSOL, "COMSOL Multiphysics 5.4." 2018.

[11] J. Tamminen, "Modelling inductive charger in Elmer Multiphysics software Bachelor ' s thesis," Aalto-university, 2018.

[12] M. IBRAHIM, "Wireless Inductive Charging for Electrical Vehicles : Electromagnetic Modelling and Interoperability Analysis," UNIVERSITE PARIS-SUD, 2014.

[13] SAE, "Surface Vehicle," SAE international, 2017.

[14] M. Budhia, G. A. Covic, and J. T. Boys, "Design and optimization of circular magnetic structures for lumped inductive power transfer systems," *IEEE Trans. Power Electron.*, vol. 26, no. 11, pp. 3096–3108, 2011.

[15] SAE, "J2954 Surface Vehicle Recommended Practice," SAE international, 2019.

[16] Ferroxcube, "Soft Ferrites and Accessories - Data Handbook." Ferroxcube, pp. 13, 61, 2013.

[17] ElectronicsTutorials, "Magnetic Hysteresis," *Electronics Tutorials*. [Online]. Available: https://www.electronics-tutorials.ws/electromagnetism/magnetic-hysteresis.html. [Accessed: 21-Jan-2020].

[18] A. EPCOS, "Soft Ferrites and Accessories - Data Handbook," pp. 6,44-45, 2013.

[19] "Motor Fan illustrated," *Motor Fan illustrated*, Tokyo, p. 12.

[20] Granta Design, "CES EduPack 2019." 2019.

[21] "MatWeb," 2019. [Online]. Available: http://matweb.com. [Accessed: 01-Oct-2019].

[22] W. Frei, "How to Model Conductors in Time-Varying Magnetic Fields," *COMSOL Blog*. [Online]. Available: https://www.comsol.com/blogs/how-to-model-conductors-in-time-varying-magnetic-fields/. [Accessed: 22-Jan-2020].

[23] I. Lindell and A. Sihvola, *Sähkömagneettinen kenttäteoria 1. Staattiset kentät*, 6th ed. Helsinki: Helsinki University Press, 2007.

[24] "Teflon Insulated Litz Wire/Milti Strand Manget Wire," *Made-in-chine*. [Online]. Available: https://www.made-in-china.com/showroom/gucien/product-detailvbRQXVkGAFYS/China-Teflon-Insulated-Litz-Wire-Milti-Strand-Manget-Wire.html.

[25] T. Thabet and D. John, “An Approach to Calculate the Efficiency for an N-Receiver Wireless Power Transfer System,” *Int. J. Adv. Comput. Sci. Appl.*, vol. 6, no. 9, pp. 91–98, 2015.